BM@N
Baryonic Matter at Nuclotron

Technical Design Report

The Silicon Tracking System
as part of the hybrid tracker of the BM@N experiment

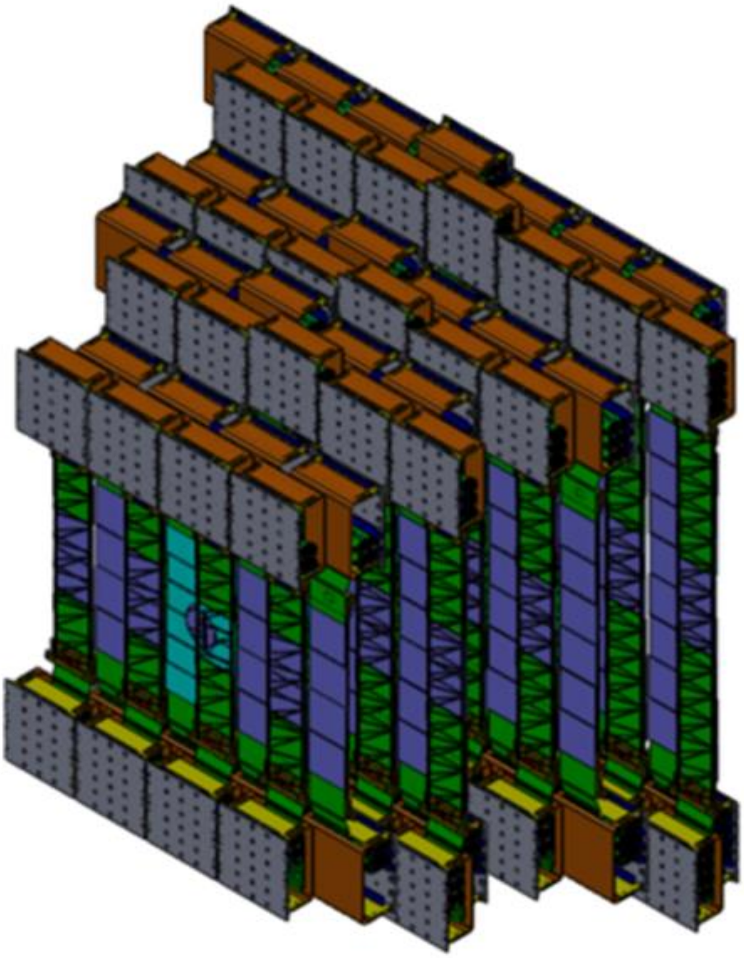

Dec. 2019

The BM@N STS group:

A. V. Baranov[4], D. Dementev[1], V. Elsha[1], J. Heuser[2], P. I. Kharlamov[1,4], I. M. Kovalev[4], A. Kolzhvari[1], I. A. Kudryashov[4], A. A. Kurganov[4], E. Lavrik[3], V.V. Leontyev[4] T. Lygdenova[1], M. M. Merkin[4,1], Y. Murin[1], J. Panasenko[5], M. Protsenko[1], C. J. Schmidt[2], H. R. Schmidt[2,5], A. Sheremetev[1], A. Sheremeteva[1], A. Senger[3], P. Senger[3,6], N. Sukhov[1], M. Shitenkov[1], A. Voronin[1], A. G. Voronin[4], W. Zabolotny[7], A. Zinchenko[1]

[1] JINR LHEP Dubna, Russia
[2] GSI Helmholtzzentrum, Darmstadt, Germany
[3] FAIR Darmstadt, Germany
[4] SINP MSU, Moscow, Russia
[5] University Tübingen, Germany
[6] NRNU MEPhI, Moscow, Russia
[7] Warsaw University of Technology, Warsaw, Poland

Editors: Dmitrii Dementev, Peter Senger

Acknowledgements

We acknowledge support by the Joint Institute for Nuclear Research (JINR), Dubna, Russia, and by the GSI Helmholtzzentrum für Schwerionenforschung GmbH, Germany.

Contents

Summary

This document describes the plans for upgrading the BM@N experiment in order to investigate Au + Au collisions up to energies of 4.5A GeV and beam intensities of 20 kHz. These measurements open the unique possibility to perform pioneering studies of fundamental questions: the high-density equation-of-state (EOS) of symmetric nuclear matter, the existence of a mixed phase in dense QCD matter, and the lifetime of various hypernuclei. The relevant observables, which will allow to shed light on the high-density EOS and the mixed phase, are multi-strange hyperons, which have to be measured in different collision systems and beam energies.

The handling of the high particle densities and rates requires the installation of several additional layers of highly-granulated silicon detectors in front of the GEM tracking system. The task of the hybrid Silicon-GEM tracking system is to measure the trajectories of charged particles originating from the interactions of heavy-ion beams with nuclear targets. The challenge is to reconstruct the tracks of more than 300 charged particles per central Au+Au interaction with high efficiency and a good momentum resolution.

First feasibility studies have been performed based on a hybrid tracking system of 4 stations double-sided micro-strip silicon sensors and 7 layers of (partly existing) GEM chambers. Using 1000 central Au+Au events with a beam kinetic energy of 4A GeV generated by the DCM-QGSM code, lambda hyperons have been reconstructed with a total efficiency of $\varepsilon(4\pi) = 10\%$, an invariant mass resolution of $\sigma = 1.1$ MeV/c^2, and a signal-to-background ratio of $S/B = 5.2$. The next step would be to use the information on the time-of-flight in the simulations for particle identification, based on a realistic detector response of the TOF detector, and track matching between the GEMs and the TOF detectors. Then, the statistics of the events has to be improved considerably, to allow for the reconstruction of Ξ^- and Ω^- hyperons, which are the most important observables.

For future measurements with a high-intensity gold beam, the air gaps in the beam line from the Nuclotron to the BM@N setup have to be removed, and the setup has to be upgraded with an evacuated beam pipe. The proposed design of a beam pipe with several small kinks to follow the beam deflected by the magnetic dipole field has been validated by FLUKA calculations. Moreover, it was shown the radiation doses applied to the inner part of the silicon and GEM stations over the life time of the experiment can be tolerated.

The requirements on both the tracking detector granularity and the signal read-out speed to accommodate Au+Au reaction rates up to 20 kHz can be fulfilled by four low-mass layers of silicon micro-strip sensors which have been developed for the CBM experiment at FAIR. The detector layers are located at distances between 30 cm and 90 cm downstream of the target inside the magnetic dipole field. The sensors are mounted onto lightweight mechanical support ladders and read out through multi-line micro-cables with fast electronics at the periphery of the stations where cooling lines and other infrastructure can be placed. The micro-cables will be built from sandwiched polyimide-Aluminum layers with a radiation length of $X/X_0 \leq 0.02\%$. The micro-strip sensors will be double-sided with a stereo angle of 7.5 degrees, with 1024 strips in each side, a strip pitch of 58 μm, strip lengths between 40 and 60 mm, and a thickness of 300 μm of silicon.

The STS is operated in a thermal enclosure that keeps the sensors stable at room temperature. The heat dissipated in the read-out electronics is removed by a water

cooling system. The mechanical structure of the detector system including the service and signal connections is designed such that single detector ladders can be exchanged without disconnecting and removing more than one detector station.

The STS project is realized in cooperation of institutes from Germany, Russia, Poland, and Ukraine. The detector system will be constructed and installed into the BM@N experiment in 2022-2023.

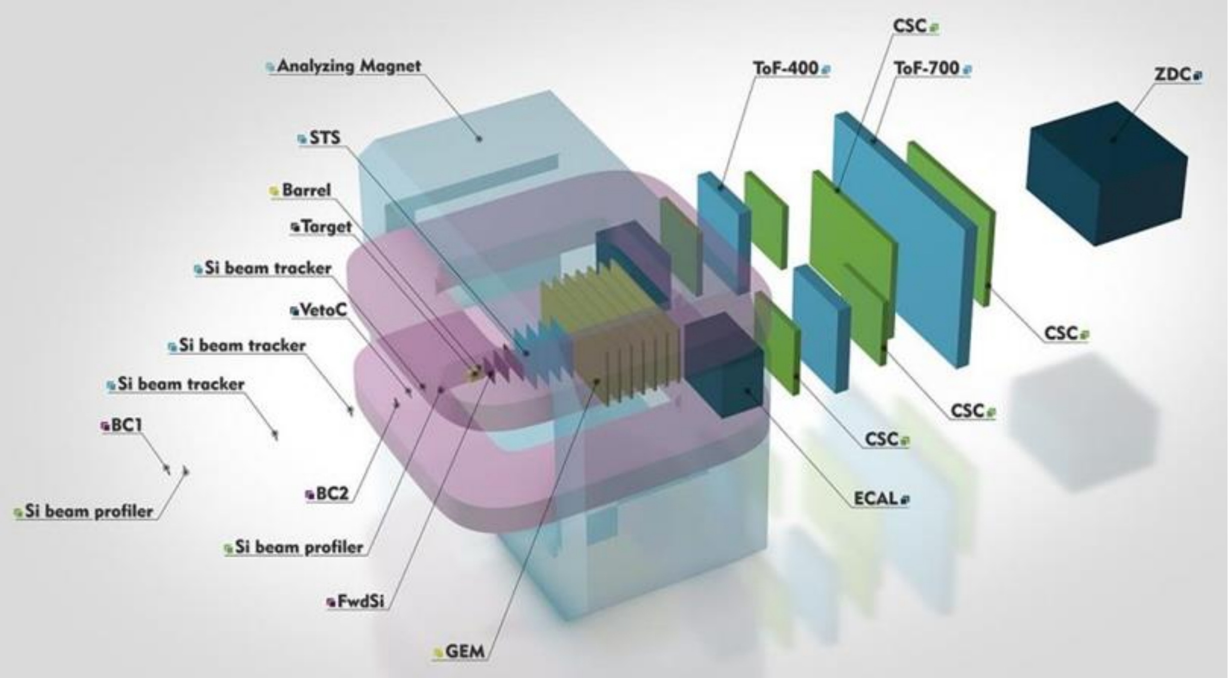

The BM@N experiment with its detector systems

1 The research program of the upgraded BM@N experiment

1.1 Exploring the QCD phase diagram at neutron star core densities

The experimental and theoretical investigation of the properties of elementary matter under extreme conditions is a major topic of international fundamental research. The goal of this research is to explore the various forms and phases of strongly interacting matter. Similar to water, which exhibits different states separated by phase transitions, it is expected that the degrees of freedom of nuclear matter change with temperature and density, thereby creating novel forms of elementary matter. The fundamental theory of strong interaction, Quantum Chromo Dynamics (QCD), predicts a smooth crossover transition from hadronic matter to the quark-gluon plasma at a pseudo-critical temperature of about 155 MeV for vanishing net-baryon density [1-3]. However, QCD still fails to make predictions about the properties of matter at high net-baryon densities. Our conception of compressed nuclear matter is based on effective model calculations which predict structures in the QCD phase diagram at high net-baryon densities, like a critical endpoint followed by a first-order phase transition, or new forms of exotic matter [4-6].

Figure 1.1 depicts a sketch of the three-dimensional phase diagram of nuclear matter as function of temperature, baryon-chemical and isospin-chemical potentials [7]. The picture includes the conjectured landmarks such as the chiral and deconfinement phase transition, their critical endpoint, exotic phases like quarkyonic matter, together with the expected locations of cosmic matter such as neutron stars, neutron star mergers, and supernovae.

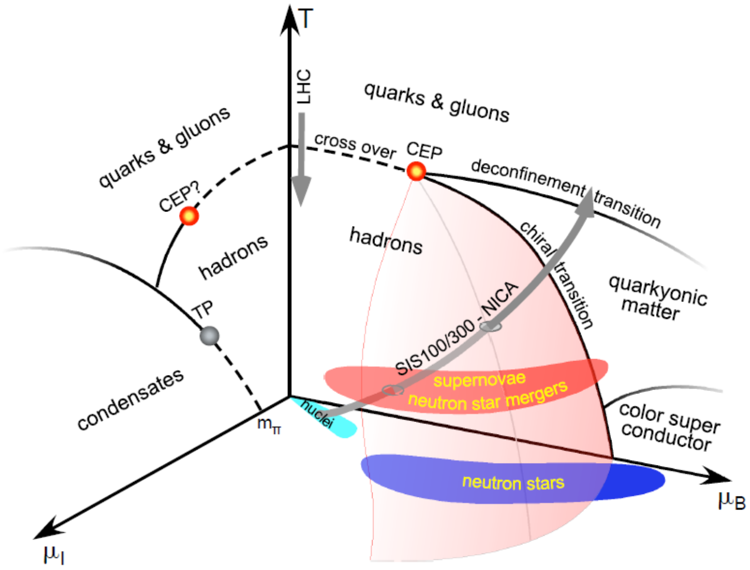

Fig. 1.1: Sketch of the three-dimensional phase diagram of nuclear matter as function of temperature, baryon-chemical and isospin-chemical potentials [7].

Experimentally, only little is known about the QCD phase diagram. The comparison of the measured yields of particles and antiparticles to the results of thermal model calculations provides a so called freeze-out temperature as function of baryon chemical potential [8,9]. This temperature is measured at a late stage of the collision, when the produced particles cease to interact, and the density has dropped well below saturation density. However, for LHC and top RHIC energies, the freeze-out temperature coincides with the pseudo-critical temperature predicted by QCD, indicating that freeze-out and hadronization might happen simultaneously. The mission of heavy-ion experiments at lower beam energies is to explore the QCD phase diagram in the region of high net-baryon densities, where structures like a first order phase diagram or new phases like quarkyonic matter arepredicted to exist. Of fundamental importance for our understanding of supernova explosions, the structure of neutron stars, and the dynamics of neutron star mergers, is the high-density equation of state, which can be studied in relativistic heavy-ion collisions.

The Nuclotron at JINR in Dubna will deliver gold beams with kinetic energies between 2 and 4.5A GeV. Heavy-ion collisions in this energy range are well suited for the creation of high net-baryon densities. This is illustrated in figure 1.2 where the net-baryon density is plotted versus time for central Au+Au collisions at a beam energy of 5A GeV as predicted by several transport models and a hydro-dynamical calculation [10]. According to these calculations, it is expected that the nuclear fireball will be compressed already at a beam energy of 4.5A GeV to more than 4 times saturation density ρ_0. The calculations illustrate, that the Nuclotron energy range is very well suited to produce baryonic matter at neutron star core densities.

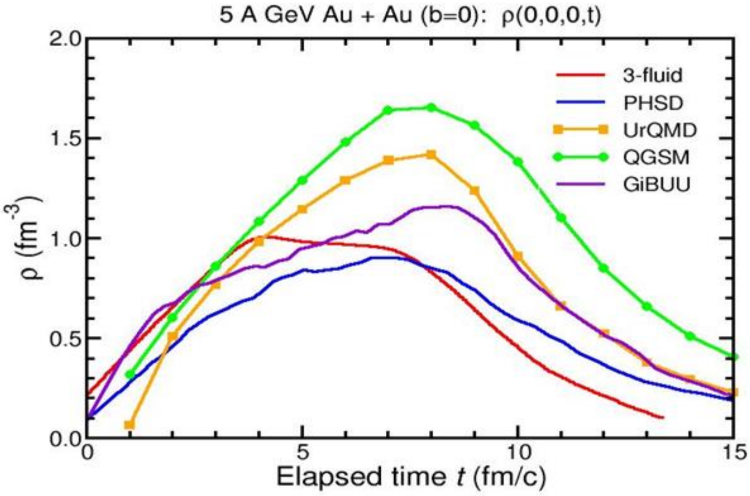

Fig. 1.2: Net-baryon density versus time reached in a central Au+Au collision at 5 A GeV beam energy according to various transport codes and a hydro-dynamical calculation [10]. A net baryon density of $\rho=1\ fm^{-3}$ corresponds to about 7 times the density of an atomic nucleus.

In heavy-ion collisions at top SPS, RHIC, and LHC energies it is observed, that the measured multiplicity of multi-strange hyperons is in agreement with predictions of the statistical hadronization model (SHM), which characterizes the matter in the collision zone by a temperature and a baryochemical potential [11]. However, the equilibration of in particular Ω baryons could not be understood in terms of hadronic two-body relaxation processes in the limited life time of the fireball. It was thus taken as strong indication that the system had undergone a transition from a partonic phase to the hadronic final state, with the equilibration being driven by multi-body collisions in the high particle density regime near the phase boundary [12]. In contrast, at low beam energies as available at GSI/SIS18, it was found that the multiplicity of Ξ^- hyperons exceeds the SHM predictions by about a factor of 24±9 [13]. Therefore, the measurement of multi-strange hyperons in Au+Au collisions at different Nuclotron beam energies will explore the onset of equilibration of multi-strange hyperons at high net-baryon densities, which might be a signature of a mixed phase of QCD matter.

1.2 The nuclear matter equation-of-state

According to calculations, the density in the core of neutron stars reaches values of 3 - 5 ρ_0 for star masses between 1.3 and 1.8 solar masses, and values of 5 - 8 ρ_0 for star masses between 1.8 and 2.0 solar masses [14]. These values depend on the chosen equation-of-state (EOS) of dense nuclear matter. In order to accommodate large neutron star masses, the EOS has to be stiff at high densities [15]. On the other hand, measurements of subthreshold kaon production [16] and elliptic flow of fragments [17] at SIS18 indicate, that at densities around 2 ρ_0 the EOS of symmetric matter is soft. Therefore, it is evident that the EOS has to stiffen at densities beyond 2 ρ_0, i.e. at densities which are reached in heavy-ion collisions at the Nuclotron at JINR and at SIS100 at FAIR.

The nuclear matter equation of state (EOS) describes the relation between density, pressure, volume, temperature, energy, and isospin asymmetry, and can be written as the energy per nucleon as function of density and isospin

$$E_A(\rho,\delta) = E_A(\rho,0) + E_{sym}(\rho)\cdot\delta^2 + O(\delta^4)$$

with the isospin asymmetry parameter $\delta= (\rho_n-\rho_p)/\rho$. Symmetric matter is stable around saturation density ρ_0 with a binding energy of $E/A(\rho_o) = -16$ MeV, the slope $\delta(E/A)(\rho_o)/\delta\rho = 0$, and the curvature $K_{nm} = 9\rho^2 \ \ \delta^2(E/A)/\delta\rho^2$ with K_{nm} the nuclear incompressibility. At densities around 2 ρ_0, the nuclear incompressibility has been determined from heavy-ion collisions, and values of $K_{nm} = 200 \pm 20$ MeV have been found, corresponding to a soft EOS, as mentioned above.

Various EOS calculated for symmetric nuclear matter and for neutron matter are shown in figure 1.3 as function of density [18]. In order to determine the EOS which is relevant for neutron stars, laboratory experiments try to measure the symmetry energy E_{sym}, which is the difference between the EOS for symmetric and neutron matter. Most of the experiments performed so far measure E_{sym} at densities around ρ_0, and then extrapolate to higher densities [19]. However, the calculations shown in figure 1.3 illustrate, that beyond densities of about 2 ρ_0 the various EOS differ significantly, and extrapolations to 4 or 5 ρ_0 are not conclusive. Moreover, according to figure 1.3, it is not sufficient to measure E_{sym} at high densities, but one has to measure the EOS for symmetric nuclear matter as well, in order to determine the EOS for neutron matter.

EOS-related observables in heavy-ion collisions should be sensitive the pressure and/or to the density in the nuclear fireball. The collective flow of identified particles is sensitive to the pressure gradient created in the early fireball, and provides information on the dense phase of the collision, i.e. on the nuclear incompressibility. In order to extract this value from experimental data, they have to be compared with results of transport calculations for different EOS, which can be derived from a parametrization of the nucleon-nucleon potential [18]. The in-plane flow and the elliptic flow of protons has been measured in Au+Au collisions at kinetic beam energies between 2 and 10A GeV, corresponding to densities from about 3 to 8 ρ_0, and values for the incompressibility of nuclear matter have been extracted, which range from K_{nm} = 200 MeV to 300 MeV [20]. Unfortunately, this wide range of values is not sufficient to make any prediction which would be relevant for our understanding of neutron stars. In order to reduce the uncertainty of K_{nm} in this important density region, future experiments should study the collective flow in this energy range not only for protons, but also for other baryons like hyperons.

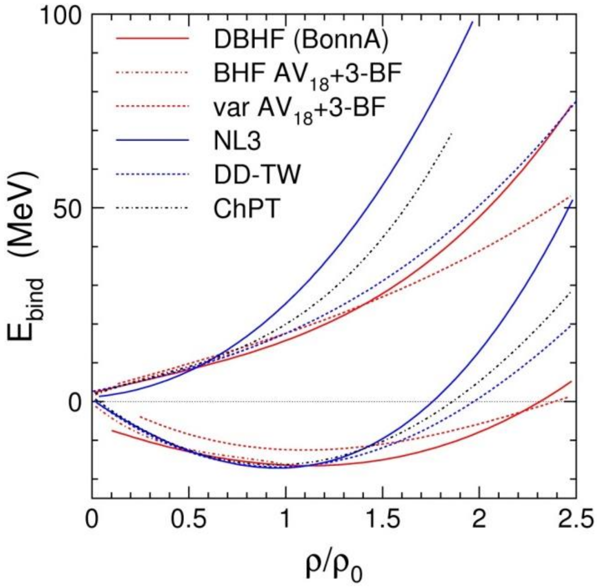

Fig. 1.3: EOS in isospin-symmetric nuclear matter (lower curves) and neutron matter (upper curves). BHF/DBHF and variational calculations are compared to phenomenological density functionals NL3 and DD-TW and ChPT [18].

Another important observable sensitive to the EOS is subthreshold particle production. In heavy-ion collisions, strange particles are produced already at kinetic beam energies per nucleon, which are well below the threshold energy in nucleus-nucleus collisions. For example, K^+ meson production has been observed in heavy-ion collision at beam energies down to 0.6A GeV, although the production energy threshold for the process $p+p \rightarrow K^+\Lambda\ p$ is E_{thr} = 1.6 GeV [21]. According to transport models, the production proceeds via multiple collisions inside the fireball, involving baryonic resonances and mesons. These multiple collisions are enhanced at high densities, and, therefore, subthreshold kaon production was found to be sensitive to the nuclear incompressibility around densities of 2 ρ_0. The data were compatible with K_{nm} = 200 MeV for isospin symmetric matter [16].

In order to study the EOS at higher densities, beam energies well above the K^+ meson production threshold are required. In this case, diagnostic probes with higher threshold energies are needed, such as Ξ^- or Ω^- hyperons, which are produced in nucleon-nucleon collisions like $pp \rightarrow \Xi^- K^+K^+p$ with E_{thr} = 3.7 GeV, and $pp \rightarrow \Omega^- K^+K^+K^0p$ with E_{thr} = 7.0 GeV. However, according to transport models, Ω^- can be produced in Au+Au collisions already at 4A GeV via hyperon-hyperon collisions. Therefore, Ξ^- or Ω^- hyperons are expected to be sensitive probes of dense nuclear matter at 3 - 4 ρ_0, which can be reached in central Au+Au collisions at Nuclotron beam energies. As an example, PHQMD calculations [22] have been performed for Au+Au collisions at a beam kinetic energy of 4A GeV assuming two different nuclear inkompressibilities: K_{nm} = 240 MeV ("soft") and K_{nm} = 350 MeV ("hard"). Figure 1.4 depicts the yield ratios of hyperons simulated for a soft over a hard EOS. According to this preliminary calculation, the yield of multi-strange hyperons is about a factor of 2 higher for a soft EOS as compared to a hard EOS. Up to now, no data exist on multi-strange hyperon production in heavy-ion collisions in this energy range.

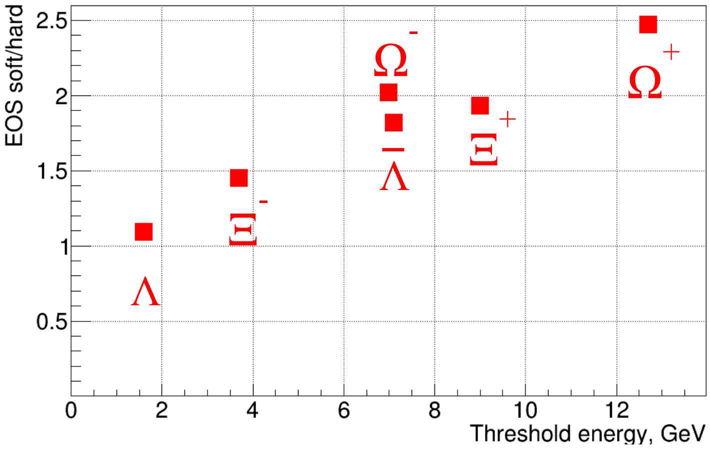

Fig. 1.4: Hyperon yield ratios calculated for Au+Au collisions with a beam kinetic energy of 4A GeV using the PHQMD event generator assuming a soft and a hard EOS as function of the production threshold energy in nucleus-nucleus collisions (preliminary result, details see text) [22].

1.3 Hypernuclei

Another important open question concerning the properties of dense nuclear matter in neutron stars, which is also related to the EOS, is the so called hyperon puzzle. With increasing density, the neutron chemical potential should exceed the hyperon chemical potential, leading to the weak decay of neutrons into hyperons. This process would soften the EOS, and, hence, prevent the existence of large-mass neutron stars, which, however, have been observed. The occurrence of neutrons in neutron stars depends, for example, on the lambda-nucleon and the lambda-lambda potential, which also plays a role in hypernuclei. Therefore, the identification of new (double-) lambda-hypernuclei, and the determination of their lifetime will shed light on the hyperon puzzle in neutron stars. Predictions of statistical model calculations on the yield of various light hypernuclei produced in central Au+Au collisions as function of collision energy shown in figure 1.5 [23]. The distributions reflect the interplay of the strangeness production probability increasing with beam energy, and of the probability for the production of light nuclei, which decreases with beam energy. The yield of hypernuclei exhibits a maximum in the energy range between $\sqrt{s_{NN}}$ = 3 – 5 GeV, which is in the reach of Nuclotron beams. The identification of hypernuclei requires a high-resolution tracking system close of the target. Therefore, the installation of the SIS100, and NICA, which, therefore, offer a substantial discovery potential.

In conclusion, the research program of BM@N includes:

1. Scouting the location of the transition between hadronic and partonic dominated matter by measuring the yield of Ξ^- and Ω^- hyperons in Au+Au collisions as function of beam energy.
2. Exploring the high-density EOS for symmetric nuclear matter by measuring
   - the excitation function of collective flow of identified particles in Au+Au collisions.
   - the excitation function of Ξ^- and Ω^- hyperons in Au+Au and C+C collisions
3. Precise measurement of yields and lifetime of known light hypernuclei, and search for new hypernuclei,

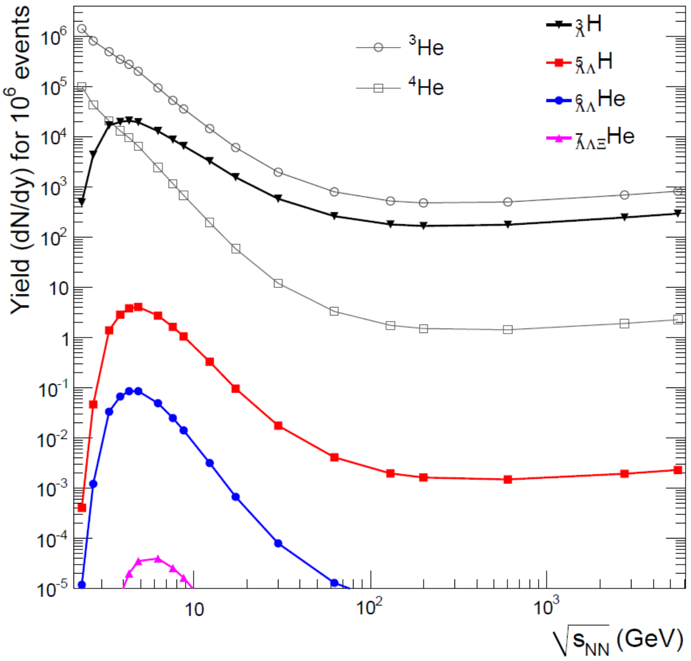

Fig. 1.5: Energy dependence of hypernuclei yields at midrapidity for 10^{6} central collisions as calculated with a thermal model. The predicted yields of ^{3}He and ^{4}He nuclei are included for comparison [25].

References

[1] S. Borsanyi et al., JHEP 1009 (2010) 073
[2] A. Basavov et al.: Phys. Rev. D85 (2012) 054503
[3] Y. Aoki et al., Nature, 443 (2006) 675
[4] J. Luecker et al., arXiv:1308.4509v1 [hep-ph]
[5] L. McLerran and R. D. Pisarski, Nucl. Phys. A796, (2007) 83
[6] K. Fukushima and T. Hatsuda: Rept. Prog. Phys. 74 (2011) 014001
[7] NUPECC Long Range Plan 2017
[8] F. Becattini et al., Phys. Rev. Lett. 111 (2013) 082302
[9] A. Andronic et al., Nature, 561, (2018) 321
[10] I.C. Arsene et al., Phys. Rev. C75 (2007) 24902
[11] A. Andronic, P. Braun-Munzinger and J. Stachel, Nucl. Phys. A 834 (2010) 237c
[12] P. Braun-Munzinger, J. Stachel and C. Wetterich, Phys. Lett. B 596 (2004) 61
[13] G. Agakishiev et al. (HADES collaboration), Eur. Phys. J. A 47 (2011) 21
[14] T. Klaehn et al., Phys. Rev. C74: 035802, 2006
[15] G. Baym et al., Reports on Progress in Physics 81 (2018) 056902
[16] Ch. Fuchs et al., Phys. Rev. Lett. 86 (2001) 1974
[17] A. Le Fevre et al., Nucl. Phys. A945 (2016) 112
[18] C. Fuchs and H.H. Wolter, Eur.Phys.J. A30 (2006) 5
[19] Bao-An Li, Nuclear Physics News, Vol. 27, No. 4, (2017) 7
[20] P. Danielewicz, R. Lacey, W.G. Lynch, Science 298 (2002) 1592
[21] C. Sturm et al., (KaoS Collaboration), Phys. Rev. Lett. 86 (2001) 39
[22] V. Kireyeu, private communication
[23] A. Andronic et al., Phys. Lett. B697 (2011) 203

2 Physics performance simulations of the hybrid tracking system (STS+GEM)

This chapter presents results of simulations of heavy-ion collisions performed for the hybrid tracking system of the upgraded BM@N experiment. This system comprises 4 detector stations equipped with double-sided micro-strip silicon sensors, and a set of 6 large-area GEM chambers. This detector configuration will allow to measure hadrons including multi-strange hyperons with high efficiency and good momentum resolution in Au+Au collisions at Nuclotron energies with beam intensities up to $2{\cdot}10^6$ ions/s. Using the event generator DCM-QGSM, 1000 central Au+Au collisions with a beam kinetic energy of 4A GeV have been simulated and analyzed with the latest CBM Cellular Automaton (CA) tracking code ported to the BmnRoot framework. This code is able to reconstruct tracks of charged particles which have produced at least 4 hits in subsequent detector layers. These hit may either be produced in the 4 silicon stations only, or in the GEM stations, or in both detector stations, like 2 (or more) hits in the silicon stations, and 2 (or more) hits in the GEM stations. The magnetic field was chosen to be 0.8 T, in order to keep the same deflection angle (and beam pipe configuration) as for a beam kinetic energy of 4.5A GeV at a magnetic field of 0.9 T. Lambdas can be identified by determination of their decay vertex, without identification of the daughter particles via time-of-flight. As a first step towards the identification of primary particles, MC information of hits in the BM@N Time-of-Flight (TOF) detectors has been used to study their geometrical acceptance. The studies have been performed by Alexander Zinchenko.

2.1 The Silicon Tracking System

The Silicon Tracking System (STS) of the BM@N will consist of 4 stations equipped with double-sided micro-strip sensors. The sensors have two sizes 42 mm x 62 mm, and 62 mm x 62 mm, and a thickness of 320 ± 15 μm. Each sensor has 1024 strips on each side with a strip pitch of 58 μm. The n-side has straight strips, the p-side has strips with a stereo angle of 7.5°, corresponding to a “pixel of size Δx = 58 μm times Δy = 58 μm/tan(7.5°) = 440.6 μm for a two-coordinate spatial measurement. The edge strips are connected via a second metallization layer. The strips are read out via ultra-thin micro-cables based on Aluminum-Polymide technology. The sensors are mounted on low-mass carbon structures (ladders).The stations 1, 2, 3, and 4 comprise 24, 52, 64, and 104 sensors of size 62x62mm^2. In the inner part of each station 8 sensors of size 42x42mm^2 are located, and 4 sensors of size 42x42mm^2 with cut edges close to the beam pipe. The layout of the stations is shown in figure 4.1.1 in Chapter 4. The geometry of the strips, the arrangement and the response function of the sensors, as well as the material budget of sensors, cables, and ladders are taken into account in the detector model used in the simulations.

2.2 The GEM chambers

The total active area of a GEM chamber is 163.2 x 45 cm^2 for the upper chambers, and 163.2 x 39 cm^2 for the lower chambers. The area of the strips depends on the detector region as depicted in figure 2.1. In the inner zone, where the particle density is high, the strips cover an area of about 1.2 cm^2 (0.8 mm x 15 cm). In the outer zone, the strips have a size of 2.4 cm^2 (0.8 mm x 30 cm). The channel read-out time is about 2 µs.

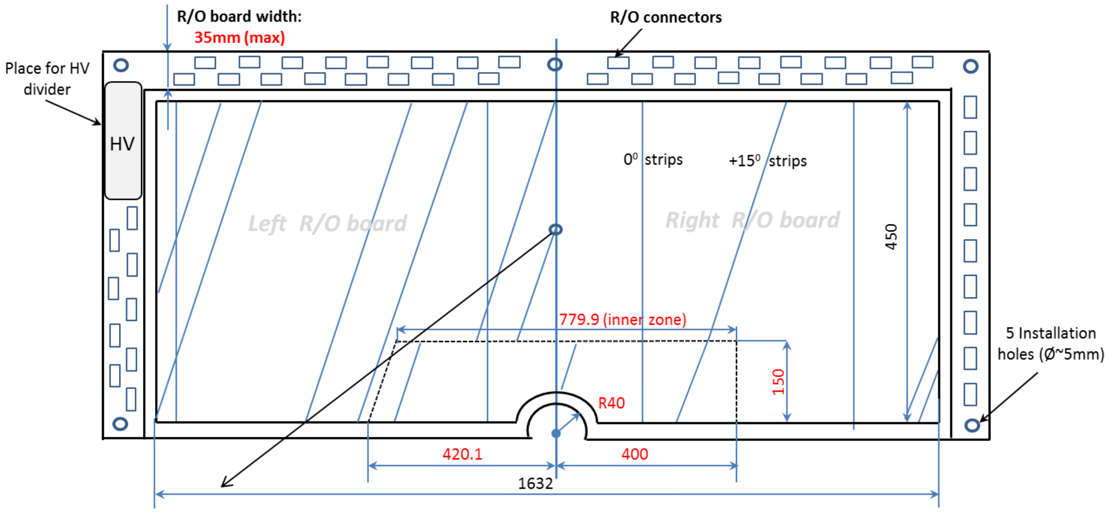

Fig.2.1: Layout and dimensions of the GEM chambers. Active area 163.2 x 45 cm^2 (upper chambers), and 163.2 x 39 cm^2 (lower chambers)

2.3 The BM@N hybrid tracking system

The BM@N hybrid tracking system comprises the 4 silicon stations and 6 GEM stations. The silicon stations are located at 30 cm, 50 cm, 70 cm, and 90 cm downstream the target, followed by the GEM detectors at 120 cm up to 270 cm, with a gap of 30 cm between the stations. A sketch of the hybrid system is presented in figure 2.2.

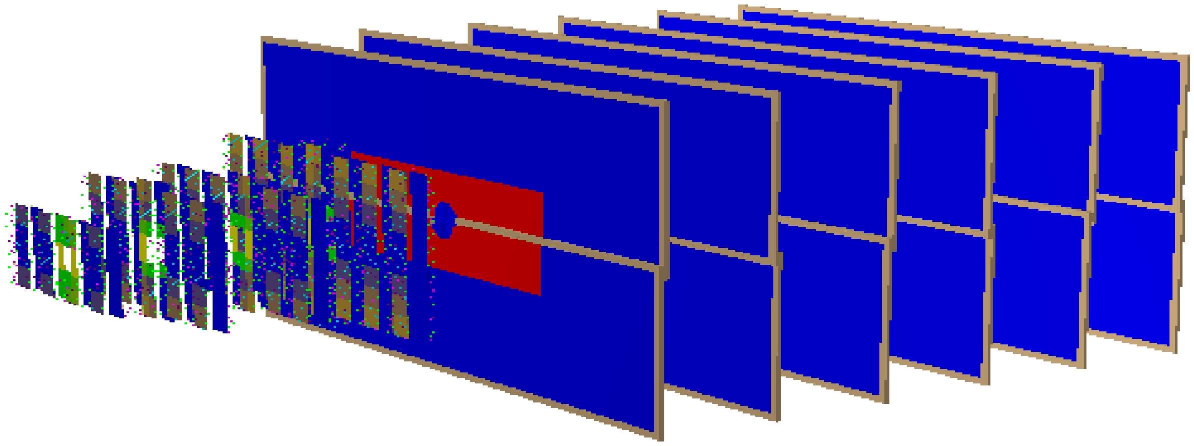

Fig. 2.2: The BM@N hybrid tracking system: 4 stations equipped with double-sided micro-strip silicon sensors, and 6 stations of GEM detectors (see text).

2.4 Track reconstruction efficiency

The simulations discussed in the following have been performed using the event generator DCM-QGSM. Central Au+Au collisions with a beam kinetic energy of 4A GeV have been generated and analyzed with the latest CBM tracking code ported to the BmnRoot framework. The magnetic field was chosen to be 0.8 T.

The analysis has been performed for 2 cases: using the information from the silicon stations only, and from the hybrid system silicon stations + GEM stations. Figure 2.3

depicts the re-constructible primary tracks, which are tracks which stem from the primary vertex and create at least 4 hits either in the silicon stations, or in the hybrid system Silicon +GEM. The blue histogram in figure 2.3 represents the tracks producing hits in Silicon+GEM, whereas the red histogram corresponds to the track seen by the silicon stations only. From the 1000 central Au+Au collisions, about 150000 tracks are re-constructible in the hybrid detector system, about half of these tracks have been identified based on hits in the silicon stations only. In figure 2.4 the reconstructed primary tracks are shown. About 88% of the re-constructible tracks have been found in the hybrid detector, compared to 93% for the tracks producing hits in the silicon stations only.

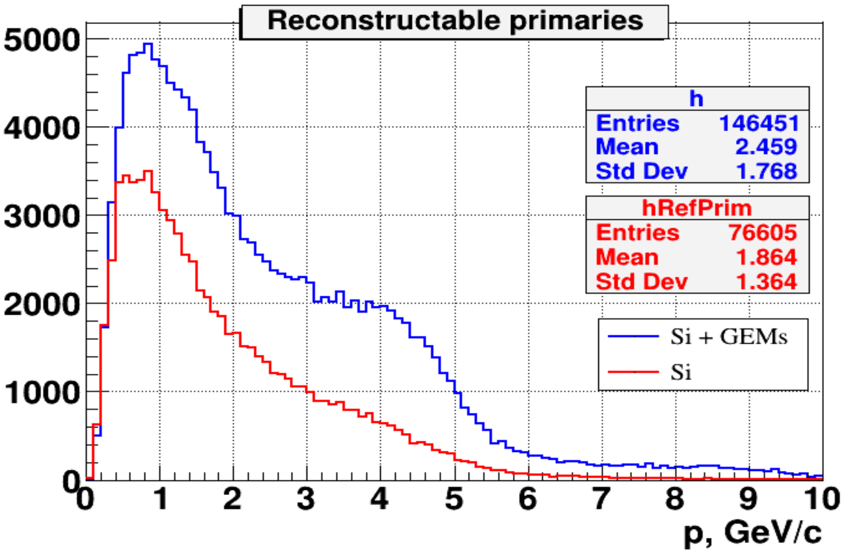

Fig. 2.3: Re-constructible (4 or more hits) primary tracks as function of momentum found in 1000 central Au+Au collisions at a kinetic beam energy of 4A GeV using the silicon stations only (red histogram), and using the hybrid system silicon + GEMs (blue histogram).

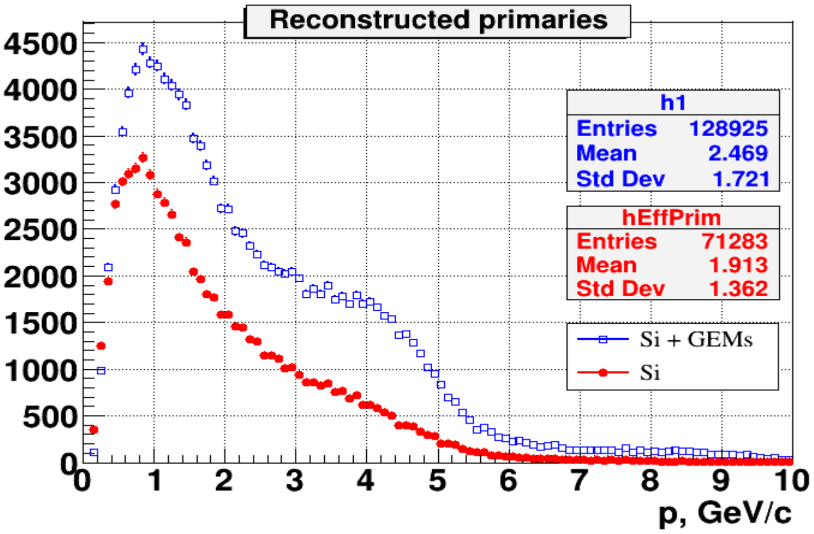

Fig. 2.4: Reconstructed (4 or more hits) primary tracks as function of momentum found in 1000 central Au+Au collisions at a kinetic beam energy of 4A GeV using the silicon stations only (red histogram), and using the hybrid system silicon + GEMs (blue histogram).

According to figures 2.3 and 2.4, almost twice as much primary tracks are re-constructible using the hybrid system, as compared to the silicon stations only. The reason for the difference is illustrated in figure 2.5, which depicts the phase space of primary particles re-constructible in the silicon+GEMs setup, but not re-constructible in the 4 silicon stations (left panel). It can be seen, that many of these tracks are emitted at polar angles around 5° and smaller. These particles miss the first silicon station, which has an inner hole with a diameter of about 6 cm, corresponding to an emission angle of 5.7°. The phase space distribution of those tracks, which are not found by the silicon stations, i.e. their inefficiency, is shown in the right panel of figure **2.5**, demonstrating that in addition to the tracks with small emission angles also tracks with very low momenta are not accepted.

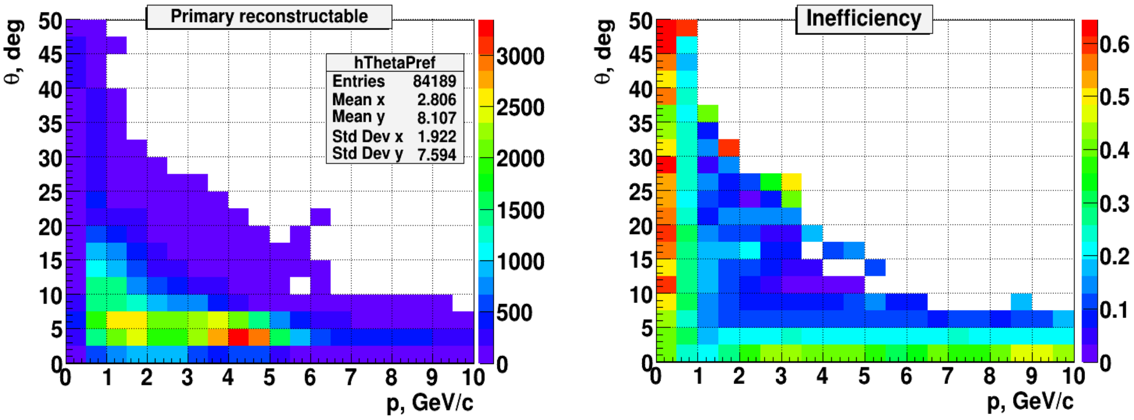

Fig. 2.5: Left: Phase space of primary particles re-constructible in the silicon+GEM setup, but not re-constructible in the silicon setup. Right: Phase space distribution of the particles which are not reconstructed by the four silicon stations.

The reconstruction efficiency for primary tracks as function of momentum is presented in figure 2.6. The primary tracks, which create only hits in the 4 silicon stations, can be reconstructed with an efficiency of better than 90% above a momentum of about 0.6 GeV/c, whereas the track reconstruction efficiency for the hybrid system reaches a maximum of about 90% between 1 and 2.5 GeV/c, and then drops to about 80% at 6 GeV/c. The reason for the lower efficiency of the Silicon+GEM system is the low granularity of the GEMs, which leads to a large number of clone hits being misinterpreted as real hits.

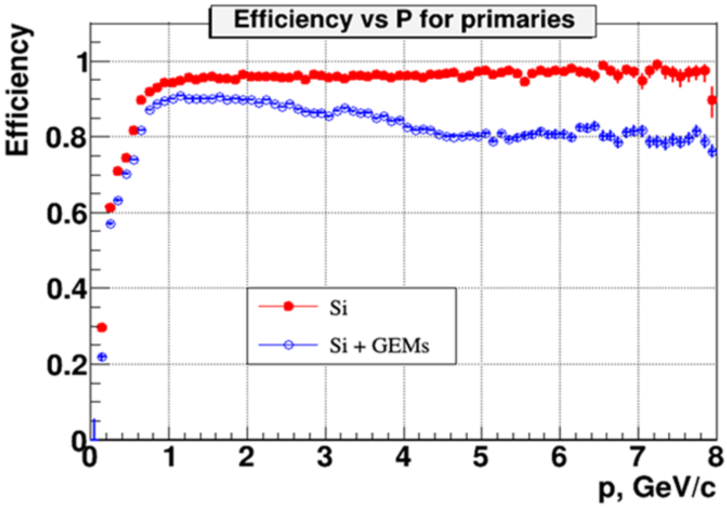

Fig. 2.6: Reconstruction efficiency as function of momentum for primary tracks with minimum 4 hits in the Si stations only (red histogram), and in the Si + GEM stations (blue histogram).

2.5 Momentum resolution

The momentum resolution for primary particles emitted in central Au+Au collisions at a beam kinetic energy of 4A GeV is shown in figure 2.7 for the different detector combinations. The left panel of figure 2.7 depicts the momentum resolution for primary tracks reconstructed in the silicon+GEM, whereas in the right panel the momentum resolution obtained with the 4 silicon stations is shown. The momentum integrated momentum resolution of the silicion+GEM setup is found to be Δp/p = 0.006, and Δp/p = 0.015 for the silicon stations. The momentum resolution for primary particles as function of momentum is shown in figure 2.8 for the silicon+GEM detector system. Only for momenta below p = 0.5 GeV/c the momentum resolution is worse than Δp/p = 0.006.

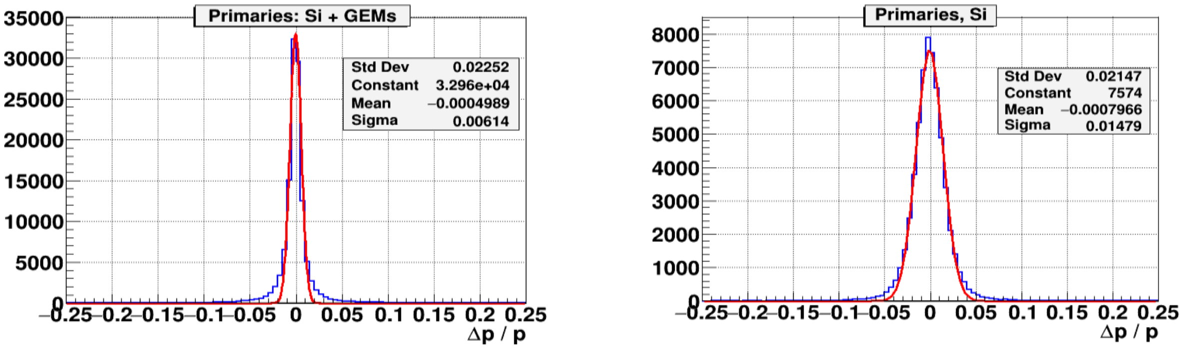

Fig. 2.7: Momentum resolution for primary tracks emitted in central Au+Au collisions at a beam kinetic energy of 4A GeV reconstructed in the silicon+GEM setup (left), and in the silicon setup (right).

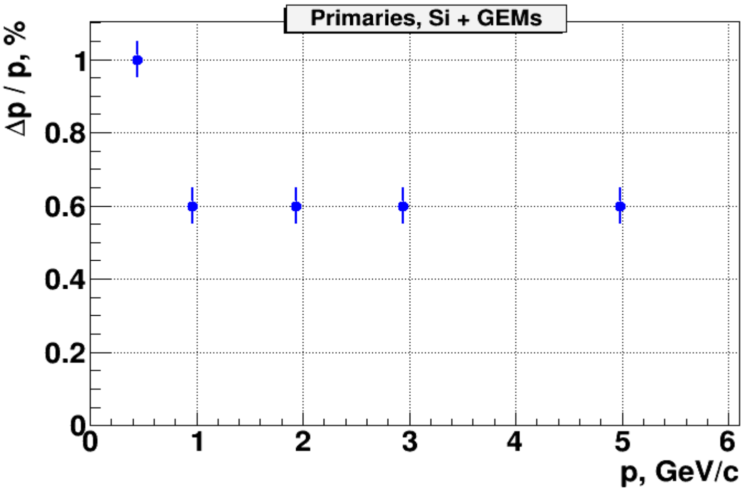

Fig. 2.8: Momentum resolution for primary tracks emitted in central Au+Au collisions at a beam kinetic energy of 4A GeV reconstructed in the silicon+GEM setup as function of momentum.

2.6 Phase space coverage for protons and pions

The phase space distributions of primary protons and pions emitted in central Au+Au collisions at a beam kinetic energy of 4A GeV as generated with the DCM-QGSM code are shown in the first row of figure 2.9 (protons left, pions right). The particle identification has been performed based on the Monte Carlo information. The center row depicts the distribution of primary protons (left) and pions (right) reconstructed in the silicon + GEM system, and in the lower row the corresponding distributions are shown as reconstructed with the silicon stations only. In the case of protons, about 47% of the produced protons are reconstructed by the Silicon+GEM system, and 21% by the silicon stations only. The corresponding acceptances for pions are lower (30% and 15%) because of the pion decay. Mid-rapidity is covered by both detector configurations. However, in contrast to the silicon stations (lower row), the hybrid system (center row) covers also a substantial region at small transverse momenta and forward rapidities. This inefficiency of the silicon stations was already illustrated by the right panel in figure 2.5.

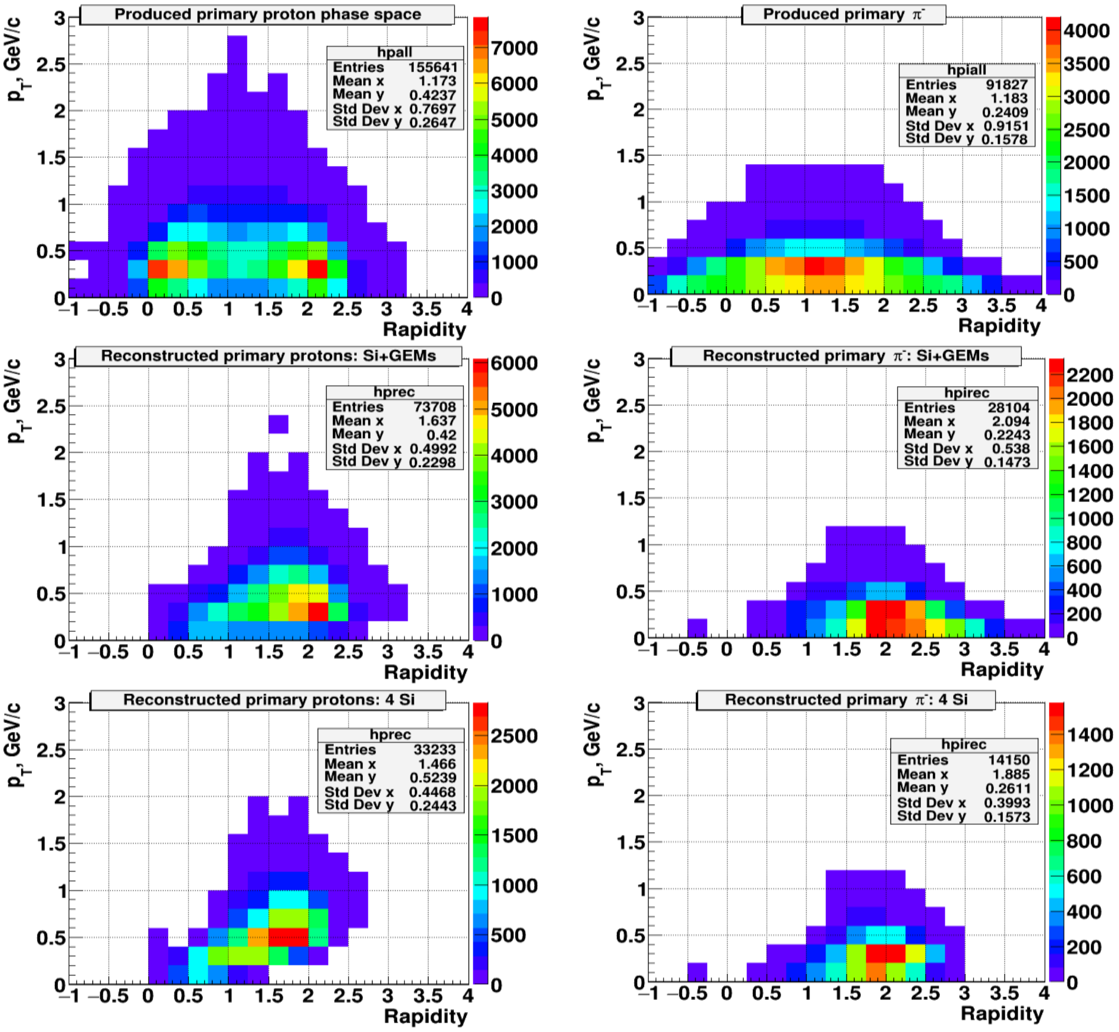

Fig. 2.9: Phase space distributions as function of transverse momentum and rapidity for protons (left column) and pions (right column) as generated with the DCM-QGSM code for central Au+Au collisions at a beam kinetic energy of 4A GeV (upper row), and reconstructed based on hits in silicon+GEM detectors (center row), and using hits in silicon stations only (lower row). Particle identification is based on Monte Carlo information.

2.7 Lambda reconstruction

The number of reconstructed lambdas as generated with the DCM-QGSM code for central Au+Au collisions at a beam kinetic energy of 4A GeV is presented in figure 2.10 for the silicon+GEM system (blue histogram) and for the silicon stations only (red histogram). The lambda reconstruction efficiency of the silicon+GEM system is more than 4 times higher than the one of the silicon stations only. This corresponds to the results shown in figure 2.11, which demonstrate that both the pion and proton acceptances of the silicon+GEM system are twice as large as the ones of the silicon stations. It is worthwhile to note, that no particle identification of the lambda decay products has been applied. The CA track finder identifies the vertex of the lambda decay into 2 charged particles ($\Lambda \rightarrow p+\pi^-$), and assumes that the decay products are either a pion or a proton, and vice versa. The resulting proton-pion invariant mass spectra are shown in figure 2.11 for the case of the silicon+GEM system (left) and for the silicon system only (right). The invariant mass resolution and the signal-to-background ratio are comparable for both cases. The significance of the signal is higher for the silicon+GEM system because of its higher reconstruction efficiency.

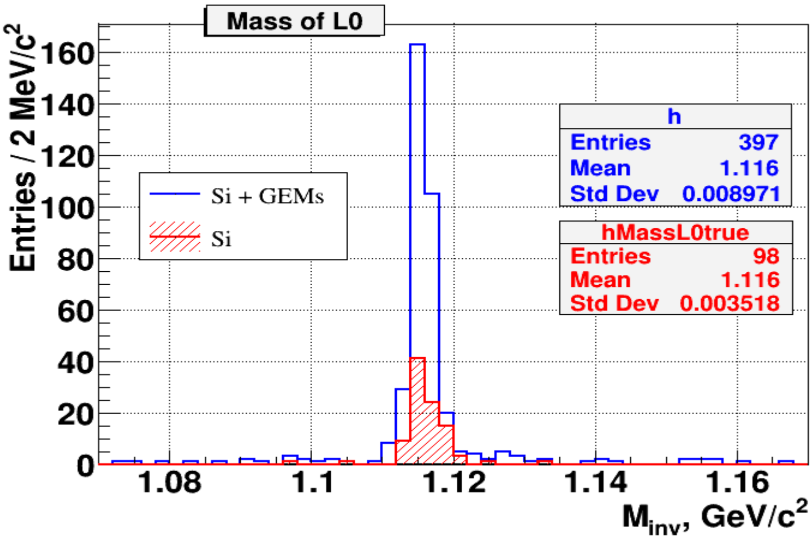

Fig. 2.10: Number of reconstructed lambdas using 4 silicon stations only (red histogram), and using the 4 silicon + 6 GEM stations (blue histogram).

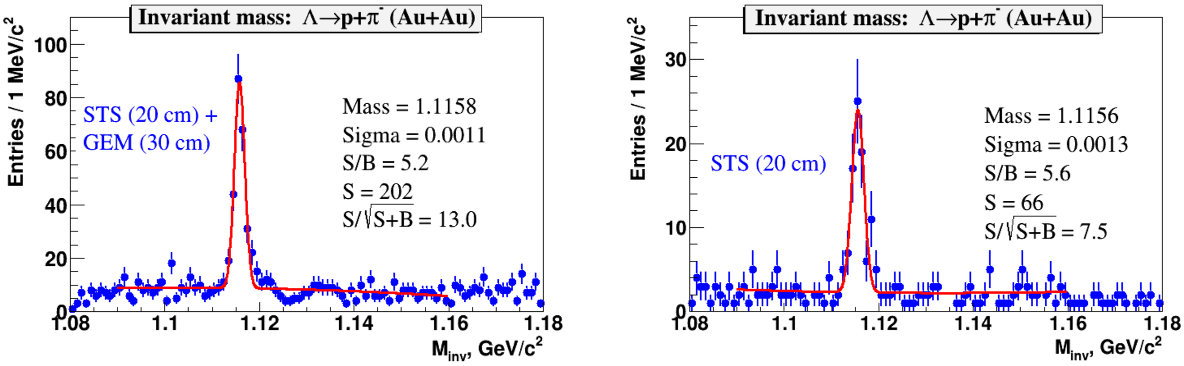

Fig. 2.11: Proton-pion invariant mass spectra using 4 silicon + 6 GEM stations (left panel), and using 4 silicon stations only (right panel).

The phase space distributions of lambdas and their decay products emitted in central Au+Au collisions at a beam kinetic energy of 4A GeV as generated with the DCM-QGSM code are shown in the first row of figure 2.12 (lambdas left, protons center, pions right). The proton and pion identification has been performed based on the Monte Carlo information. The center row depicts the distribution of lambdas (left), decay protons (center) and decay pions (right) reconstructed in the silicon + GEM system, and in the lower row the corresponding distributions are shown as reconstructed with the silicon stations only. Similar to the primary protons and pions (see figure **2.9**), the hybrid detector system covers a substantially larger phase space for lambdas than the silicon stations only.

According to figure 2.12, about 3800 lambdas are produced in 1000 central Au+Au collisions at 4A GeV kinetic beam energy. The number of the decay products correspond to the branching ratio of the lambda decay $\Lambda \to p+\pi^-$ which is BR = 0.64. The lambda reconstruction efficiency is slightly above 10% for the hybrid detector system, and about 2.6% for the silicon system only.

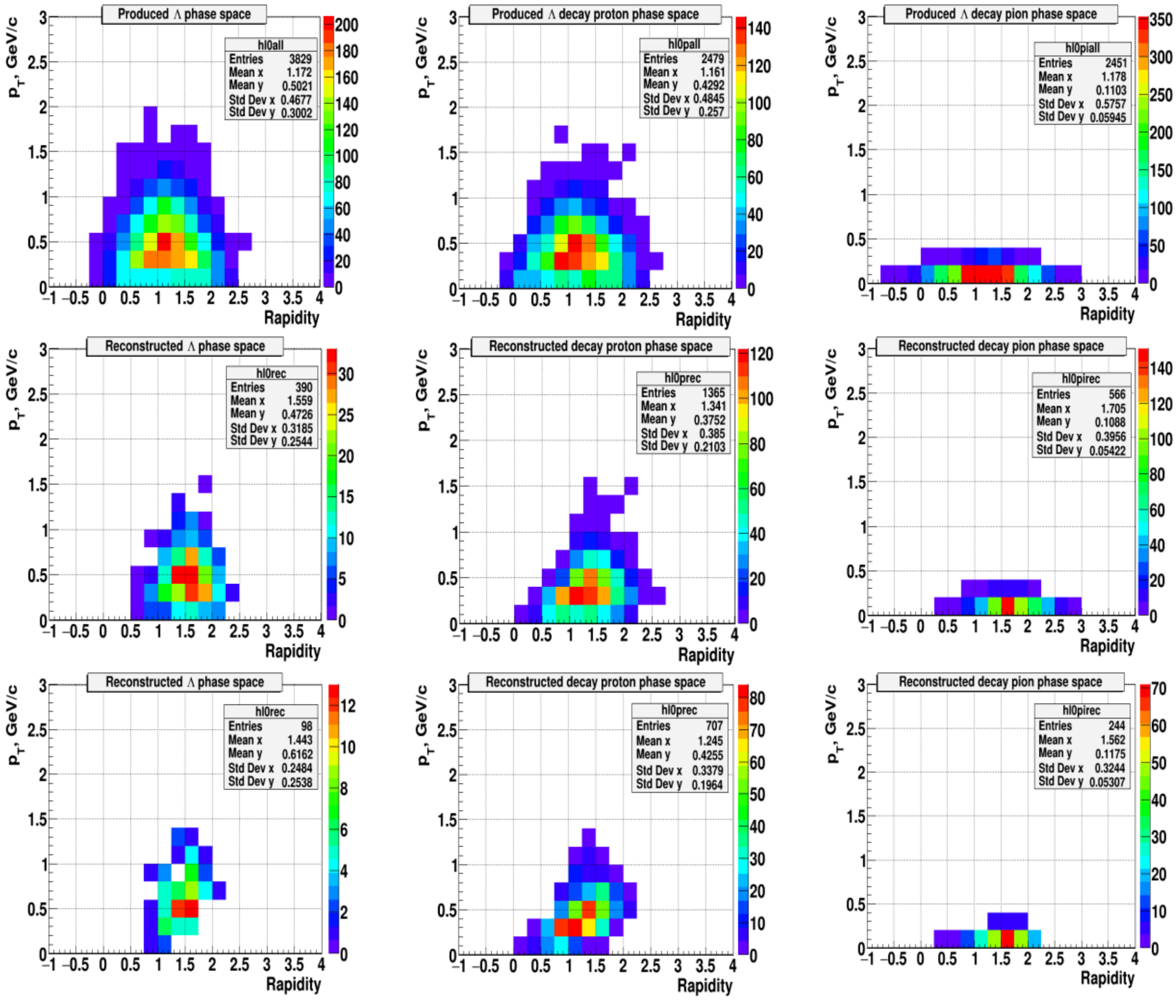

Fig. 2.12: Phase space distributions as function of transverse momentum and rapidity for Lambdas (left column), protons from lambda decays (center columns), and pions from lambda decays (right column), as generated with the DCM-QGSM code for central Au+Au collisions at a beam kinetic energy of 4A GeV (upper row), and reconstructed based on hits in the silicon+GEM detector system (center row), and using hits in the silicon stations only (lower row).

2.8 Acceptance of the time-of-flight detectors

Two sets of Time-of-flight (TOF) detectors have been installed, TOF-400 and TOF-700, consisting of multi-gap Resistive Plate Chambers (mRPC) made of window glass. Four TOF-400 detectors are situated at distances of 4.5 m from the target, two detectors to the left from the beam, two others to the right. The TOF-700 wall is located at a distance of 7 m downstream the target. The position and geometry of the TOF detectors with respect to the tracking detectors is sketched in figure 2.13.

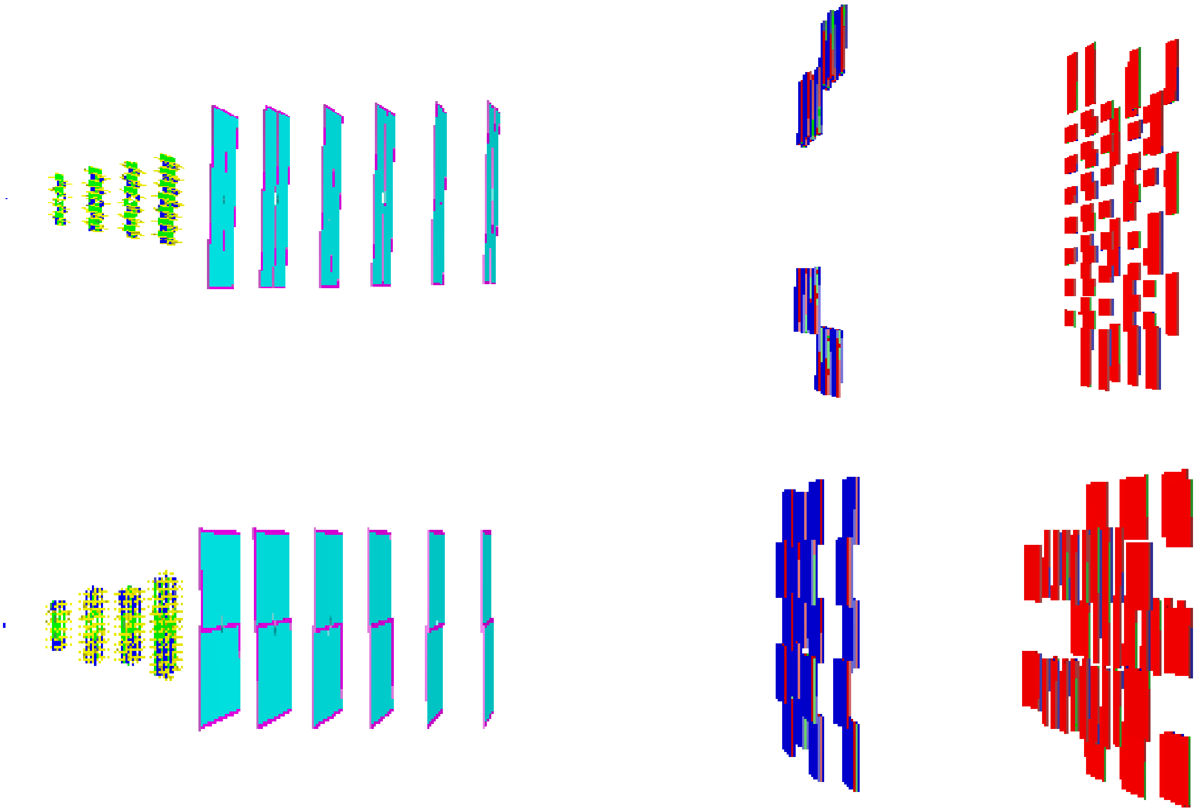

Fig. 2.13: The hybrid tracking system of the BM@N experiment together with the TOF detectors (in blue and red), which are located at a distance of 4.5 m and 7 m downstream the target. Upper picture: top view, lower picture: side view.

The results of the simulations including the TOF acceptance are illustrated in figure 2.14 and figure 2.15. The first row of figure 15 depicts the primary protons, π+ and π- mesons (from left to right) which have been reconstructed by the hybrid tracking system. The center row presents the reconstructed protons, π+ and π- mesons, which produce a MC hit in the TOF detectors. In the lower row of figure 2.14, the acceptance of the TOF detector is depicted for the three particle species. Please note, that these plots represent the geometrical TOF acceptance based only on MC information, no detector response and no track matching efficiency was taken into account. According to the lower row of figure 2.14, the TOF acceptance is above 90 % at forward rapidities, and decreases towards lower rapidities. For the pions this effect is more pronounced, reflecting the longer lifetime of high momentum pions, which are boosted towards large rapidities.

According to the upper and center row of figure 2.14, only 57 % of the protons, which are reproduced by the hybrid tracking system, will produce a MC hit in the TOF detectors. Only about 25% of the reproduced π+ and 27% of the reproduced π- mesons reach the TOF detectors. These numbers reflect, in addition to the geometrical TOF acceptance, the losses due to the finite lifetime of the pions.

As mentioned above (see figure 2.9), about 47% of the produced protons can be reproduced by the hybrid tracking system, and, consequently, only 27 % of the produced protons finally hit the TOF detectors. The corresponding number for the π- mesons is 8 %. These efficiencies might be further reduced taking into account the track matching efficiency between GEM and TOF detectors, and a realistic response function of the TOF detectors.

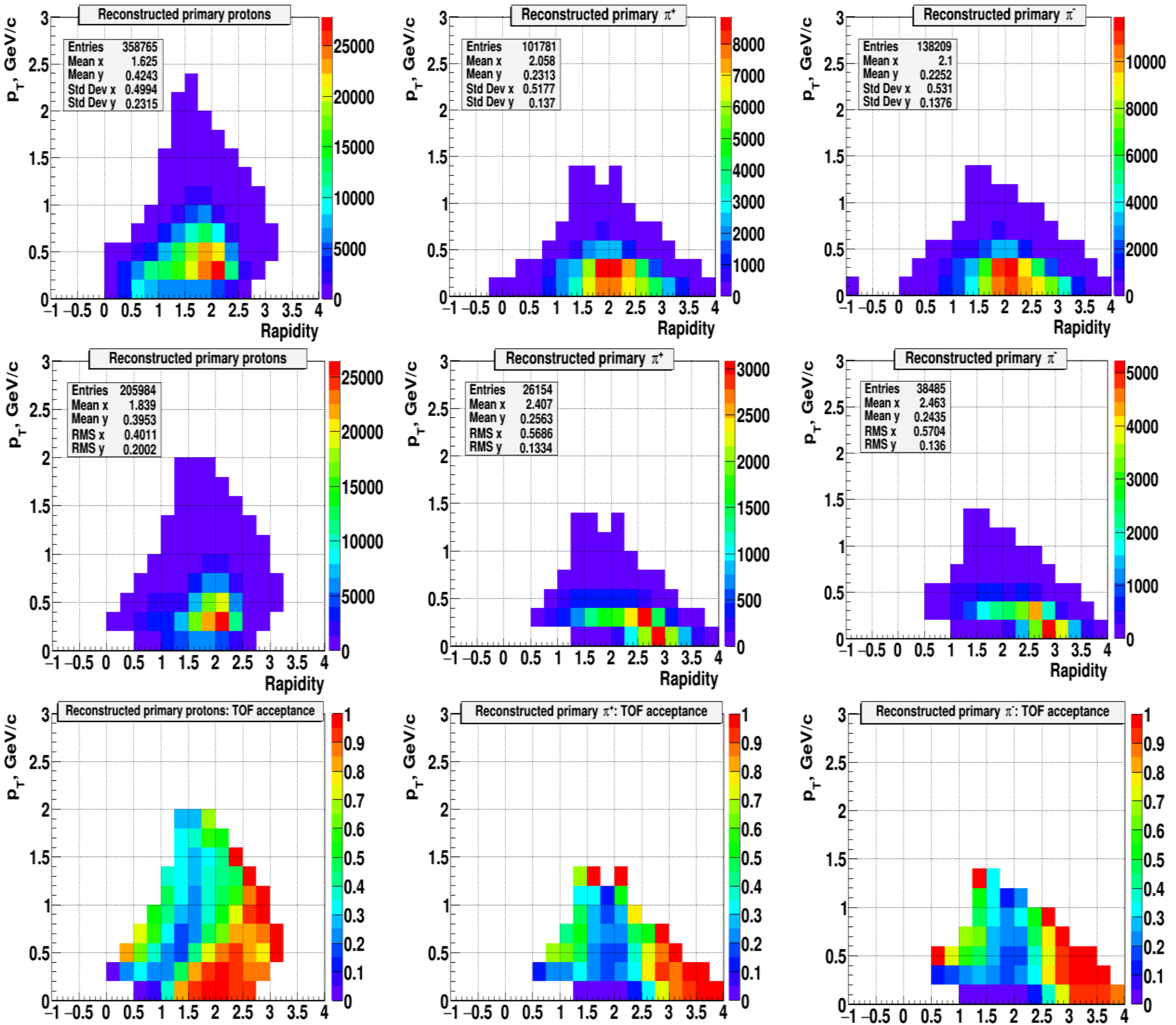

Fig. 2.14: Reconstructed primary protons, π+ and π- mesons (from left to right). Upper row: without MC hit in the TOF detectors, center row: with MC hit in the TOF detectors, lower row: acceptance of the TPF detectors.

The first row of figure 2.15 depicts the K+ mesons, K- mesons, and fragments reconstructed in the hybrid tracking system (from left to right) The center row presents the reconstructed K+ mesons, K- mesons and fragments which produce a MC hit in the TOF detectors. In the lower row of figure 2.15, the acceptance of the TOF detector is depicted for the three particle species. According to the upper and center row of figure 2.15, only 21 % of the reproduced K+ mesons, 20% of the K- mesons, but 69% of the fragments, produce a MC hit in the TOF detectors. Again, the small kaon efficiencies include losses to the finite lifetime.

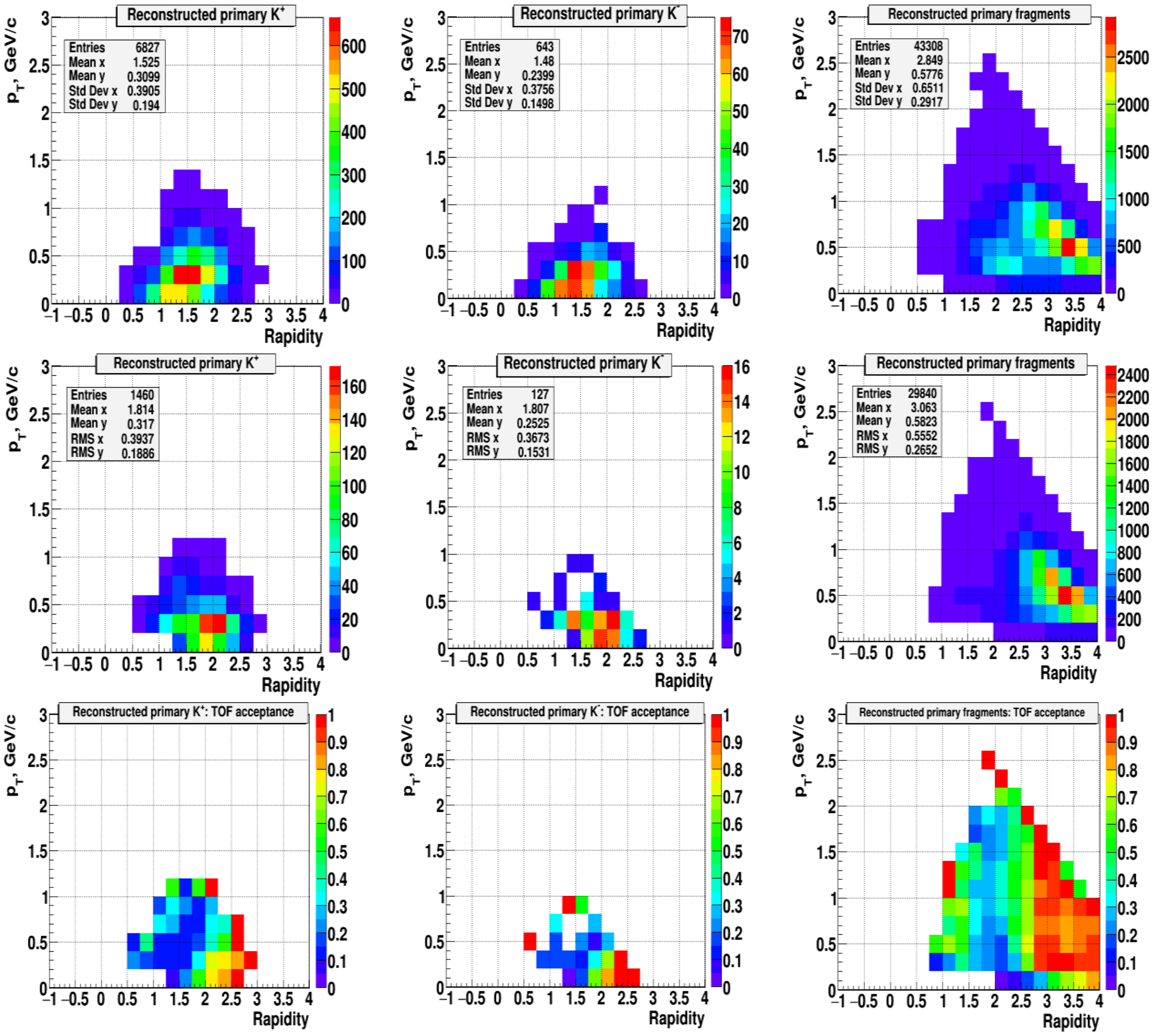

Fig. 2.15: Reconstructed primary K+ mesons, K- mesons, and fragments (from left to right). Upper row: without MC hit in the TOF detectors, center row: with MC hit in the TOF detectors, lower row: acceptance of the TPF detectors.

The reason for the moderate TOF acceptance is illustrated in figure 2.16. The left picture shows the acceptance of the TOF detectors if there would be no magnet. The right panel depicts the acceptance of the TOF walls for reconstructed protons, extrapolated to the position of the first TOF stations at Z0450 cm, including the material of the magnet, and for a magnetic field of 0.8 T. It is clearly visible, that the magnet coils reduce the vertical acceptance of the TOF detectors, and that part of the protons miss the TOF detectors due to the deflection by the magnetic field.

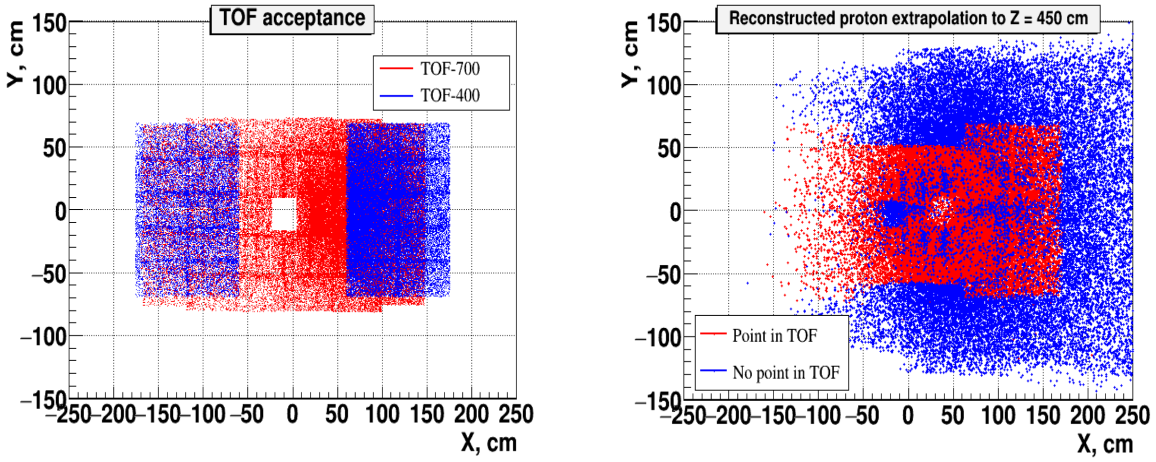

Fig. 2.16: Acceptance of the TOF detectors without magnet (left), and with magnet and a magnetic field of 0.8 T for reconstructed protons, extrapolated to the first TOF detectors at Z=450 cm (right).

2.9 Conclusions

First simulations of track reconstruction in central Au+Au collisions at a beam kinetic energy of 4A GeV have been performed based on the BM@N hybrid tracking system comprising 4 high-resolution silicon sensor stations and 6 GEM stations. Primary produced charged particles are re-constructible, if they produce at least 4 hits in the hybrid tracking system. Their reconstruction efficiency, i.e. the ratio of reconstructed to re-constructible tracks, is 88%. About 47 % of the tracks from primary produced protons and about 30 % of the tracks from primary produced π- mesons have been reconstructed. The momentum resolution of primary tracks is about 0.6% for particles with momenta above 0.5 GeV/c.

The primary protons and pions have been identified by MC information. In the future, particles will be identified via their time-of-flight measured by the BM@N TOF detectors. As a first step, the MC hits in the TOF have been used in the analysis to determine the geometrical acceptance of the TOF detectors. Due to the limited height of the magnet gap, and the deflection by the magnetic field, only 57 % of the protons reconstructed by the hybrid tracking system produce a hit in the TOF detectors. Due to their finite live time, for pions and kaons the acceptance is further reduced to about 25 % and 20%, respectively. The total acceptance including TOF geometry is 27 % for produced protons, and 8 % for produced π- mesons. About 10% of the produced lambdas could be reconstructed and identified by determination of their decay vertex, without MC information on the daughter particles. The invariant mass resolution of the lambdas is σ = 1.1 MeV/c^2, the signal-to-background ratio is S/B = 5.2.

The next step would be to use the information on the time-of-flight in the simulations for particle identification, based on a realistic detector response and track matching between the GEMs and the TOF detectors.

2.10 Running scenario

The ultimate goal of the BM@N research program on the study of the nuclear EOS would be to measure the excitations functions for the production of Λ, Ξ^-, and Ω^- hyperons in central Au+Au and central C+C collisions for beam kinetic energies of 2A, 3A, and 4A GeV. Based on the yield estimates from statistical model predictions (A. Andronic, private communication) as listed in Table 2.1, a running scenario for the first years of data taking is proposed in the following. However, it should be noted, that predictions from modern transport models like UrQMD, PHSD and PHQMD predict for central Au+Au collisions at 4A GeV lower multiplicities for multi-strange hyperons, about a factor of 2 for Ξ^-, and about a factor of 20 less for Ω^- hyperons. For 2A GeV and 3A GeV no transport model predictions are presently available. Therefore, at least the numbers on Ω^- hyperons are affected by a large uncertainty.

Table 2.1: Multiplicities and weekly yields of hyperons produced in central Au+Au collisions according to a statistical hadronization model (A. Andronic, private communication). The kinetic beam energies are indicated, the collision rate is 10 kHz. The yield predictions take into account the efficiency estimates (ε(Λ) = 10%, ε(Ξ) = ε(Ω) = 1%) and the respective branching ratios.

E (A GeV)	M(Λ)	M(Ξ^-)	M(Ω^-)	Λ/week	Ξ^-/week	Ω^-/week
2	0.15	$2.6 \cdot 10^{-4}$	$9 \cdot 10^{-8}$	$5.8 \cdot 10^{7}$	$1.6 \cdot 10^{4}$	3.7
3	0.75	$5.7 \cdot 10^{-3}$	$1.3 \cdot 10^{-5}$	$2.9 \cdot 10^{8}$	$3.4 \cdot 10^{5}$	530
4	3.8	0.11	$2 \cdot 10^{-3}$	$1.5 \cdot 10^{9}$	$6.6 \cdot 10^{6}$	$8.2 \cdot 10^{4}$

Expected results year 1:

Based on table 2.1, the following running scenario is conceivable for the first year: Four weeks of Au+Au collisions at 4 (or 4.5) A GeV with a limited beam intensity of 10^5 Au ions/s. This will reduce the weekly yields listed in table 2.1 by a factor of 10. The harvest of this measurement will be high statistics data for Λ and Ξ^- hyperons. The yield of Ω^- hyperons will depend on their production cross section. Both the yield of multi-strange hyperons and the collective flow of identified baryons including hyperons are expected to be sensitive to the EOS. By comparison of these data to modern transport models, first information on the high-density EOS can be extracted. An even more spectacular result of the first year of data taking would be the measurement of a large amount of hypernuclei such as $_{\Lambda}{}^{3}$H, $_{\Lambda}{}^{4}$H, and $_{\Lambda}{}^{4}$He (see table 2.2). These data will provide new and precise information on the lifetime of hyper-hydrogen. Taking into account interruptions and limitations in Au beam intensity, the time to perform the measurement might be longer, or the yield will be reduced.

Table 2.2: Multiplicities of hypernuclei produced in central Au+Au collisions at a beam kinetic of 4A GeV according to statistical model, reaction rate 1 kHz, ε = 1%, branching ratio = 0.64

Hypernucleus	Multiplicity	yield/week
$_{\Lambda}{}^{3}$H	10^{-2}	$3.8 \cdot 10^{4}$
$_{\Lambda}{}^{4}$H	10^{-3}	$3.8 \cdot 10^{3}$
$_{\Lambda}{}^{4}$He	10^{-3}	$3.8 \cdot 10^{3}$

Expected results year 2:

In the second year the hyperon production excitation function in Au+Au collisions could be completed, by measuring 2 weeks at 3A GeV, and 2 weeks at 2A GeV with a beam intensity of 10^6 ions/s. Depending on the In case of the availability of higher beam intensities, also a substantial amount of Ω^- hyperons could be collected.

Another 2-3 weeks of beam time should be devoted to the measurement of hyperon production in C+C collisions at a beam kinetic energy of 4A GeV with a beam intensity of 10^6 ions/s or more, if possible. The C+C data serve as a reference measurement to the Au+Au data, and will help to improve the determination of the nuclear incompressibility. The hyperon yields from C+C collisions are not supposed to depend on the EOS, in contrast to the yields from Au+Au data. Therefore, the hyperon ratio (Au+Au)/(C+C) is very sensitive to the EOS, as the systematic errors on the hyperon yields both from experiment and model calculation will be reduced. As an example, the Λ and Ξ^- yields calculated with the PHQMD transport model are shown in Table 2.3 for a soft and a hard EOS, for collisions at a beam kinetic energy of 4A GeV. As mentioned above, the yield of Ξ^- hyperons in central Au+Au collisions in table 2.1 (statistical hadronization model) is twice as high as in table 2.3 (PHQMD transport model), whereas the yield of Λ hyperons agree for both models. The experimental challenge will be to identify Ω^- hyperons in C+C collisions, which would substantially help discriminate the soft from the hard EOS (see figure 1.4).

Table 2.3: hyperon yields per week and multiplicity ratios from central Au + Au collisions over central C + C collisions at beam kinetic energies of 4A GeV (corrected for the atomic number) for a soft and a hard equation of state (EOS) as predicted by the PHQMD transport model. The yield predictions are based on a collision rate of 10 kHz, and take into account the efficiency estimates (ε(Λ) = 10%, ε(Ξ) = 1%), and the branching ratios.

EOS	Λ/week Au+Au	Ξ^-/week Au+Au	Λ/week C+C	Ξ^- /week C+C	M(Λ)Au/ M(Λ)C ·12/197	M(Ξ^-)Au/ M(Ξ^-)C ·12/197
soft	$1.5 \cdot 10^9$	$4.1 \cdot 10^6$	$4.0 \cdot 10^7$	$2.6 \cdot 10^4$	2.3	9.6
hard	$1.4 \cdot 10^9$	$3.1 \cdot 10^6$	$4.2 \cdot 10^7$	$3.0 \cdot 10^4$	2.0	6.3

In addition to the hyperons, also hypernuclei will be measured in C+C collisions. These data will allow to find out which collision system (heavy or light) is best suited to produce He, Li, Be, B and C hypernuclei. To this end, also C+Au collisions should be investigated in an exploratory run over a few days.

3 Radiation environment

Measurements with gold beams up to intensities of $2 \cdot 10^6$ ions/s with the BM@N experiment require a well focused beam in order to minimize reactions of the beam with beam pipe and the silicon detector stations. Presently, the beam line from the Nuclotron to the experiment includes air gaps and beam monitors which cause substantial multiple scattering of the beam, which results in a broad beam profile. Moreover, the present BM@N experiment has no beam line downstream the target, and the beam reacts with air inside the magnet. The reactions of the beam with materials of the beam pipe, target chamber or detectors create a significant background of delta electrons hitting the detectors. In order to study the effect of this background radiation on the detector performance, simulations with the FLUKA code have been performed. The FLUKA code calculates the interaction of the beam with materials, and simulates nuclear reactions using an RQMD event generator.

3.1 Beam from the Nuclotron

In the first study, a Gaussian beam profile with a sigma of 1 cm at the target and a divergence of 1 mrad was assumed, corresponding to the presently existing Nuclotron beam. It turns out, that this beam will create a huge flux of up to 10^6 charged particles per cm^2 and second, even with an evacuated target chamber and beam pipe downstream of the target. These particles are mainly delta electrons, which are produced in the beam pipe by the tail of the wide beam profile. The main reasons for the bad beam quality are air sections with beam monitors in the beam line from the Nuclotron to the experiment. It is expected, that the width of the beam profile can be reduced from a sigma of 1 cm down to a sigma of 0.35 cm, when the air gaps and the beam monitors in the beam line are removed. Therefore, FLUKA simulations have been performed to study the effect of the reduced beam width.

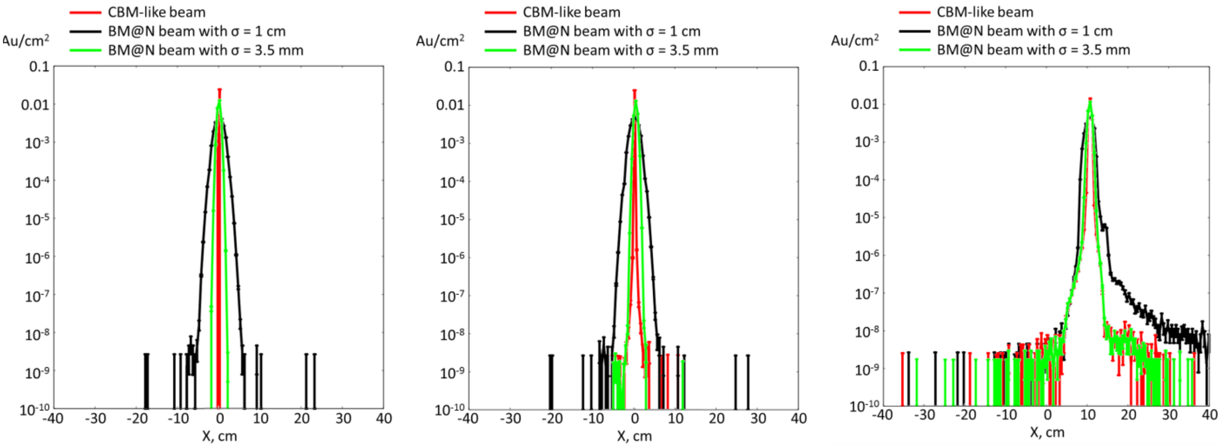

Fig. 3.1: Horizontal beam distribution for 3 different beam profiles: Gaussian shape with a sigma of 1 cm and a divergence of ± 1mrad (black line), a sigma of 0.35 cm and a divergence of ± 1mrad (green line), and for a beam of rectangular shape of size x = y = 0.6 mm with a divergence of 1.7 mrad (red line). The distributions are shown at the target (left), at 30 cm downstream the target (center), and at 4.2 m downstream the target (right).

Figure 3.1 depicts the comparison of the beam profiles in x-direction for a sigma of 1 cm and a divergence of ± 1mrad, a sigma of 0.35 cm and a divergence of ± 1mrad, and for a beam of rectangular shape of size x = y = 0.6 mm with a divergence of 1.7 mrad ("CBM-like beam"). The profiles are shown at the position of the target (left panel), at the position of the first STS station 30 cm downstream the target (center panel), and at 420 cm downstream the target where the Projectile Spectator Detector will be located (right panel). The simulations have been performed for an Au beam with a kinetic energy of 5A GeV, an intensity of $2\cdot10^6$ ions/s, and a 1% interaction Au target

The charged particle density rates in the four silicon detector stations are shown in figure 3.2. The upper panel depicts the result for the beam with sigma 1 cm, the center panel corresponds to the beam with sigma 0.35 cm, and the rectangular beam of size x = y = 0.6 mm is shown in the lower panel . Due the wide beam profile for sigma 1 cm, the beam scatters in the beam pipe and creates delta electrons, which are focused into a vertical area of a width in x of about 10 cm. In this area, the electron density rate is about 10^6 /cm^2/s. For the narrower beam profile with sigma 0.35 cm, the delta electrons are mainly produced in the target, and hit predominantly the first STS detector at 30 cm downstream the target, generating the horizontal distribution in the center and lower panel of figure 2. In the subsequent STS layers at 40, 50 and 60 cm downstream the target, the yield of delta electrons is already drastically reduced down to hit densities between 100 and about 5000 charged particles per cm^2 and sec. These distribution are very similar to the ones produced by the "CBM-like" beam with rectangular shape of size x = y = 0.6 mm with a divergence of 1.7 mrad.

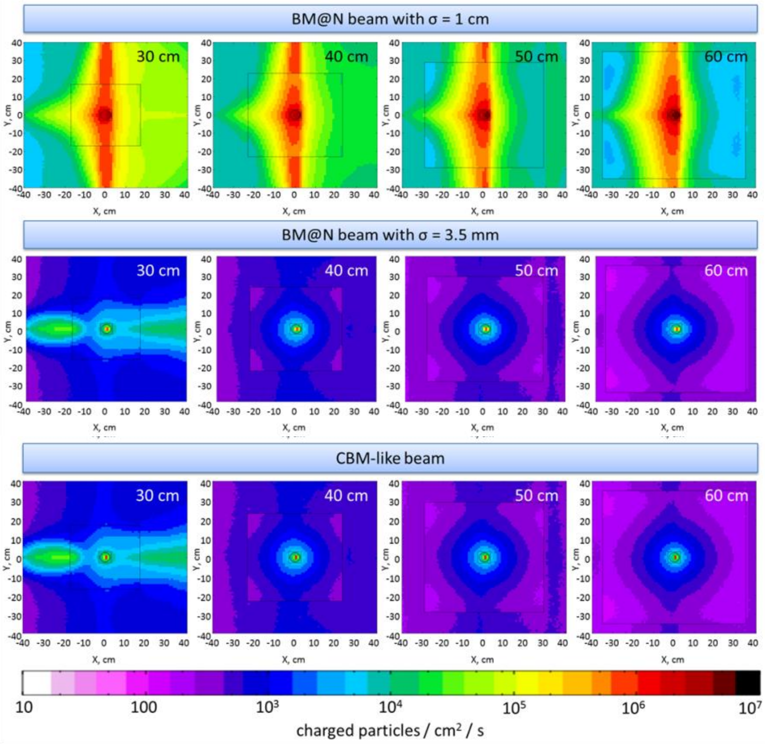

Fig. 3.2: Charged particle densities in the four STS stations for the present Nuclotron beam ("BM@N beam with σ = 1 cm", upper panel), for a narrower beam profile ("BM@N beam with σ = 3.5 mm, center panel), and for a beam of rectangular shape of size x = y = 0.6 mm with a divergence of 1.7 mrad ("CBM-like beam"). The simulations have been performed for an Au beam with a kinetic energy of 5A GeV, an intensity of $2\cdot10^6$ ions/s, and a 1% interaction Au target.

The charged particle distributions in a plane 2m downstream the target, where the GEM detectors are located, are shown in figure 3.3 for the Gaussian beam profile with sigma = 1 cm (upper panel), for the Gaussian profile with sigma = 0.35 cm (center panel), and the rectangular profile (lower panel). The hit densities produced by the beam with sigma 1 cm reach values up to 10^5 /cm^2/s, which will cause GEM channel dead times between 48% and 96%, depending on the strip area. The particle densities produced by the narrower beam profiles are about 100 times lower, and can be tolerated.

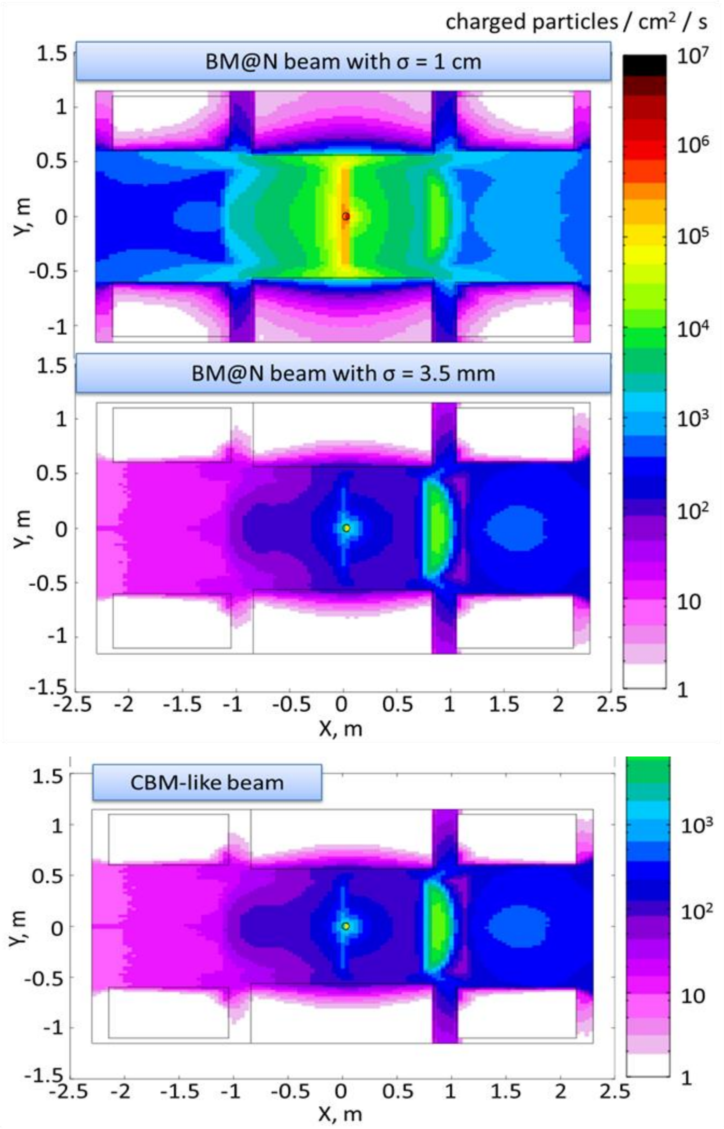

Fig. 3.3: Charged particle densities at a distance of 2 m downstream the target where the GEM tracking stations are located, for the present Nuclotron beam (“BM@N beam with σ = 1 cm”, upper panel), for a narrower beam profile (“BM@N beam with σ = 3.5 mm”, center panel), and for the rectangular beam (“CBM-like beam” of size x = y = 0.6 mm).

The simulations have been performed for an Au beam with an intensity of $2{\cdot}10^6$ ions/s. In conclusion, if the width of the Nuclotron beam profile can be reduced to a sigma of 0.35 cm or better, for example by eliminating the air gaps of the beam line and installing beam monitors which can be removed during operation of the experiment, measurements with Au beams up to intensities $2{\cdot}10^6$ ions/s will become possible.

3.2 Conceptual design of a beam pipe downstream the target

Based on the geometry and material of the target chamber and beam pipe as proposed by Vladimir Spaskov, FLUKA calculations have been performed for an Au beam with a kinetic energy of 4.5A GeV, a profile with a width of $\sigma = 3.5$ mm, a divergence of 1mrad, and an intensity of $2 \cdot 10^6$ ions/s. The calculations take into account that the beam will already be deflected by the magnetic field before it hits the 250 μm thick Au target which is located 124.5 cm upstream the center of the magnet. The magnetic field corresponds to a current of 1800 A.

The geometry of the target chamber together with the first part of the beam pipe is shown in the upper part of figure 3.4. Both the target chamber and the beam pipe are made of 1mm thick carbon fiber. The target chamber has an outer diameter of 66 mm, whereas the first part of the beam pipe with a length of 40 cm has a diameter of 48 mm. The kink angle between the target chamber and the first part of the beam pipe is 0.72°. The subsequent beam pipe is shown in the lower part of figure 3.4.

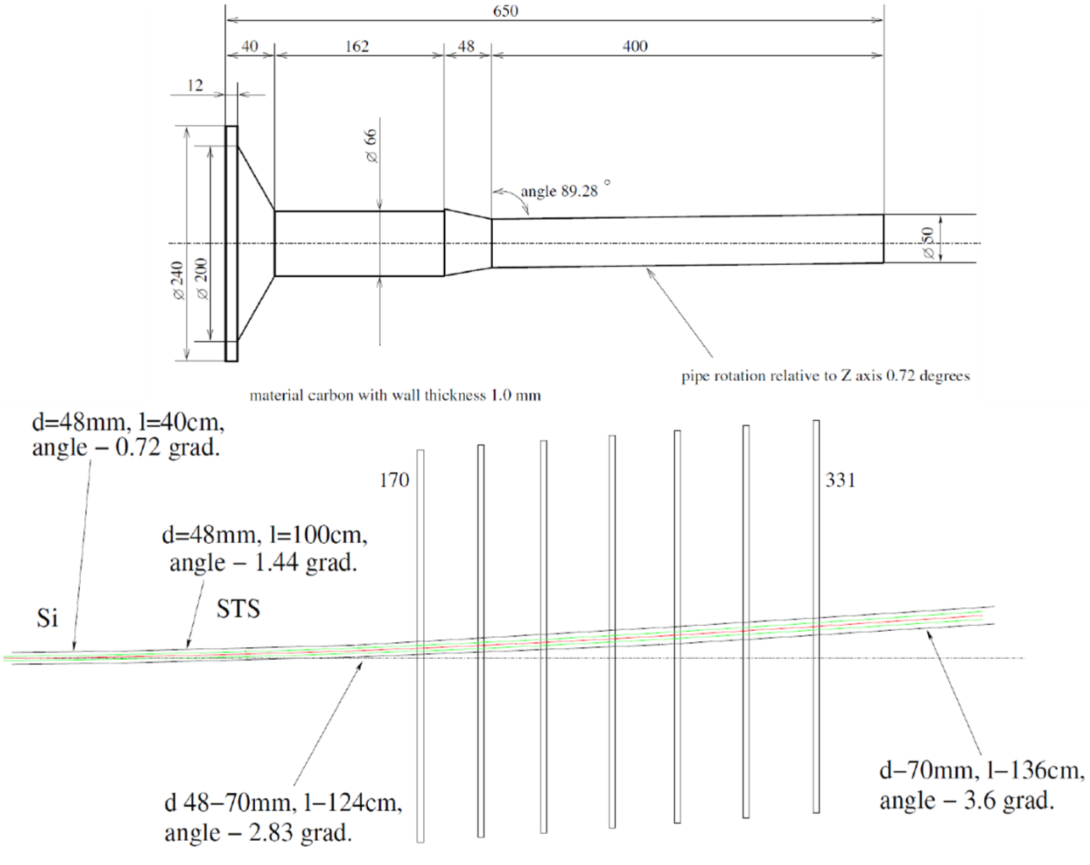

Fig. 3.4: Proposed target chamber and beam pipe of the BM@N experiment. Upper panel: target chamber and the first 40 cm of the beam pipe. Lower panel: Subsequent part of the beam pipe. Target chamber and beam pipe is made of Carbon fiber with a wall thickness of 1 mm.

First results of the FLUKA calculation are shown in figure 3.5. The upper panel illustrates the deflection of the beam and the shape of the beam pipe in the horizontal X-Z plane, while the lower panel depicts the intensity distributions in the X-Y plane for different Z positions. The results demonstrate that the curvature and the increasing diameter of the proposed beam pipe is well suited to guide the high intensity beam, and to minimize radiation outside the pipe. Please note, that the FLUKA calculation takes into account the divergence of the beam, the multiple scattering in the target, and the reactions of the beam in the material of the beam pipe.

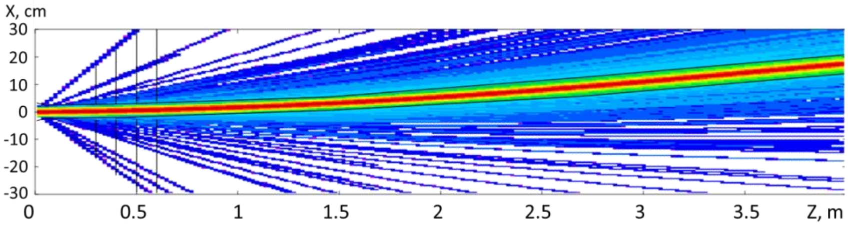

Fig. 3.5: Projection of the Au ions into the X-Z plane illustrating the beam deflection. Results of FLUKA calculations for an Au beam with a kinetic energy of 4.5A GeV, a profile with a width of σ = 3.5 mm, and a divergence of 1mrad.

3.3 Radiation level in the detector regions

The charged particle densities in the four silicon stations are shown in figure 3.6. The charged particle rate densities reach values from about 0.5 kHz/cm^2 at the perimeter of the detector, to about 5 kHz/cm^2 for the innermost sensors. Based on the strip size of the sensors of 50 μm · 6 cm = $3 \cdot 10^{-2}$ cm^2, and the channel read-out time of maximum 1 μs, one can estimate channel inefficiencies between $1.5 \cdot 10^{-5}$ for the vast majority of the sensors, and $1.5 \cdot 10^{-4}$ for the sensors close to the beam pipe.

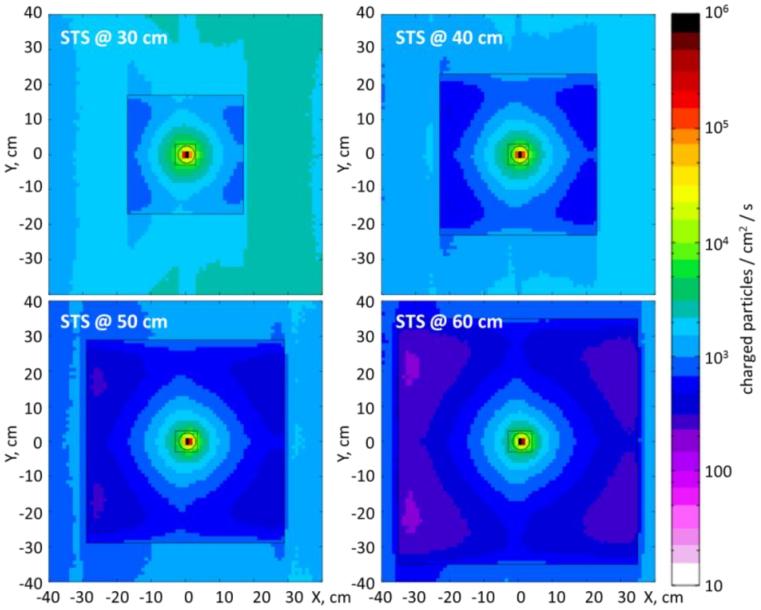

Fig. 3.6: Distributions of rate densities for charged particles hitting the four silicon stations in minimum bias Au+Au collisions at a beam kinetic energy of 4.5A GeV and an intensity of $2 \cdot 10^6$ ions/s. The beam has a width of σ = 3.5 mm, a divergence of 1mrad, and hits a 1% interaction Au target. The FLUKA calculation take into account a target chamber and a beam pipe as sketched in figure 3.4.

The ionizing dose and the equivalent neutron fluence in the regions of the detectors downstream the target is illustrated in figure 3.7 and 3.8, respectively, both in the top view (left panels) and in a side view (right panels). The intensive flux in the bending plane is caused by delta electrons created in the target. In the experiment, these delta electrons have to be stopped by a lead layer around the target chamber, in order to shield the barrel detector, which serves for centrality determination and triggering. Detailed simulations are necessary for the design of this shielding layer.

In the region of the silicon stations, the ionizing dose reaches values of about 10 Gy after 2 month of beam on target. Assuming a total running time of the BM@N experiment of 5 years and 4 months per year, a dose of about 100 Gy is reached, resulting in a mild damage of the sensors in the inner part of the stations. The equivalent neutron fluence in the silicon stations reaches values below 10^{10} n_{eq}/cm^2 after 2 months, corresponding to a life time fluence of 10^{11} n_{eq}/cm^2, which is well within the radiation tolerance of the sensors.

In the region of the GEM stations, the ionizing dose reaches values of about 1 Gy after 2 month of beam on target, corresponding to a life time dose of 10 Gy. The equivalent neutron fluence in the GEM stations reaches also values below 10^{10} n_{eq}/cm^2 after 2 months, corresponding to a life time fluence of 10^{11} n_{eq}/cm^2. Both values can be tolerated by the GEM detectors.

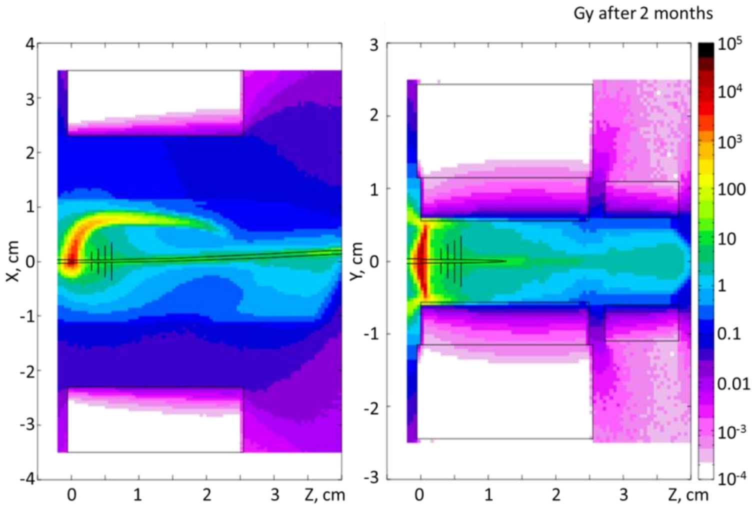

4

Fig. 3.7: Ionizing dose in Gray in the horizontal (left panel) and vertical plane (right panel) along the beam after two months of running with an Au beam of 4.5A GeV with an intensity of 2·10⁶ ions/s.

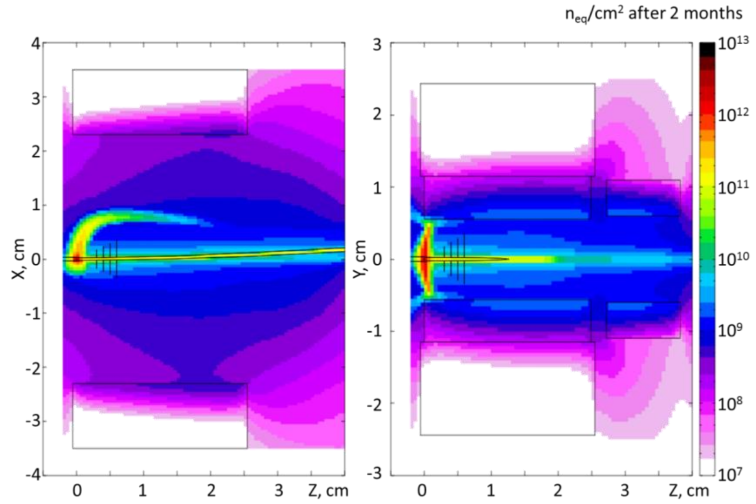

Fig. 3.8: Equivalent neutron fluence n_{eq}/cm^2 in the horizontal (left panel) an vertical plane (right panel) along the beam after two months of running with an Au beam of 4.5A GeV with an intensity of $2 \cdot 10^6$ ions/s.

4 The Silicon Tracking System

4.1 Layout of the Silicon detector stations and system components

The Silicon Tracking System (STS) of the BM@N consist of four stations equipped with a total number of 292 double-sided micro-strip sensors providing information on exact place, time and energy released by the particle passing through a sensor. The sensors have two sizes 42 mm x 62 mm, and 62 mm x 62 mm, and a thickness of 320 ± 15 μm. Each sensor has 1024 strips on each side with a strip pitch of 58 μm. The n-side has straight strips, the p-side has strips with a stereo angle of 7.5°, corresponding to a "pixel of size Δx = 58 μm times Δy = 58 μm/tan(7.5°) = 440.6 μm for a two-coordinate spatial measurement. The edge strips are connected via a second metallization layer.

The 2048 strips of each sensor are out simultaneously by 2 Front-End Boards (FEBs) connected to the P and N sides of a sensor. Readout electronics is connected to the strips of a sensor with the help of low-mass aluminum flat cable. This makes it possible to allocate the complicated and radiation sensitive circuits of the readout electronics at considerable distance outside of the sensitive area of the detector operating in high radiation field. Each sensor is connected via 32 cables with 64 lines each to 16 read-out ASICs with 128 channels each, which are placed on the 2 cooled FEBs with 8 ASICs each. This sensor-cables-FEBs system is called a module. Several modules are mounted on ultralight space-frames made of high modulus carbon fiber, to make up the STS super-module, the so called "ladder". The stations 1, 2, 3, and 4 comprise 24, 52, 64, and 104 modules with sensors of size 62x62mm^2. In the inner part of each station, 8 modules with sensors of size 42x42mm^2 are located, and 4 modules with sensors of size 42x42mm^2 with cut edges close to the beam pipe. The layout of the stations is shown in figure 4.4.1, and the number and size of the sensors in each station is listed in table 4.4.1.

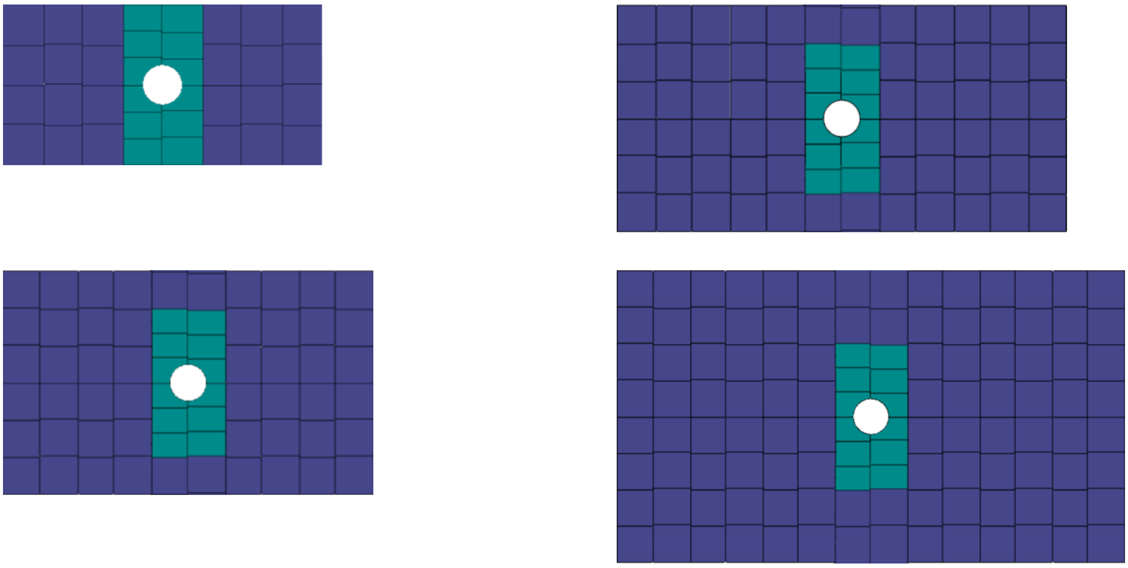

Fig. 4.1.1: Layout of the Silicon Tracking System with sensors of size 42 x 62 mm^2 (green) and 62 x 62 mm^2 (blue). The active area increases from 24.8 x 49.6 cm^2 (station 1, upper left), 37.2 x 62 cm^2 (station 2, lower left), 37.2 x 74.4 cm^2 (station 3, upper right) to 49.6 x 86.8 cm^2 (station 4, lower right), covering a total area of 1.06 m^2.

Table 4.4.1: Number and size of the sensors in each station

STS Station	**Number of sensors**	**Size of sensors**
1	24	62 x 62 mm^2
	8	42 x 62 mm^2
	4 (cut)	42 x 62 mm^2
2	52	62 x 62 mm^2
	8	42 x 62 mm^2
	4 (cut)	42 x 62 mm^2
	0	22 x 62 mm^2
3	64	62 x 62 mm^2
	8	42 x 62 mm^2
	4 (cut)	42 x 62 mm^2
	0	22 x 62 mm^2
4	104	62 x 62 mm^2
	8	42 x 62 mm^2
	4 (cut)	42 x 62 mm^2
	0	22 x 62 mm^2

The arrangement of the stations is shown in figure 4.1.2. The first station is located 30 cm downstream the target, the distance between the station will be 20 cm. The figure shows the low-mass carbon ladders with the cooled front-end electronic boxes at the upper and lower end.

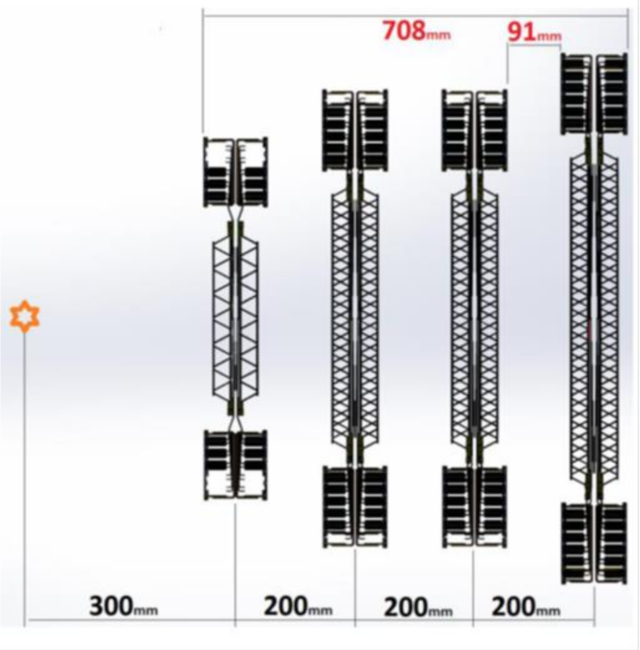

Fig.4.1.2: Arrangement of the silicon stations

Figure 4.1.3 depicts the hit density per cm^2 and event in the 4 stations, calculated for central Au+Au collisions at 4A GeV, assuming the STS configuration with a relative station distance of 15 cm. The hit density is below 0.02 hits/cm^2/event. For an inner sensor of size 42 x 62 mm^2 this value corresponds to a strip occupancy of about $5{\cdot}10^{-4}$ per event.

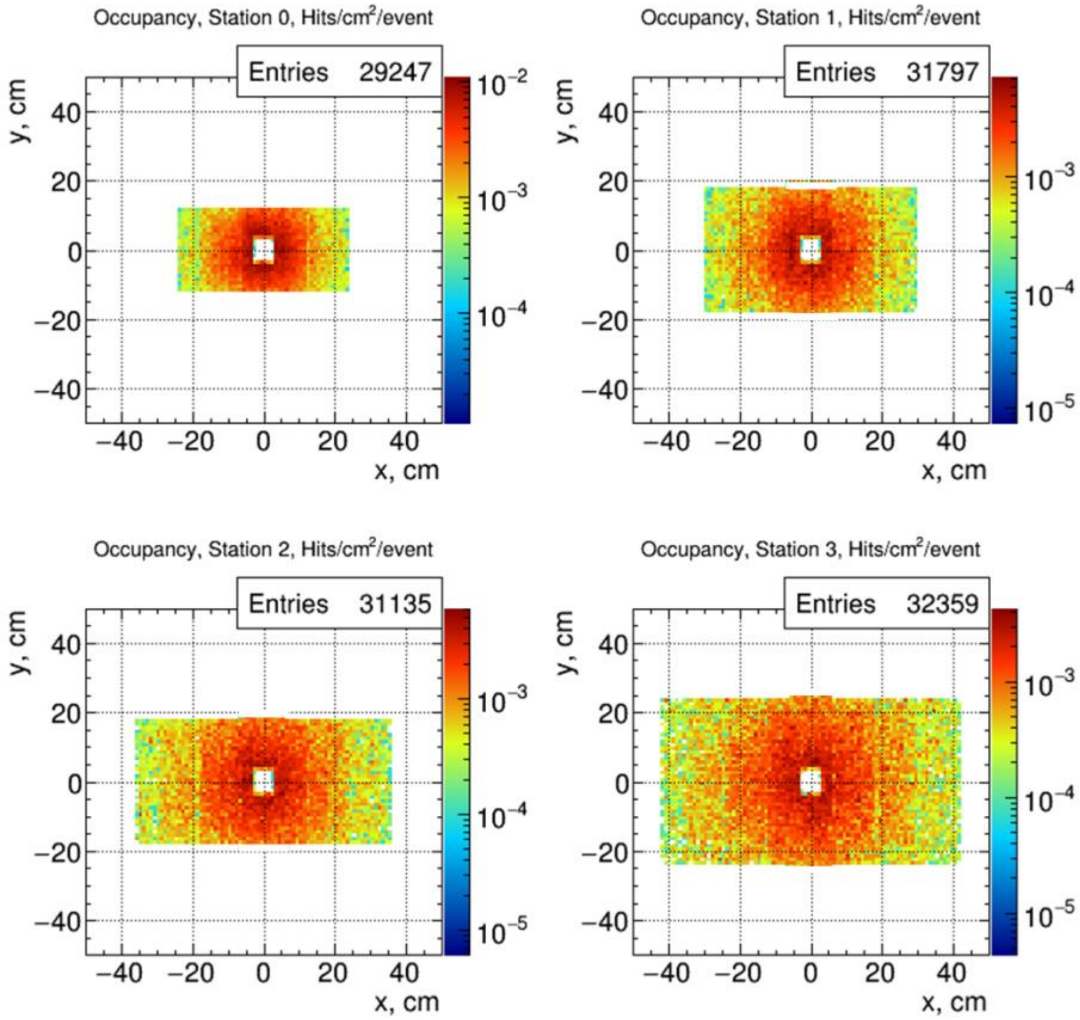

Fig.4.1.3: Hit density per cm² and event in the four STS stations with a relative distance of 15 cm.

The sensors on the ladders overlap by 1 mm to cover the dead area at the edges of the sensors. The ladders in the center of the stations form a semi-circle opening which will finally, when all stations installed in a mainframe, form a bore in STS for the placement of the vacuum carbon fiber beam pipe transporting the incident beam through the STS to the beam dump.

To make up a plain out of the sensors on the ladders the ladders are first mounted on the C-frames. Four C-frames of two types – right (R) and left (L) are needed to build up a sensitive plain of the STS without dead zones between the left and right edges of the ladders. The readout electronics is mounted inside FEB-boxes, which are in turn mounted on the heat exchangers in the periphery of the stations. Front-end electronics dissipate thermal power, which should be removed from the detector. Dedicated hexid liquid cooling system is being developed, additional thermal shielding of the electronics is also suggested. The different components of the STS are shown in figure 4.1.4.

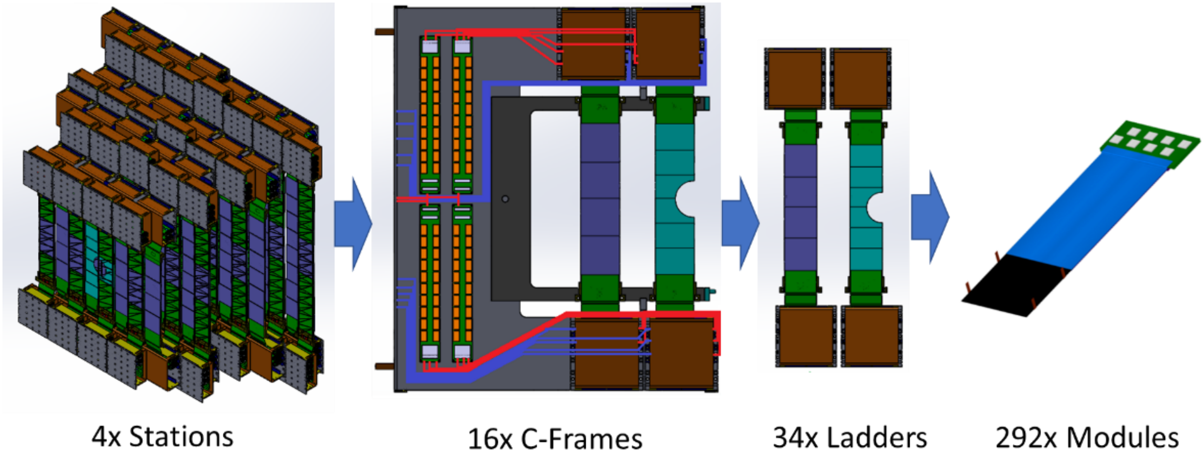

Fig. 4.1.4: Components of four STS stations

Stations are installed inside the mainframe as shown in figure 4.1.5. The mainframe consists of carbon fiber square tubes and walls made of CF sandwich panels with Airex foam inside. The walls serve for the electromagnetic and thermal shielding. The front and back walls of the mainframe have windows around the beam pipe made of low-mass material.

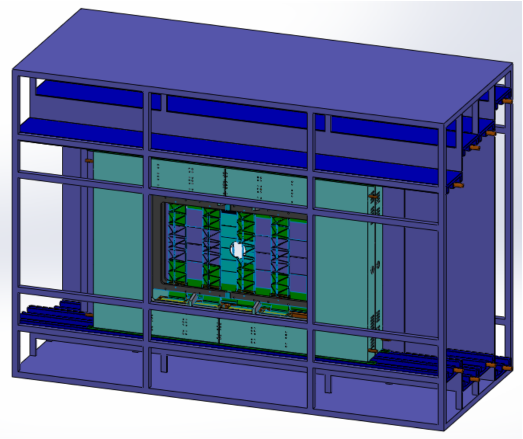

Fig. 4.1.5: STS Mainframe

4.2 Double-sided microstrip sensors

The BM@N Silicon Tracking System will comprise in its four tracking stations 292 double-sided silicon micro-strip sensors in three geometrical shapes, one sensor for each detector module. The majority of the sensors are of rectangular geometry, having the outer dimensions of 6.2 cm width and height of 4.2 and 6.2 cm. The resulting two discrete strip length of about 4 and 6 cm match to the different particle hit density regions in the detector. The smaller sensor variant is also intended in a technical modification with circular cutouts, to be applied in the areas where the beam pipe intersects the tracking stations.

The silicon micro-strip sensors originate from a development done for the Silicon Tracking System [1] of the CBM experiment at FAIR. While the CBM sensors are by now finalized [2] [3] and in series production since mid 2019[1], the sensors for the BM@N-STS have already been acquired in 2016 at the two vendors[2] involved in the prototyping and thus reflect the status during the CBM development then. The BM@N-STS sensors differ from the final CBM-STS sensors in several aspects, mostly concerning the arrangement of biasing contact pads, labeling, guard termination rings, reference markers, thickness of some metal layers, as well as the dicing precision. Also the quality acceptance criteria were more open than those specified for the series production of the CBM-STS. The strip geometry itself is essentially identical. The sensor variant with the circular cutouts does not exist yet. The BM@N team at SINP, Moscow State University, works on their design. Figure 4.2.1 shows prototype silicon micro-strip sensors made in four shapes for the CBM-STS. The two middle-size variants represent those to for application in the BM@N-STS. The following two subsections summarize the sensor technology and the performance of prototypes, mostly referring to the technical documentation published in [2].

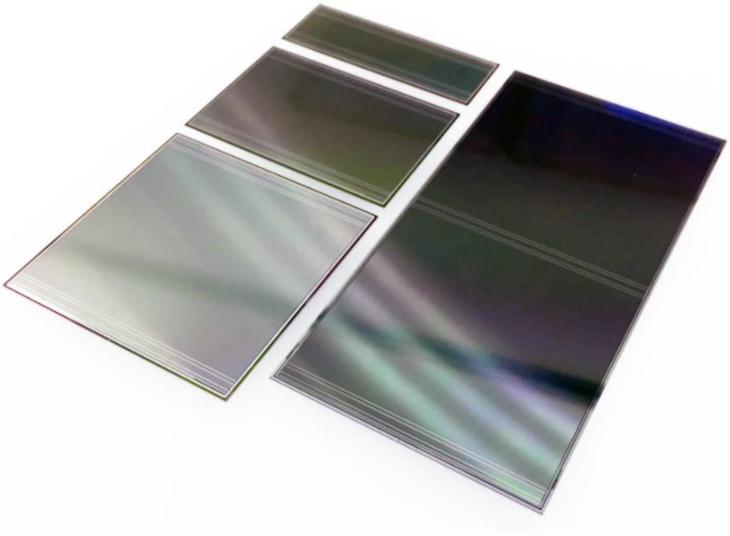

Fig. 4.2.1. Prototype double-sided silicon microstrip sensors in the four basic variants of the CBM-STS, having 1024 strips per sensor side across 6.2 cm width, and strip lengths of 2, 4, 6 and 12 cm. The two middle-sized variants will be used in the BM@N-STS.

---

[1] CBM-STS Sensor Production Readiness Review in 4/2018; series production after tendering at Hamamatsu Photonics from 7/2019 to 11/2020.

[2] CiS Forschungszentrum für Mikrosensorik, Germany, and Hamamatsu Photonics,Japan.

4.2.1 Sensor technology

All sensors are realized in the same technology. Starting from 300-micrometer thick n-type intrinsically doped wafer material (the detailed thickness is manufacturer dependent/order specific), a two-sided segmentation is established in a multi-step planar processing. The result is a structured wafer with strip-like p and n-doped implants just beneath the two surfaces of the wafer, referred to as p and n sides. The p-n-n structures are reversely biased through a combination of polysilicon resistors between every strip and a bias rail surrounding the sensor on both sides, distributing the bias from a few feed-in points. The implants are read out through coupling capacitors integrated into the sensors: separated by a thin silicon oxide layer from the implant, a metal layer extends on top of the implant, ending in a contact pad that can be connected to the electronics read-out channel.

The strip layers are about 20 micrometer wide and repeatedly placed at a pitch of 58 micrometer. The strip length is essentially defined by the sensor chip's height. On the n-doped side, the strips run parallel to the vertical chip edge. On the p-doped side, the strips are inclined by 7.5 degrees forming a stereo angle with respect to the n-side so that particle hits can be determined as space points. The strip pitch and the strip grid essentially define the spatial resolution in the transverse directions of the beam axis. In the module concept of the STS, the sensors will be read out form one edge only. For the p-side strips, the shorter corner strips not reaching the read-out side are interconnected through routing lines on a second metal layer to the matching corner strips in the opposite corner, adding their signals to the read-out channels there. The sensor topology is illustrated in figure 4.2.2.

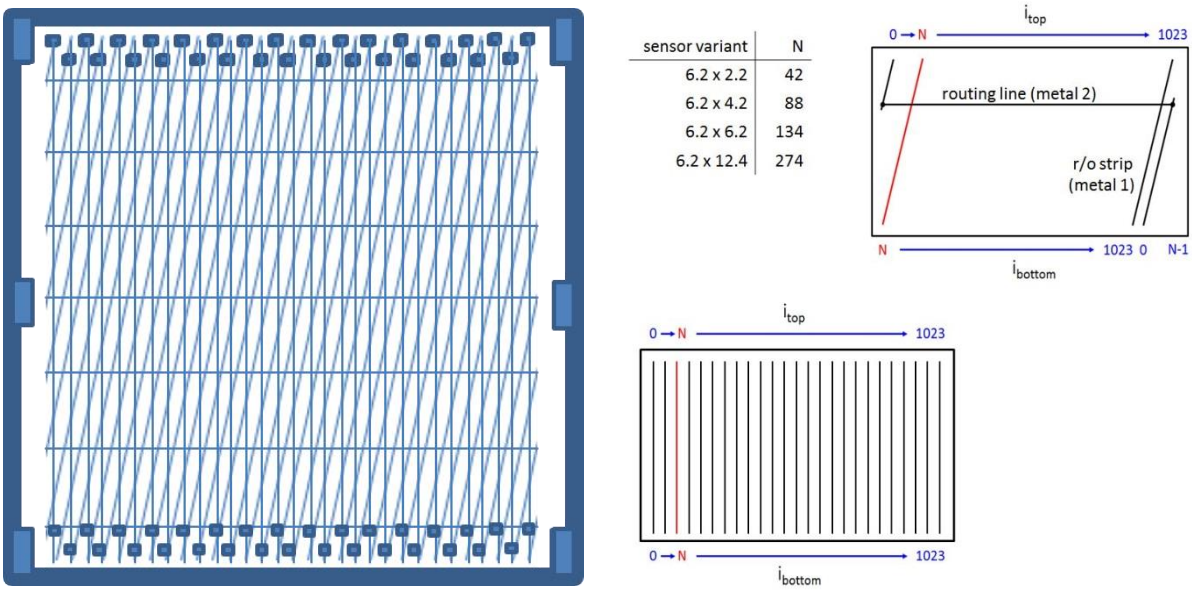

sensor variant	N
6.2 x 2.2	42
6.2 x 4.2	88
6.2 x 6.2	134
6.2 x 12.4	274

Fig.4.2.2 Schematic representation of a STS micro-strip sensor in a see-through view (left) and per side (right). The vertical lines represent the n-side strips, the tilted lines the p-side strips. The horizontal lines are the routing lines that interconnect the short strips of the corners to read-out pads at the top edge where micro-cables and front-end electronics, respectively, are to be connected to. All silicon sensors comprise 1024 strips per side. On the p-sides, additional strips from the corners arise as specified in the table insert. Prototype sensors, evaluation, test results

4.2.2 Prototype sensors, evaluation, test results

4.2.2.1 Layout parameters

Sensors as delivered by the two vendors to JINR are depicted in the close-up photographs shown in Figs.Fig. 4.2.3. The design reflects an early layout of the final design iteration CBM06, optimized in particular for connectivity issues relevant to microcable attachment during module assembly. The wafer material is 285 µm thick at CiS and 320 µm at Hamamatsu. The full specifications are close to those for the CBM series production as provided in [2]. While all positions of the contact pads for signal read-out (the visible two double-rows) and biasing (pads close to the surrounding guard rings) are identical for both vendors, the outer guard ring layout and passive rim with space for labels do differ at that time of development. Furthermore, microscopic differences for layer dimensions, distances and structures exist between the two vendors as their specific design rules apply.

The sensors were delivered as diced objects, i.e. cut out from the production wafers. The dicing precision at CiS, done with diamond blade cutting, is within +15 µm from the scribe line; in practice the precision on prototypes ranged up to +80 µm. Hamamatus uses laser dicing and achieves dicing with precision better than 10 µm, even of the order of few µm. The delivered objects were 6.2 by 6.2 cm sensors from CiS and Hamamatsu, and 6.2 by 4.2 cm sensors from CiS.

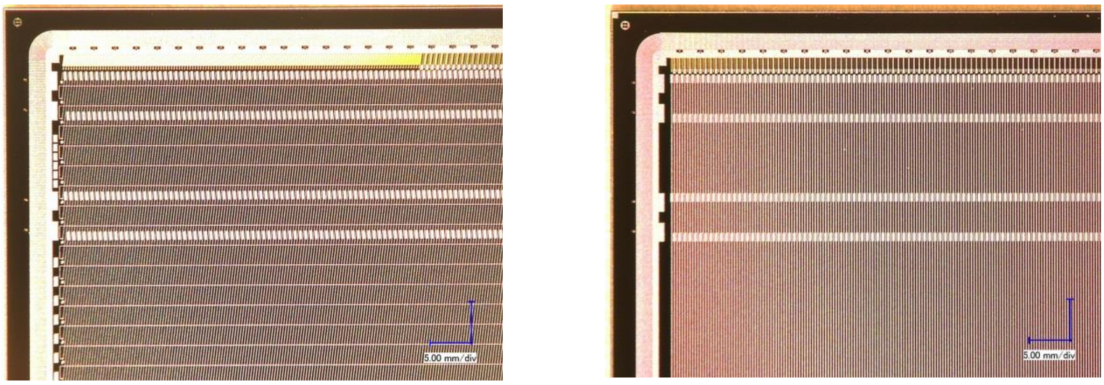

p-side n-side

Fig. 4.2.3 View onto both sides of early prototype sensors of layout CBM06 as produced at CiS, Germany.

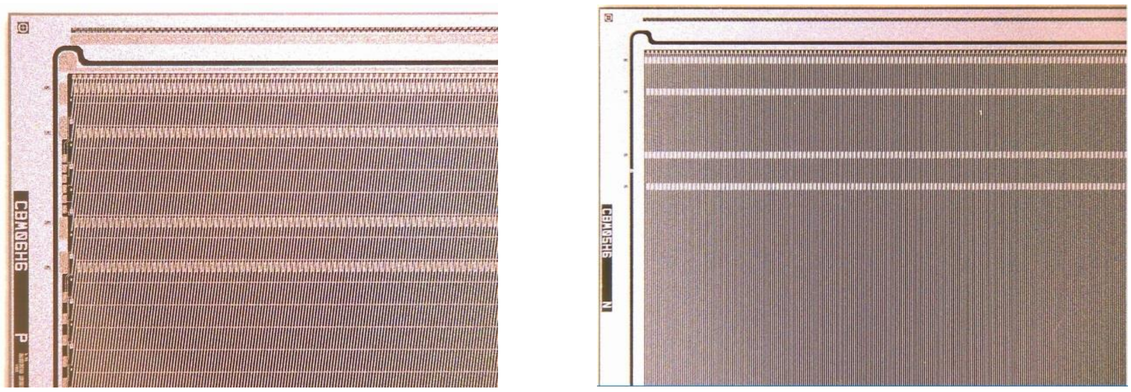

p-side n-side

Fig. 4.2.4: View onto both sides of early prototype sensors of layout CBM06 as produced at Hamamatsu Photonics, Japan.

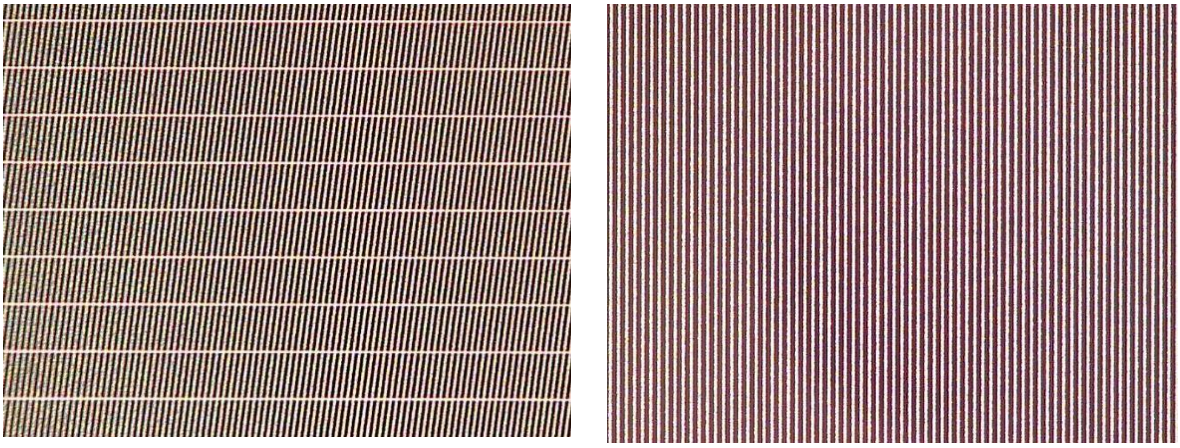

CiS sensor, p-side

Hamamatsu sensor , n-side

Fig. 4.2.5: Strips on the sensors in close-up view. The strip pitch is 58 µm, the strip width about 20 µm, depending in detail on the vendors' design rules.

4.2.2.2 Quality inspection

The sensors delivered to JINR come quality-inspected by the vendor, with a record of global parameters (current-voltage curves) as well as strip-by-strip measurements. The data comprises characterization of the full-depletion voltage, sensor currents as function of the applied reverse bias voltage, and the number of defect strips (by short circuits to neighboring strips, or shorts through the AC coupling layer, or strip interruptions on the read-out layer). However, during the prototyping phase of the sensors the acceptance cuts were still wide open in order to allow for identify of quality compromising effects. Also not all sensors have the full record of all inspections, or the scanning range (e.g. bias voltage) was limited at the vendor. During shipment to the recipient, unpacking and handling there, further damage may occur. Therefore, quality inspection prior to the selection for integration into modules is essential.

A quality inspection station has been set up at JINR. It allows electrical inspection of global and strip-individual parameters and is described in [4]. For the CBM-STS, also optical inspection based on a contactless, focus-based camera survey has been conceived. Typical results from quality inspection are represented in the graphs 4.2.6, 4.2.7, and 4.2.8, showing good performance for system integration.

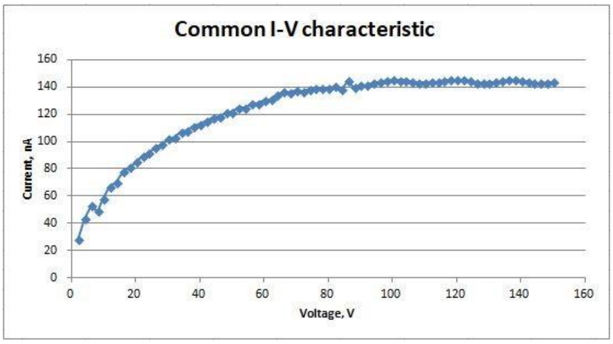

Fig. 4.2.6: Current-Voltage characteristic of a sensor of 6.2 by 6.2 cm at room temperature.

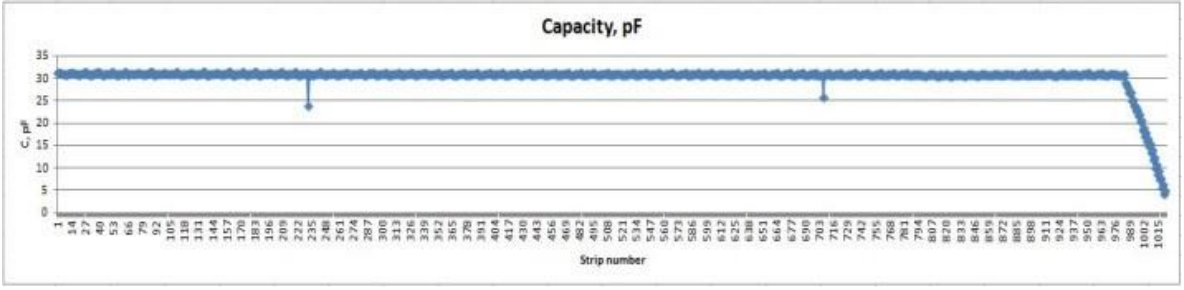

Fig. 4.2.7: Strip-by-strip measurement of capacitance to its neighboring strips reveals potential short circuits or breaks.

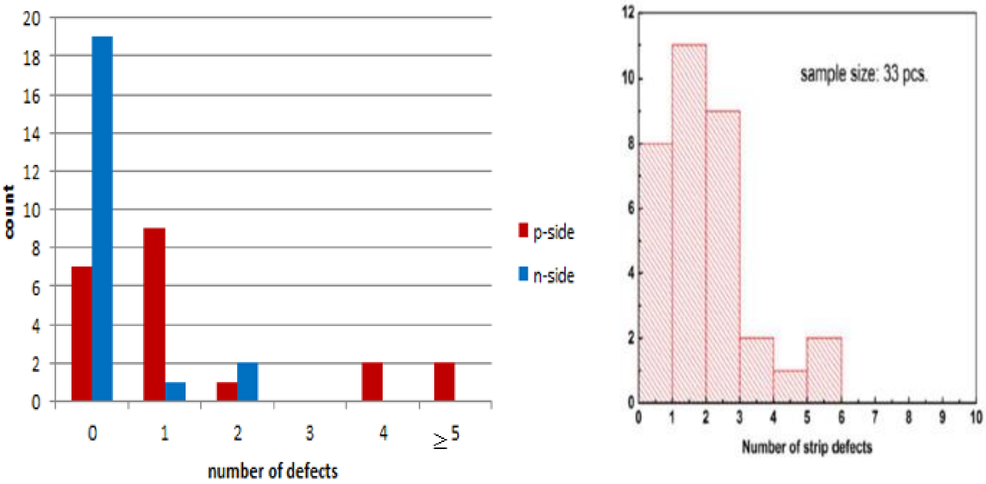

Fig. 4.2.8: Statistics of strip defects on a number of 6.2 by 6.2 cm sensors from CiS (left) and Hamamatsu (right) [2].

4.2.2.3 Sensor performance after irradiation

In the course of sensor development for the CBM-STS, extensive irradiation studies have been carried out with proton and neutron beams, causing ionizing and non-ionizing damage to the silicon lattice or the wafer surface structures. The high-interaction operation of the CBM experiments sets here the stronger radiation tolerance requirements than for the conditions in the BM@N-STS. It could be shown that design, materials, technologies of both CiS and Hamamatsu allow operating the sensors up to 2 × 10^{14} neutrons/cm^2 (1 MeV equivalent) fluence that is considered as the (multi-run) time window for CBM-STS operation before sensor exchange must be foreseen. The measurements extracted from [2] (see figure 4.2.9) show exemplarily that situation. However, charge collection efficiency can be maintained only by limiting sensor currents through cold operation of the sensors, and applying increasingly higher reverse bias along with accumulating fluence. This is a central design aspect of the CBM-STS. Sensor cooling in the BM@N-STS is essentially not required, and system operating conditions therefore more relaxed.

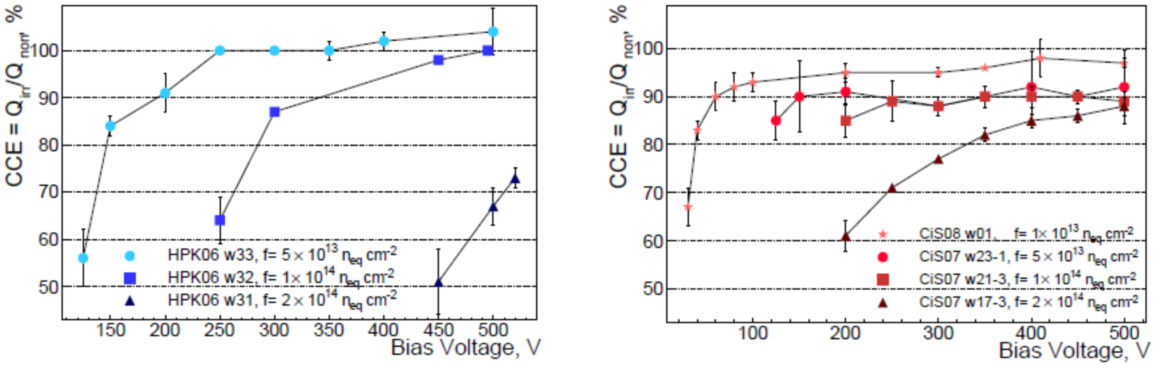

Hamamatsu sensors , p-side CiS sensors , n-side

Fig. 4.2.9: Measurements of charge collection efficiency (ratio of detected charge in irradiated to non-irradiated sensors) for samples of Hamamatsu and CiS sensors [2].

The expected lifetime dose of the BM@N silicon sensors has been calculated with FLUKA calculations based on a realistic material budget of the silicon stations including the beam pipe, for an Au beam with kinetic energy of 4.5A GeV, an intensity of $2\cdot10^6$ ions/s, and an Au target with thickness 250 μm. After 2 months of running, the inner sensors of the stations will receive a fluence (NIEL) of $\leq 10^{10}$ n_{eq} cm^{-2}. After an assumed lifetime of 5 years, each year 4 months beam on target, the integrated dose is about $\leq 10^{11}$ n_{eq} cm^{-2}. According to figure 4.2.10, this value is well below type inversion.

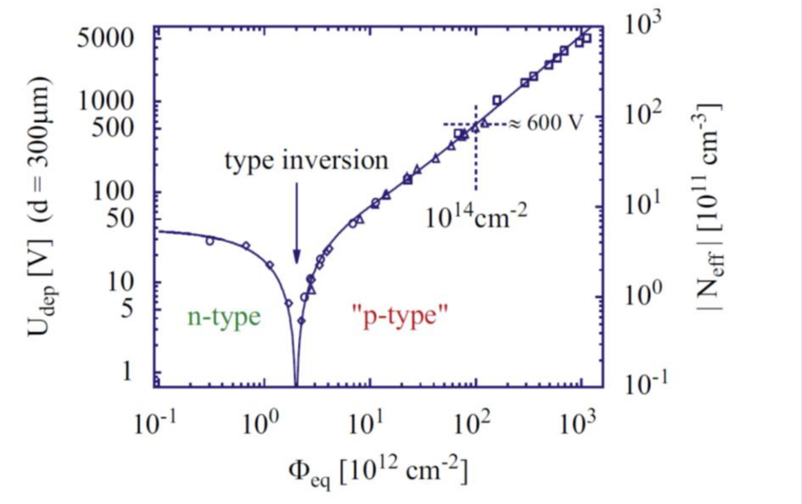

Fig. 4.2.10: Typical evolution of the full depletion voltage (left axis) and the effective doping concentration (right axis) as function of 1 MeV neutron equivalent particle fluence for a silicon sensor of 300 μm thickness.

4.2.2.4 Hit reconstruction efficiency with a STS module in particle beam

The performance of above described prototype silicon microstrip sensors coupled to prototype front-end electronics was determined in-beam with close to minimum ionizing particles. A detector module comprising a non-irradiated sensor and completed by 1/8 of the area of a fully equipped module, was installed in a reference tracking telescope realized from scintillating fiber detection layers (figure 4.2.11 left). It was installed in 2018 on a beamline at COSY, Research Center Jülich, Germany and delivered with 1.7 GeV/c protons. The read-out system of both the silicon module under test and the hodoscopes were fully based on acquiring self-triggered data that was assembled to time-sliced data samples ("events") for analysis. Despite of limited pointing precision of the hodoscope tracks onto the small wedge-shaped front/back overlap area of the read out sensor part, the experiment allowed estimating the hit reconstruction efficiency to > 95% (figure 4.2.11 right), along with determining further operational module parameters.

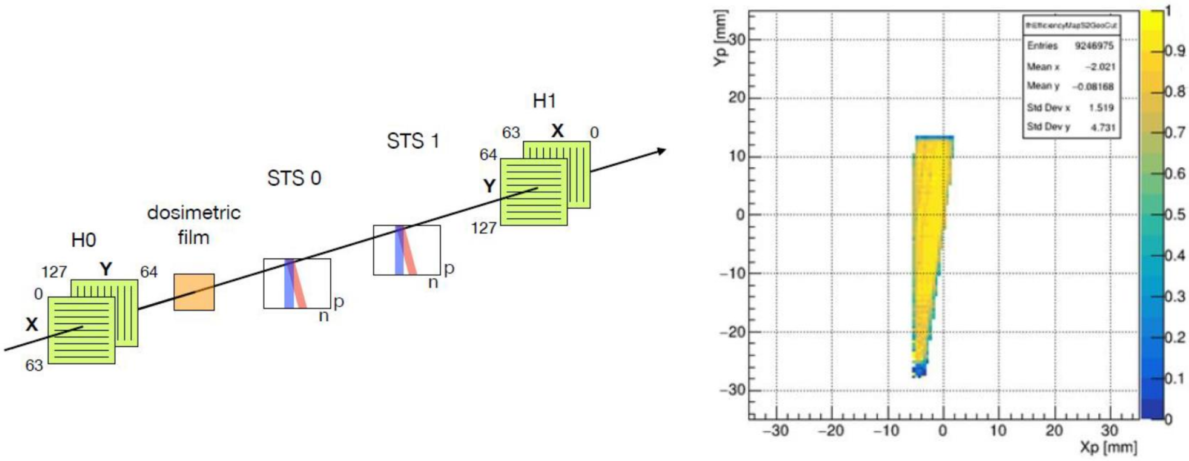

Fig. 4.2.11: In-beam experiment with a test module structure to determine the hit reconstruction efficiency from proton-beam induced signals in a prototype silicion micro-strip sensor coupled to self-triggering prototype front-end electronics of the CBM-STS.

References

[1] J. Heuser et al. (CBM Collaboration), Technical Design Report for the CBM Silicon Tracking System, GSI Report 2013-4

[2] O. Bertini et al., Production Readiness Review for the Silicon Sensors of the CBM Silicon Tracking System, Technical Note CBM-TN-18010

[3] J. Heuser et al., Description of the STS microstrip sensors for series production, Technical Note CBM-TN-19005

[4] A. I. Sheremeteva et al., Progress in STS Sensor Characterization at JINR, in: CBM Progress Report 20

4.3 Read-out cables, evaluation, optimization

Ultra-light micro-cables are one of the key component for the BM@N-STS. Ultra-light read-out micro-cables are used for transfer signals from the sensors to the front end electronics that is mounted outside the fiducial region due to material budget constraints. The central structure is a stack of signal layers, a meshed spacer and shielding [1]. Two signal layers are stacked together with a lateral shift of half the pitch, using an adhesiveless process, to achieve in a long structure a fine effective pitch of about 58 um matching the pitch of the strips on the silicon sensors to which the micro-cable will be tab bonded to. Inner layer is closer to ground than the outer layer. Additional spacer layers are added to the stack. The function of spacer between two signal layers is to reduce the capacitance contributions from the adjacent connecting layers. The spacers are made from polyimide foils structured into a 2/3 mesh to achieve a minimum possible dielectric constant. At the backside an external shielding layer is applied to reduce the noise level and to prevent shorting between the stacks of cables.
The cross-section of a micro-cable is schematically depicted in figure 4.3.1.

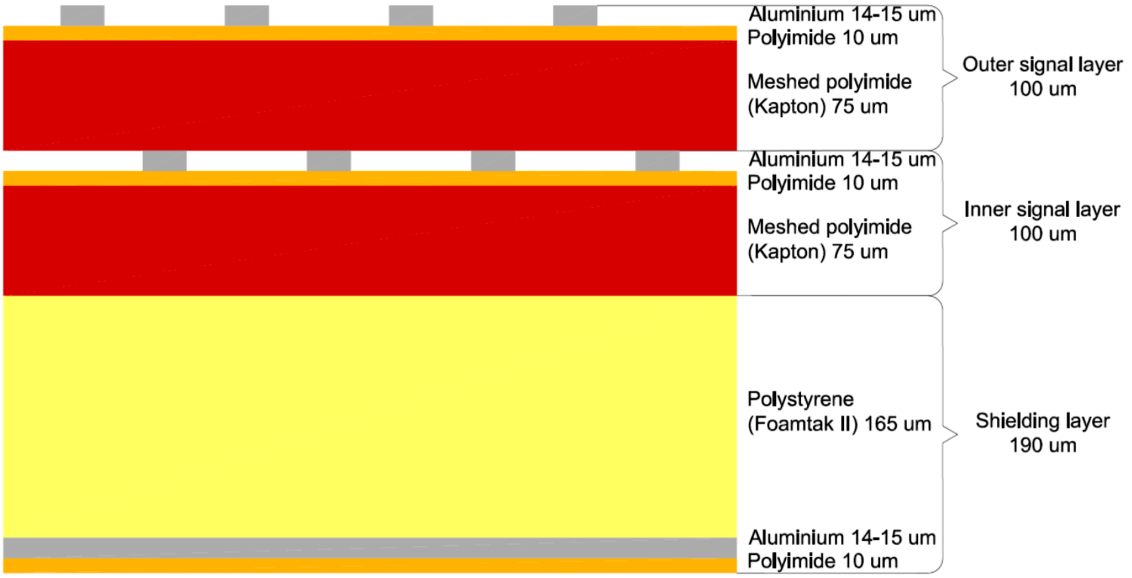

Fig. 4.3.1: Cross-section of a micro-cable.

4.3.1 Material for read-out micro-cables

While selecting a material for fabrication of micro-cables foremost the requirements to minimization of material amount within working volume, as well as requirements to resistance, mutual capacitance of conductors, electric strength and elasticity was reviewed. As the initial micro-cable construction material has been chosen the serially manufactured FDI-type aluminum-polyimide adhesiveless foiled dielectric. The FDI film is polyimide (10 μm thickness) with aluminum film (14-15 μm thickness). Radiation length of aluminum-polyimide micro-cables does not exceed 0,02% of X_0 for one layer ($X_{0\,Al} \approx 8{,}7$ cm, $X_{0\,Pi} \approx 28{,}4$ cm) [2] The. flexible dielectric substrate of the cable affects the capacitance. The material of choice in high-energy applications is polyimide with a dielectric constant of 3,5. This material is radiation-resistant with good mechanical and electrical properties.
The development of the ultra-light read-out cables, made from aluminum traces on polyimide material for minimum material budget, is a particular important task. This

includes the reliable fabrication of fine-pitch traces, matching the strip pitch of the sensors, over lengths up to about 35 cm. The fabrication of the micro-cables is based on methods of precision photo-lithography with photo-printing through flexible photomasks and chemical etching of metal and dielectric layers [3].

4.3.2 Features of micro-cable design

Each assembled analog micro-cable has following zones (areas), see figure 4.3.2.
– work zone;
– technological zone;
– zone of electrical control;
– test elements for ultrasonic bonding regimes investigations.

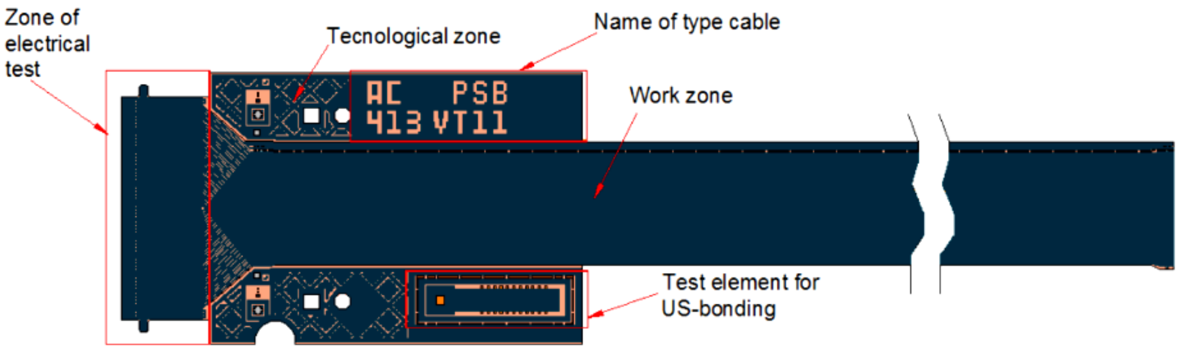

Fig. 4.3.2: Sketch of assembled analog micro-cable.

Some details about the micro-cable parameters are given below:
– number of signal traces - 64;
– width of trace in long work area - 30 um;
– pitch of trace of long work area - 112 um;
– width of trace in bond area - 45 um;
– pitch of trace in bond area - 116 um;
– width of windows of bond area - 165 um.
A photo of a typical analog micro-cable together with its components and its technological zone on the left is depicted on the photo shown in figure 4.3.3.

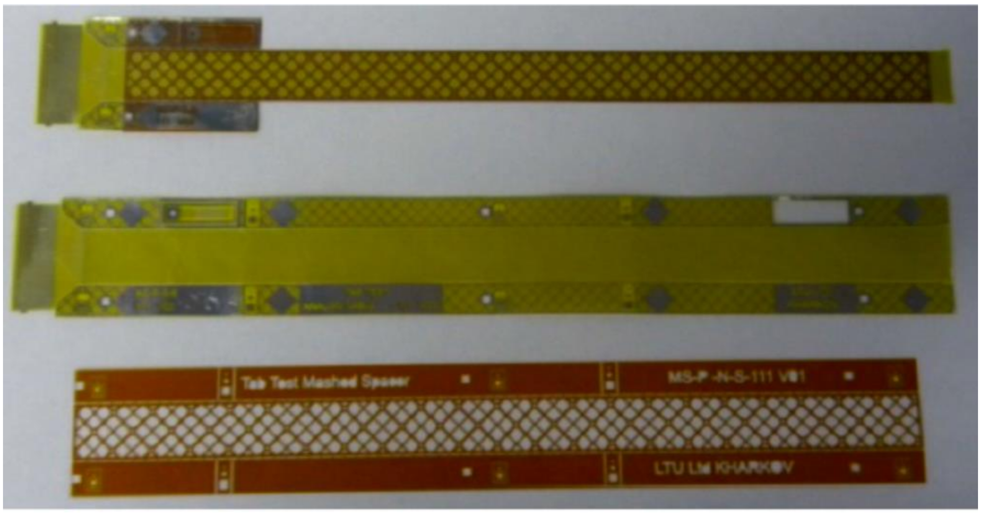

Fig. 4.3.3: Typical analog micro-cable.

4.3.3 Features of assembly

The mechanical and electrical connection to both sides of thin double-side sensors must be executed. The opportunity of formation of reach-through "windows" in polyimide layers will allow to refuse application of an aluminum wire for connection of sensor contact pad and leads of aluminum-polyimide micro-cables and to carry out connection of leads directly to sensor contact pads by ultrasonic bonding (SpTAB) through "windows" in polyimide as shown in figure 4.3.4 [4]. It will allow reducing quantity of bonded connections in detector modules practically twice and will allow considerably simplifying assembly process. Thus during assembly the opportunity of short circuits is completely excluded in the bonding area of sensor contact pads with leads of flexible micro-cables.

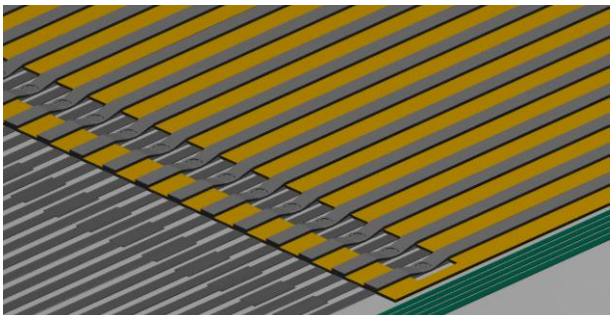

Fig. 4.3.4: SpTAB bonding of micro-cable to sensor

The assembly technology of flexible aluminum-polyimide micro-cables with sensor easily adapts for the existing automatic bonders for ultrasonic bonding. The use of identical materials (aluminum sensor contact pads and bonded aluminum micro-cable leads) ensures high quality and reliability of bonded connections.

4.3.4 Evaluation and optimization

For the full functionality of the micro-strip detector modules, the total capacitance of sensor and micro-cable at the input of the front-end electronics must be as low as possible in order to achieve a sufficiently large signal-to-noise ratio of the measurements.

If we assume that the capacitance is directly proportional to the length of micro-cable three parameters are left to optimize:

– the relative permittivity ε depends upon the material;

– the distance between two signal layers of metal traces or the shielding layer of the micro-cable;

– the width of the metal traces.

Variation of the spacer material and thickness give possibilities to influence the capacity of the cable. There were 6 material options to investigate (see Table 4.4.1).

Table 4.3.1

Material	Thickness [um]	Relative permittivity ε
polyimide 5/10 filled	50	2,25
polyimide 5/10 filled	100	2,25
polyimide 3/10 filled	50	1,8
polyimide 3/10 filled	75	1,8
polyimide 3/10 filled	100	1,8
Foamtak II	165	1,5

Possible stack-ups were chosen as listed in Table 4.3.2. In the following table one half of the symmetric stack-ups are described (from the outer layer to the plane of symmetry where the sensor is located).

Table 4.3.2:

No.	Spacer for Shielding layer	Spacer for Signal layers*
1	100 um polyimide 5/10 filled	50 um polyimide 5/10 filled
2	100 um polyimide 3/10 filled	50 um polyimide 3/10 filled
3	165 um Foamtak II	50 um polyimide 5/10 filled
4	165 um Foamtak II	50 um polyimide 3/10 filled
5	165 um Foamtak II	75 um polyimide 3/10 filled
6	165 um Foamtak II	100 um polyimide 3/10 filled
7	165 um Foamtak II	165 um Foamtak II

Note: *the spacer under each signal layer should be the same to make the laboratory assembly procedures easier.

These 7 stack-ups were simulated for a trace width of 46 um. The results for the inner and outer signal layer were calculated and shown in Table 4.3.3 [5].

Table 4.3.3

No.	Inner layer [pF/cm]	Outer layer [pF/cm]	Thickness [um]
1	0,715	0,724	544
2	0,615	0,620	544
3	0,715	0,613	674
4	0,615	0,566	674
5	0,569	0,534	774
6	0,548	0,518	874
7	0,468	0,476	1134

Stack No. 1 and 2 differ only by the polyimide material for the spacer used. No. 2 uses the polyimide 3/10 filled mesh with a mean ε of 1,8 instead of 2,25. An improvement of the trace capacitance for both layers is observable. No. 3 and 4 have the same structure as No. 1 and 2 between the signal layers, but the spacer between shielding and outer signal layer is thicker and with lower ε. This has mainly an influence on the capacitance of the outer signal layer, not on the inner signal layer. If the capacitance of both layers is to be improved the structure between the signal layers also needs improvement. No. 5 and 6 has the same stack of materials as No. 4, but the thickness of the polyimide 3/10 filled spacer is increased to 75 and 100 um. The capacitance consequently decreases with the increasing thickness of the spacer as anticipated. No. 7 contains only 165 um thick Foamtak II spacers. The low ε and the high thickness of the material results in a low capacitance of the signal layers.

Due to mechanical space restrictions in the BM@N STS detector the "best" micro-cable stack-up is not the one with the lowest capacitance, but the one with the lowest capacitance fitting in the foreseen space and manufacturability. Therefore, the stack No. 5 was chosen.

To reach the design goal of a capacitance of less than 0,5 pF/cm, the last parameter must be modified: the width of the metal traces of the signal micro-cable. The design rule requires an aspect ratio (aspect ratio = trace width / trace height) that should be at least two. Hence the trace width cannot be reduced to any arbitrary value. Thus, the width of the traces for aluminum foil with a thickness of 15 um can be achieved in the working area about 30 um instead of 45 um in the bond area.

The trace width is reduced to a width of 30 um and the calculation for the stack No. 5 is done [5]. The following values are obtained for 30 um traces: for inner layer 0,387 pF/cm; for outer layer 0,377 pF/cm.

References

[1] Pre-series production of microcables for STS detector modules at LTU Ltd / V. M. Borshchov, Yu. A. Murin, C. J. Schmidt, M. A. Protsenko, I. T. Tymchuk, J. M. Heuser, R. A. Kushniruk, M. S. Tykhomirova, K. M. Liholitova, and L. V. Klimova // GSI Scientific Report 2015, MU-NQM-CBM-1. – GSI Darmstadt, Germany. – 2016. – P. 1.

[2] Development of thin multi-line cables for the STS micro-strip detector modules / V. N. Borshchov, O. M. Listratenko, M. A. Protsenko, I. T. Tymchuk // CBM Progress Report 2007. – GSI Darmstadt, Germany. – 2008 – P. 34-35.

[3] Improvement of ultra-light microcables production at LTU for the CBM Silicon Tracking System / V. M. Borshchov, I. T. Tymchuk, C. J. Schmidt, V. G. Kucherenko, G. I. Nikitskiy, J. M. Heuser, M. A. Protsenko, J. Eschke, R. A. Kushniruk, L. V. Klimova and K. M. Liholitova // GSI Scientific Report 2014, MU-NQM-CBM-46. – GSI Darmstadt, Germany. – 2015. – P. 83.

[4] Assembly of demonstrators for laboratory and in-beam tests at JINR LHEP / A. Sheremetev, T. Semchukova, T. Andreeva, M. Protsenko, I. Tymchuk, A. Zavalniuk // CBM Progress Report 2016. – GSI Darmstadt, Germany. – 2017 – P. 49.

[5] Capacitance studies of the CBM STS microcable stack-up / D. Soyk, H. Faber, C. J. Schmidt // CBM Progress Report 2016. – GSI Darmstadt, Germany. – 2017 – P. 44-45.

4.4 The DAQ System

The BM@N STS will conceptually inherit the DAQ system from the CBM silicon tracker currently in development for FAIR. This is an entirely data driven acquisition system relying on purely self-triggering readout channels, which will also be adopted for the operation with BM@N trigger. The DAQ chain will in the following be described from front end to the first computing node.

4.4.1 The Detector Pre-Amplifier Front End based upon STS-XYTER ASIC

The CBM-STS inheritance for BM@N is most prominently visible through the employment of the CBM-STS front-end readout chip STS-XYTER. This chip implements a set of 128 parallel analogue readout channels that are equipped with a programmable fast shaper and discriminator path together with a second, slow shaper, high resolution analogue shaper channel followed by a 5 bit flash ADC. Fast path of the channel is used to provide a time stamp, while a slow one provides amplitude measurements.

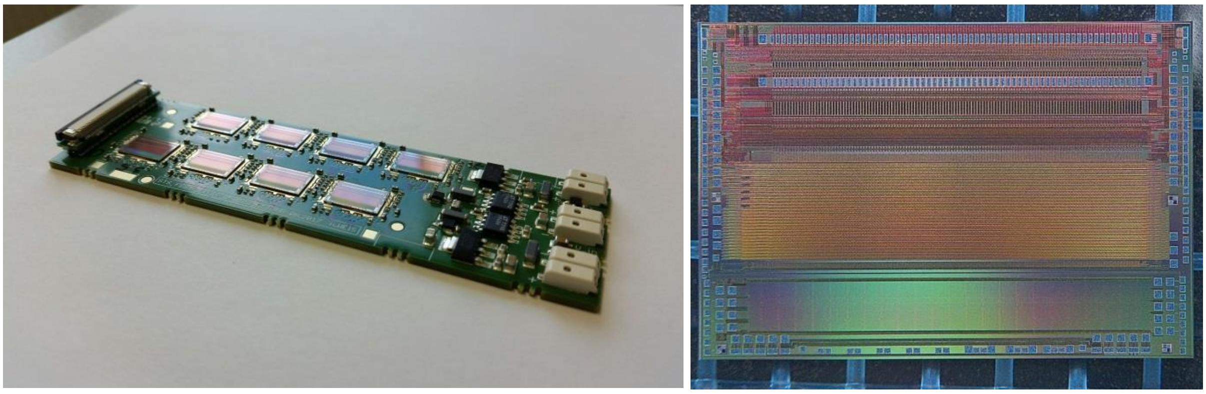

Fig .4.4.1: Bare die of the STS-XYTER Version 2.1 (right). Eight such chips will be integrated onto one readout board FEB-8 (left). The precise size of this board is depicted in detail below. A FEB-8 as depicted on the left will not be assembled to this stage as only STS-XYTERs already connected by micro cables to the sensor will be allocated on the board. Visible are power inputs on the right of the board and data signal input and outputs on the left.

Each STS-XYTER is capable of delivering data of up to 50 MHits. The FEB-8 to be employed for BM@N will have connectivity for 10 MHits per chip, giving an overall connectivity for a detector module of 80 MHits per second. The front end board may be operated at lower clock speeds down to 40 MHz. In such a mode of operation the maximum hit rate for a module is then 20 MHits per second.

The readout protocol and the detailed description of operation of the STS-XYTER is described in the STS-XYTER manual. The FEB-8 will be equipped with skimming regulators which need to be radiation tolerant for CBM and have been dedicatedly developed for this application to account for the limited physical space available for the

FEB-8. During the course of the development activities, however, it was found that also the device LT3045, a configurable regulator for up to 500mA is sufficiently radiation tolerant up to 10 kGy TID.

FEB-8 needs to be realized in two different symmetries for the P and N sides of the sensor as depicted in Fig. 4.4.2

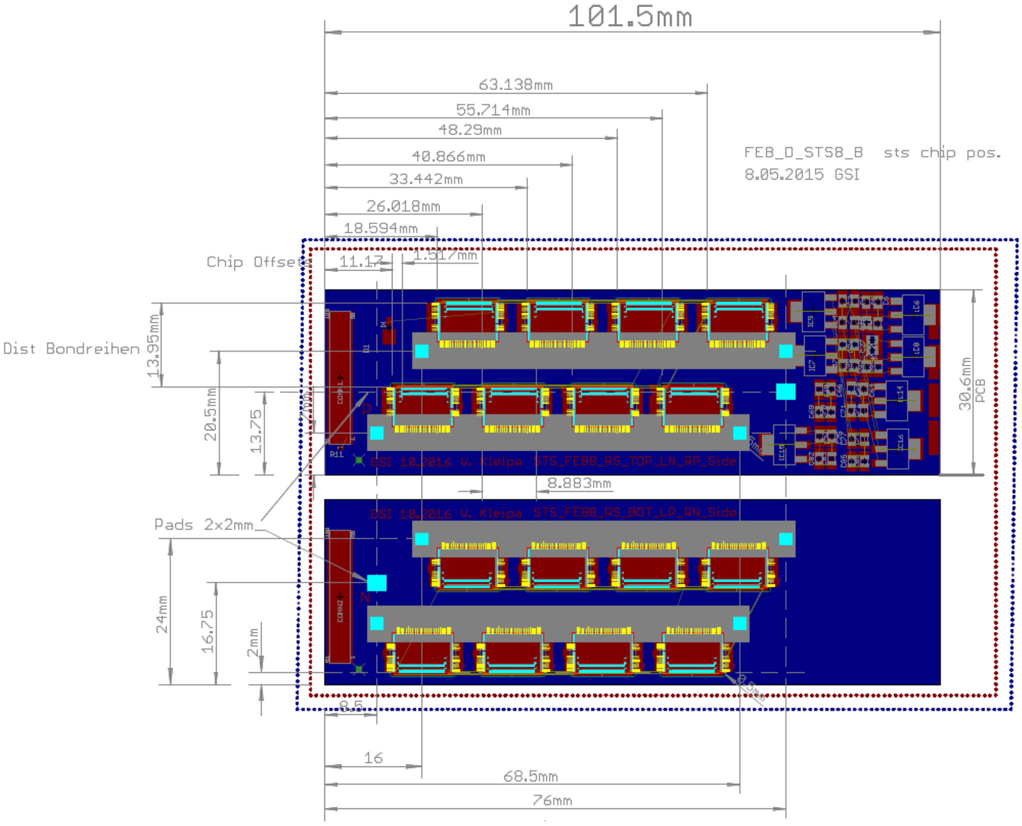

Fig. 4.4.2: *Geometric size of the FEB-8 front end boards. They need to be realized in two different symmetry versions to allow for a minimized set of different module cable sets. On the upper version the micro-cables connecting to the sensor are routed upwards, on the lower version downwards.*

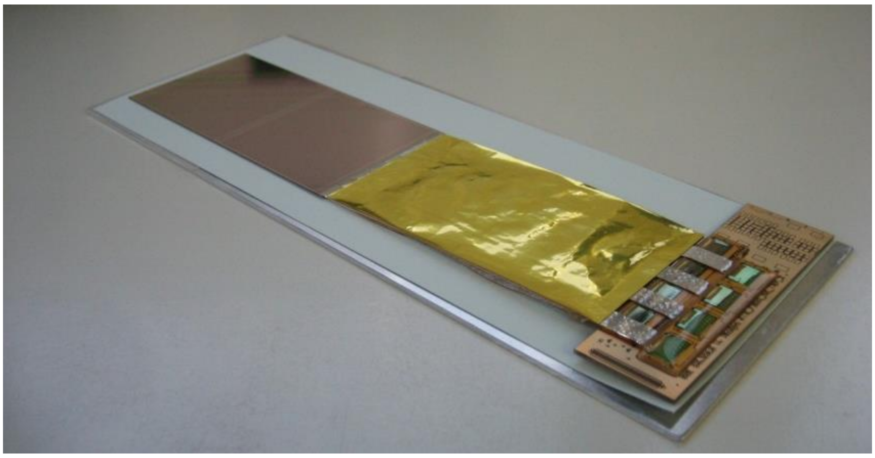

Fig. 4.4.3: *Full Silicon strip detector module with FEB-8 connected to the sensor.*

Fig. 4.4.4: *Full sensor module equipped without a shielding layer to show micro-cable routing.*

The chip communicates to the system through a programmable multi-channel e-link interface (c.f. GBTx chipset at CERN) that supplies one to five data uplinks and receives commands through one e-link type communication downlink. Both the uplinks and the downlinks follow protocols that are carefully AC balanced so that AC coupled communication is feasible. The protocol is described in [1].

For CBM the readout chips link up to a radiation hard data aggregation chip GBTx that serves to serialize the data of 14 uplink data channels of 320 Mbit/s bandwidth onto one optical 4.8 Gbit/s link. The GBTx chip is a radiation tolerant ASIC developed by CERN. Given its radiation-hard nature it is considered a dual use item and can thus not be supplied neither to Russia nor India or China. The export to these countries has explicitly been prohibited. This is where the need for the development of a more universal solution for BM@N arises. The most cost efficient and universal solution is to emulate the needed GBTx functionality in a commercially available FPGA.

GBTx provides means for transferring data acquisition (DAQ), slow control (SC), timing & trigger control (TTC) logical data paths via a single full-duplex physical optical link (Versatile Link). In principle the GBTx serves to transfer the data of 14 e-links (wide mode) onto a 14 bit wide register at the receiving FPGA device from where it may be further processed. Even though complex data serializing, scrambling and data loss protection is done along this path, the GBTx link may be viewed as a transparent data transfer from the e-link inputs onto the 14bit wide receiving register and vice versa with the down-link channels. In this respect there is no need to insist that an emulation of the GBTx functionality would exactly realize the transfer of 14 e-links. Instead, an arbitrary data mapping along the physical availability of connections and data transfer bandwidth on a particular FPGA and its links can be envisioned.

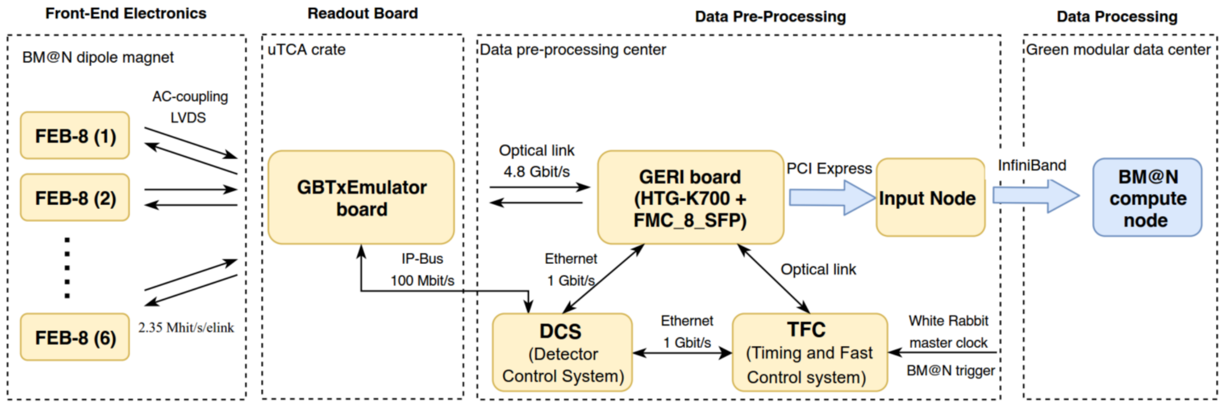

Fig. 4.4.5: *Readout chain of BM@N STS*

Compared to CBM, the BM@N STS will experience interaction rates which are lower by orders of magnitude. This is why the GBTx functionality can be emulated by an FPGA board. Also the e-link connectivity may find a better match in an emulated version. Whereas the GBTx is designed to transfer the data of 14 e-links operating at 320 Mbit/s to fill up the available optical readout payload bandwidth of 4.375 Gbit/s, the emulator provides 48 uplink connections operating at 80 Mbit/s. 56 such e-link connections would in principle be feasible but do not match the actual needs, whereas 48 e-links can serve for 6 x 8 uplinks and consequently 6 FEB-8 readout boards or the readout of 3 full sensors. Since the DAQ system of other detector subsystems of BM@N experiment are not data driven and operates with a trigger, there will be a possibility to integrate high speed ring buffers on the level of GBTxEMU board to minimize the data flow from STS front-end electronics and to link events based on trigger number. Nevertheless, the STS DAQ system will also have an opportunity to operate in a data driven mode, in this case the time stamp will be used to tie events from different subsystems.

For data readout into a computing farm, a PCIe Interface is needed that receives the optical signals from various GBTxEmulator boards and dumps the data into DMA. This functionality will herein be named GERI (General Emulator Readout Interface). In principle some processing may be realized on this FPGA level as well. For example, the data could be sorted timewise into Microslices. Naturally only data directly linked to the corresponding GERI may be considered synchronous and sorted. For the synchronization of multiple GBTxEMU interfaces additional FPGA board will be used. Proposed hardware solution for this TFC board is AMC FMC Kintex 7 board (AFCK)

We intend to send 7 Gbit optical data links from 7 GBTxEmu Boards into one GERI board. The eighth optical channel will be used for the clock and sync input from the timing control tree. The feasibility of this timing and synch path depends upon the detailed connectivity within the GERI board. Only if the clock of the particular timing SFP can be recovered and jitter cleaned on the board, it can be used for synchronization of the entire system.

A GERI board consequently receives up to 7 x 3,75 Gbit/s = 26,25 Gbit/s = 3,28 GByte/s which it needs to transfer via PCIe into the compute node. With PCIe Gen 2, one can transfer 0,5 GByte/s per lane. Consequently an 8 lane PCIe Gen 2 or higher board is needed to for the GERI functionality. Various options are commercially available:

1. The Hightech Global HTG-K700 is such a board that can mount an 8 SFP FMC on the input side and provides 8 lane PCIe Gen 2.

2. The other alternative could be the Trenz Electronic TEC0330[3] Virtex-7 PCIe FMC Carrier which also has 8 lane PCIe Gen 2. It additionally provides complex clocking resources with an external clocking input via SMA and a LMK04828B chip for clocking and jitter cleaning that would ease synchronous operation.

3. Solution, which will be used in CBM, but most likely is redundant for BM@N STS. The High Flex board (see attached short documentation) is a board that has been developed by KIT in Karlsruhe. It provides 2 8lane PCIe Gen 3 Interfaces with a total bandwidth of 119 Gbit/s.

4.4.2 The GBTx-emulating boards GBTxEMU-3Sens-1, GBTxEMU-3Sens-2

The function of the GBTxEMU-3Sens-1 device is to interface the STS-XYTER based front-end boards FEB-8 to an FPGA-Board (e.g. HTG-K700) as interface into the computer node. The FEB-8 for the silicon sensor readout may be replaced by corresponding front-end boards with different e-link configurations for other detector systems such as e.g. the CBM-MUCH. This FPGA-board could be named GERI as GBT-Emulator Readout Interface. The GBTxEMU-3Sens-1 is a GBT emulator that can be used to read out 3 CBM STS sensors and channel the data onto one multi-gigabit optical link, while the GBTxEMU-3Sens-2 can employ up to two optical multi-gigabit links. The GERI board incorporates the data processing functions that were previously for the CBM-STS handled by the DPB-board, which in this concept is obsolete. It emulates the GBT in that it serializes the 6x8 = 48 uplink-e-links onto a 6 Gbps link to the GERI and deserializes an optical downlink to 6 downlink-e-links together with a recovered clock. The e-links are to be operated at 40Mhz or alternatively at 80MHz, resulting in an up-link DDR data rate from the STS-XYTERs of 80MHz and 160MHz respectively. This way the GBTxEMU board can serve to operate and read out 6 FEB-8 front-end boards with 8 STS-XYTER client chips each, one down-link and one clock line.

---

[3] https://wiki.trenz-electronic.de/display/PD/TEC0330+TRM

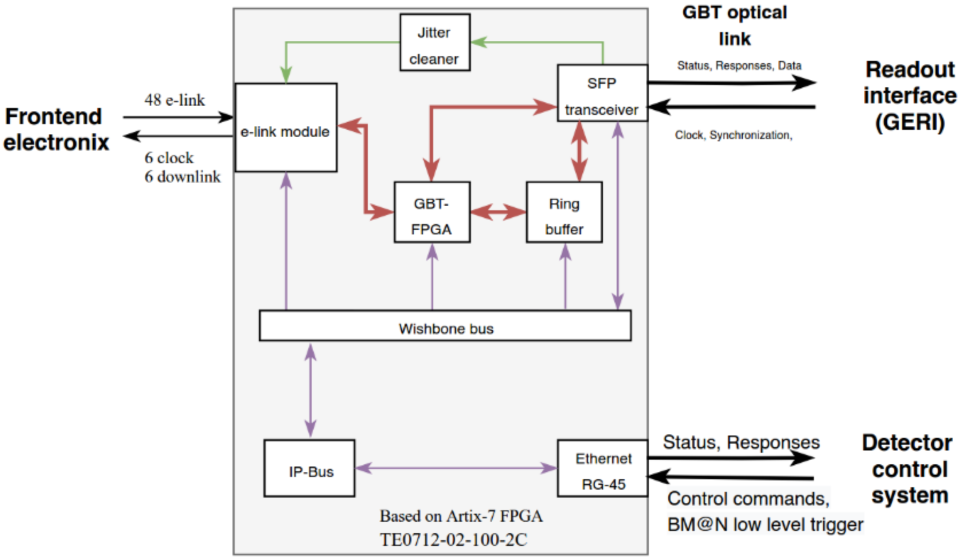

Fig. 4.4.6: Block diagram of the GBTx Emulator firmware.

The GBTxEMU board can be equipped with one or alternatively two 6 Gbit optical links, supplying each a maximum payload bandwidth of at least 4.375 Gbps.

The GBTxEMU has a 100MHz Ethernet Phy on board which can be employed for configuration via a modified IP-bus, connectivity through RJ45.

Interface to a FEB-8:

1. The interface to a FEB-8 consists of a down-link and a clock together with 8 or 16 up-links, each LVDS.
2. Whether 8 or 16 up-links from one FEB-8 are to be addressed is configurable.
3. A maximum of 48 up-link e-links, 6 down-link e-links and 6 clk links are physically available.
4. No automated phase adjustment between down-link and clock to the front-end chips is needed as the operating frequency is comparatively low. Identical signal transit time from GBTxEMU to the STS-XYTER chips may be assumed (Δt<10ps), so set-up and hold times between clk and down-link are to be pre-adjusted and fixed through firmware.
5. The up-links have fixed routing delays of up to 6ns among each other from one FEB.
6. Up-links from different FEBs may have arbitrary routing delays with respect to other FEBs.
7. One emulated down-link should serve to configure the GBTxEMU board itself as an alternative access to the IP-bus access (slow control of GBTxEMU). So six downlinks channeled through the Gbit optical link to the GBTxEMU board are routed to the six FEB-8 front end boards, whereas one downlink simply ends within the GBTxEMU for local configuration.
8. Timing and trigger as well as slow control commands are transferred through the emulator to the GBTxEMU board as well as to the client FEBs.

Clock recovery:

The GBTxEMU board needs to recover the global clock from the optical interface so that it may synchronize to a globally distributed clock. To this end it is equipped with a Si5338 clocking chip as well as with a Si5344A jitter cleaning and clocking device.

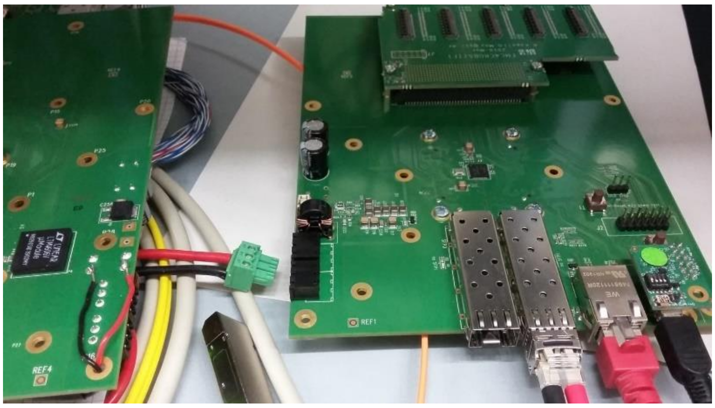

Fig. 4.4.7: *Test bench with GBTxEMU*

The whole GBT protocol is designed as an exchange 120 bit frames at f_LHC (40 MHz for practical purposes). So 120 * 40 Mbps -> 4.8 Gbps.

The frame rate (40MHz) will remain the base frequency, and everything is designed around this. The frame length is deep into the GBT cores, e.g. the FEC encoders for the downlinks. One can go to twice the speed, as done in the GBT successor ASIC, and still have a consistent scheme, but not easily from 4.8 to 6.

Consequently, in the scheme described above 6 x 8 = 48 uplinks at 80 Mbps from the six FEB-8 front end boards will fill up 96 x 40 Mbps = 3.84 Gbps of the available bandwidth in one link. In principle two FEB-8 out of the six or equivalently one sensor module could be operated at 80 MHz or 160 Mbps per e-link rather than 40 MHz. This would fill 112 out of the available total of 120 channels.

Signal latency is not important for the data uplinks, whereas deterministic latency is essential in the downlinks for link and system synchronization.

Should it turn out that this is an issue for the Xilinx Artix device, one may be forced to employ Kintex devices on the GBTxEMU boards instead.

STS front end ASICs are not supposed to support triggered mode of operation. Thus, to have a possibility to switch from data driven to a trigger data acquisition mode ring buffers should be used. The most suitable place for them is GBTxEMU board. The size and operation speed of those buffers should be enough for the BM@N trigger signal latency.

4.4.3 The GERI-Computer Input node (Gbtx Emulator Readout Interface)

The optical links of the GBTxEMU boards need to connect to an adequate optical interface as input node to the computing system. The board that has this function has been named GERI for Gbtx Emulator Readout Interface.

The GERI implements the backends of the optical interfaces to multiple readout boards. This includes adaptations of the GBT-FPGA core which handles the communication with the GBTxEMU devices as well as the backend of the ASIC communication protocol. Preprocessing of the hit data stream includes address expansion, time alignment of data from multiple sources and building of micro slices, which are data containers for all hit data created in a given time interval. The GERI implements the interface to the detector control system (DCS) connected to the backend of the communication protocol for the frontend ASICs. The GERI also implements the interface to the Timing and Fast Control System (TFC), which merges synchronization commands and fast control commands such as Start/Stop of acquisition or throttling commands coming from the TFC master into the local downlink streams.

The most probable candidate for GERI platform is an 8 lane PCIe Gen2 interface board that is commercially available at Trenz[4] TEC0330-4.

Fig. 4.4.8: *TRENZ TEC0330-4 PCIe Gen2 Interface Board as best candidate for the physical interface to the computing node.*

This board has the intriguing advantage that is provides a dedicated clock input that may be used to synchronize its operation to a global master clock. Otherwise the detailed functionality that needs to be provided in the Virtex. Feasibility of this option is currently being studied. The interfacing firmware towards GBTxEMU as well as towards the computing node (DMA) may be reused from CBM CRI developments.

As a server solution decided to use the ASUS ESC8000 G3 Server. It can take up to 8x GERI boards.

---

[4] www.trenz-electronic.de

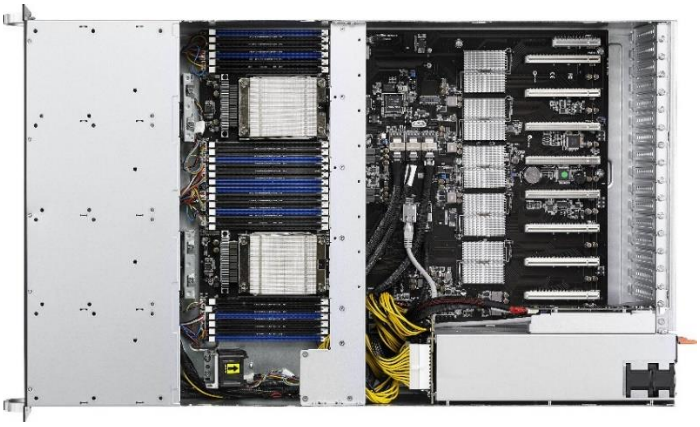

Fig. 4.4.9: *ASUS ESC8000 G3 Server*

4.4.4 The Timing and Fast Control system

The Timing and Fast Control system (TFC) is the key element to manage the free-streaming, self-triggered, high rate data acquisition system of CBM experiment. TFC for BM@N STS will be based on the same solution adopted for BM@N DAQ structure.

The TFC synchronizes all GBTx Emulator Readout Interface cards (GERI). It avoids uncontrolled data loss on readout links with finite bandwidth. It is supposed to ensure to record good full events from all active detector subsystems.

The prototype of TFC is based on the following platform: AMC FMC Carrier Kintex7 board (AFCK).

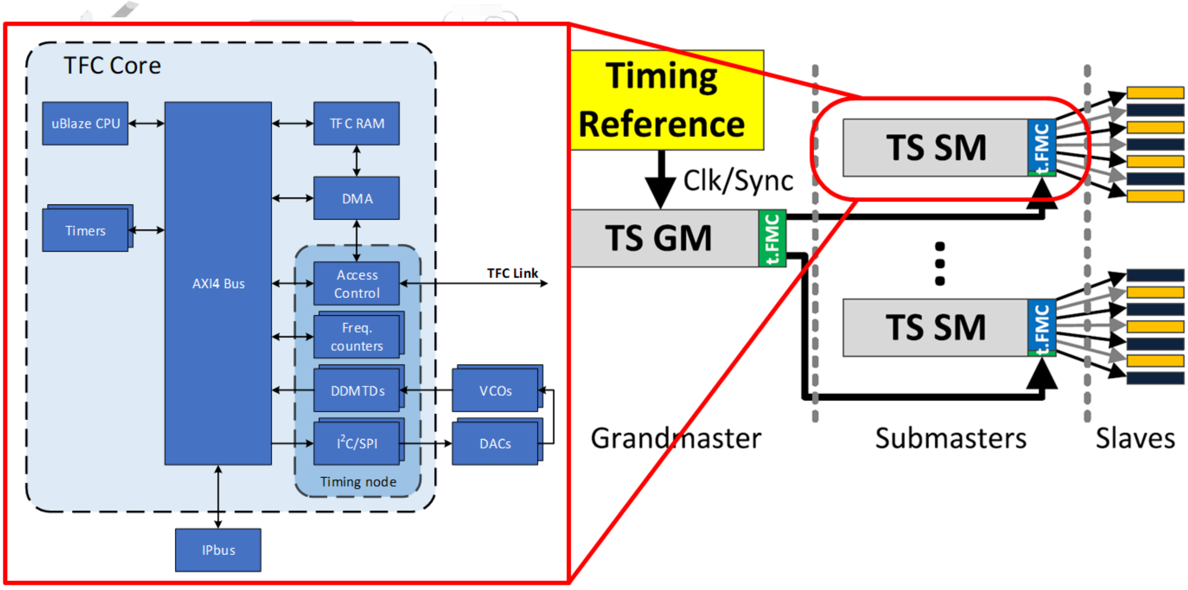

Fig. 4.4.10: *CBM TFC core architecture.*

The TFC system of BM@N STS will receive an external White Rabbit master clock[5] (125MHz), necessary for synchronization with other detector subsystems of the BM@N

---

[5] http://www.ohwr.org/projects/white-rabbit.

experiment. It will have a clock divider to provide jitter-cleaned 40 MHz clock for GERI boards. Also, it should provide BM@N trigger signal for the GBTxEMU devices while operating in triggering mode.

4.4.5 Integration of the STS readout chain into BM@N DAQ system

The readout chain of BM@N STS project is based on data-driven concept of CBM experiment. Thus, merging of the data driven STS and triggered mode BM@N data streams is one of the main issues. Since all subsystems of BM@N experiment are synchronized via White Rabbit, time stamp can be used to link events from different streams. However, for the online data processing of the data driven readout a computing power and large storage capability is needed. To get around this the ability to operate in triggered mode will be implemented in BM@N STS readout. Additional ring buffers on the level of GBTxEMU devices will be used to store data for the time of BM@N trigger latency. The BM@N trigger distribution through the STS readout tree will be made on the base of the TFC system, which will have additional core for the handling of BM@N trigger signal.

References

[1] K. Kasinski, R. Szczygiel, W. Zabolotny, J. Lehnert, C. Schmidt, W. Müller, W.F.J.. (2016). A Protocol for Hit & Control Synchronous Transfer for the Front-End Electronics at the CBM Experiment. Nuclear Instruments and Methods in Physics Research Section A: Accelerators, Spectrometers, Detectors and Associated Equipment. 835. 10.1016/j.nima.2016.08.005.

4.5 Cooling system

The cooling of BM@N STS consists of two different cooling systems: a liquid cooling system to remove the power dissipated by the front-end readout electronics (~15 kW) and a gas cooling system to remove the moderate heat produced by the sensors (~6mW/cm^2) and to compensate temperature gradient inside the STS box.

4.5.1 Cooling concept

Heat dissipated by the front-end electronics of the STS system is estimated to be on the level of 15 kW. This heat should be removed from the system to avoid thermal runaway. The readout electronics is placed outside of the geometrical acceptance of the detector that is why massive heat exchangers with a liquid cooling are used. To remove this power and to cool the electronics we have opted for a water cooling system. Full STS setup will be operated inside thermal insulation box. The temperature of the box should be kept at the level below 20° C during the time of the operation. To minimize the temperature gradient inside STS box and to remove the power dissipated by the sensors themselves additional gas cooling system is implemented.

4.5.2 Liquid cooling system

4.5.2.1 Chillers

The liquid cooling system is based on two K12 ATC chillers[6], which provide 10 kW cooling capacitance at the cooling liquid temperature of 5°C (Figure 4.5.1.). This chiller was chosen due to its high cooling capacitance and compact size. One chiller is used to cool readout electronics of all C-frames located from the same side from the beam pipe. Chillers will be located at the distance of ~25 m from the STS box inside the BM@N cave. For the safety reason all components of the system should withstand pressure up to 15 bars. Number of the connectors is minimized and all of them are located outside of the STS box. The needed liquid flow is estimated to be on the level of ~30 l/min for a chiller.

---

[6] Applied Thermal Control (https://www.app-therm.com)

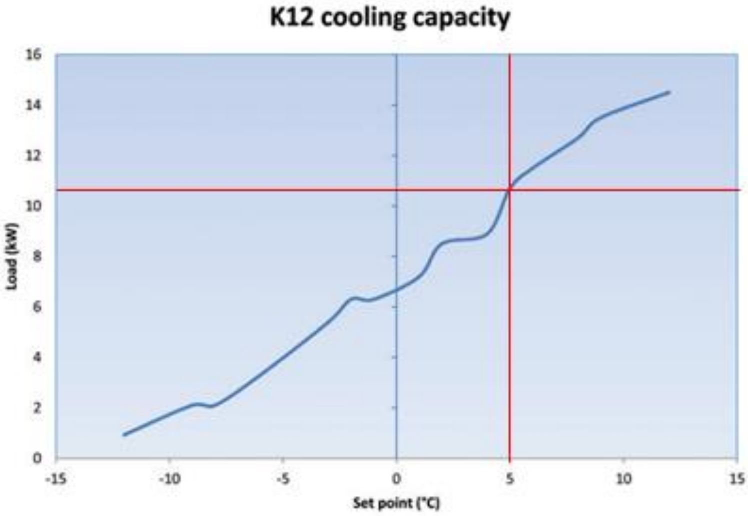

Fig. 4.5.1: Cooling capacitance of a one ATC K12 chiller. (source: ATC) For the cooling of front-end electronics two chillers are used. The operation temperature is 5°C.

4.5.2.2 Heat exchanger plates

Due to the safety requirements the heat sink requires high reliability for the whole operation period. A design with aluminum pipe glued into an aluminum plate appears feasible as discussed below. A photograph of such plate manufactured by Artmash in accordance with our specification is shown in figure 4.5.2.

Fig. 4.5.2: Prototype of the heat exchanger for the 1st Station. Aluminum pipe with a diameter of 8 mm is glued into grooves in the aluminum plate.

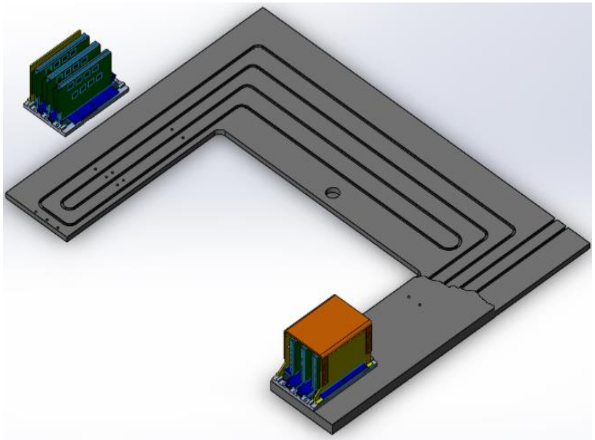

Fig. 4.5.3: Schematic view of the thermal path from the heat producing ASICs mounted onto a FEB. 6 FEBs are mounted into one FEB box which serves as thermal connector to a heat exchanger plate

4.5.2.3 FEBs

The main heat producing elements are FEBs which carry readout ASICs and LDOs. ASICs are installed on the PCB with ~50μ of thermal and electrically conductive glue (~2.5 W/m·K). Thermal contact between the ASIC and fins is realized with an array of thermal vias increasing the thermal conductivity of pure FR4 from 0.2 W/m·K to ~50 W/m·K. Each FEB is glued to the aluminum fin of L-shape (see figure. 4.5.4).

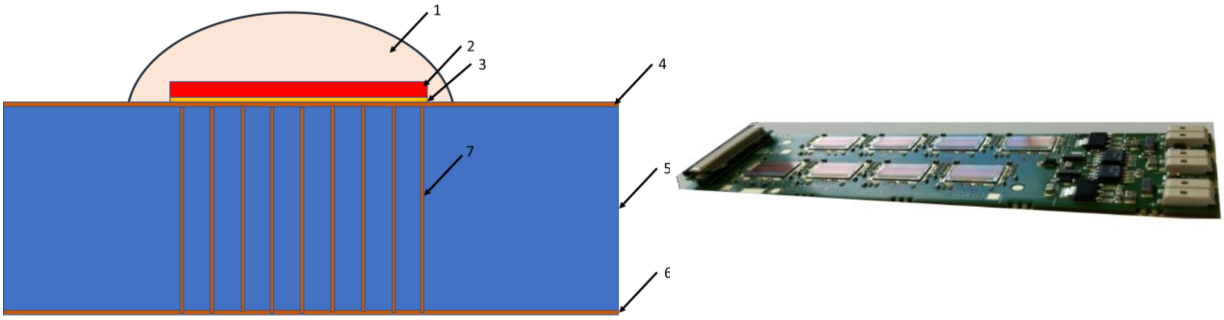

Fig. 4.5.4 Left: Schematic drawing of the thermal contact between ASICs on the PCB and fin; 1 – Encapsulation glue (thickness ~2 mm); 2 – ASIC (thickness 200 μ); 3 – Glue EPOTEC 4110 (thickness 50 μ); 4,6 – Gnd metallization layer (35 μ Cu); 5 – PCB 1,65 mm thickness (FR4 material); 7 - plugged thermal vias – Cu. Right: *Photograph of the FEB with 8 ASICs.*

4.5.2.4 FEB Box

The power dissipated from the FEBs is removed by placing them on an aluminum multi-fin cooling block (thereafter referred as the “FEB Box”) which is placed onto the heat exchanger plates (figure 4.5.3). It has been optimized with respect to size (as small as possible) and thermal conductivity (as high as possible). Several FEB boxes with various width of the cooling fins have been built, tested experimentally and compared with thermal simulations (see figure 4.5.5). To minimize thermal resistance an additional attempt was made to produce CF fins. Sandwich made of special CF[7] prepreg (800 W/m·K along the fiber) and graphene sheets[8] (1500 W/m·K) was tested. The maximum achieved thermal conductivity of the sample is 255 W/m·K. However, simulations and experiment have demonstrated that due to the low thermal conductivity of the sample in the perpendicular direction to the fiber (~15 W/m·K) usage of composite is questionable due its high costs.

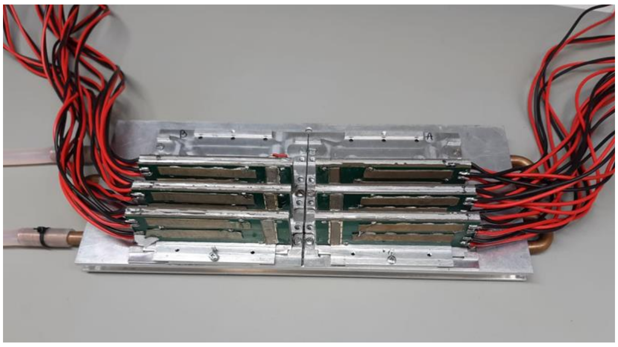

Fig. 4.5.5: Photograph of two FEB Boxes loaded with dummy FEBs. The FEB boxes are mounted on the heat exchanger.

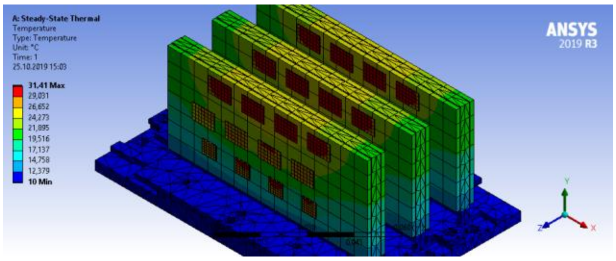

Fig. 4.5.6: Thermal simulations results for the 2 mm thick cooling fins and a coolant temperature 10 °C

---

[7] Mitsubishi K13D2U

[8] FGS003 Amec Thermasol

The results obtained from simulations are shown in table 4.2.1, and illustrated in figure 4.5.6, which depicts the simulated map of temperature gradients for a 2 mm thick aluminum fin.

	1 mm	2 mm	2,5 mm	3 mm
Upper ASICs	38,9	28,9	26,8	23
Bottom ASICs	29,5	26,9	24,4	20,7
LDO	30,7	27,6	26,2	17

Table 4.5.1: The maximum temperature of the ASICs on the FEB simulated for different thicknesses of the cooling fin. The coolant temperature is 5° C.

4.5.3 Optimization of the thermal Interfaces

The space between the two removable interfaces is usually filled with microscopic air bubbles. Therefore, it is important to fill the region of interface with some Thermal Interface Material (TIM) to increase the thermal conductivity. The most commonly available TIMs on the market for removable interfaces are thermal grease, thermally conductive pads and thermally conductive graphene films. The thermal properties of the TIM used plays essential role for the following interfaces:

Interface-1: Heat Exchanger Plate – FEB Box and

Interface-2: Front-End Board – FEB Box's fin.

The most relevant properties of the TIMs used for the interface-1 are tabulated in table 4.5.2. The thickness of the grease is assumed to be 100 μm but in reality strongly depends on the application method since the mechanical properties of different TIM vary. The TIMs were tested at the test bench by applying them between FEB boxes and heat exchanger plate. A photo of the test bench is shown in Figure 4.5.6. Temperature difference between the heat exchanger plate and the base plate of the FEB box were measured for the coolant temperature of 5 °C. Temperature was measured by thermocouple locally in several points and with IR camera scanning the global temperature profile. Results are summarized in the table 4.5.3**.** Major conclusion from the interface optimization study is that more viscous TIM (grease) fills microscopic gaps between the interfaces better than relatively more rigid types of TIM as graphene films or thermal pads. Experimentally, sensitivity to the TIM type was found to be strongest for interface-1.

	Thermal Conductivity k [W/m·K]	Thickness d [μm]	Thermal resistance $R=d/k$ [m^2·K/W]
Thermal Grease 1[9]	4,5	100	$22{,}2\cdot10^{-6}$
Thermal Grease 2[10]	10,2	100	$9{,}8\cdot10^{-6}$
Thermal Grease 3[11]	13,8	100	$7{,}2\cdot10^{-6}$
Thermal Grease 4[12]	14,3	100	$7{,}0\cdot10^{-6}$
Thermal Pad[13]	62,5	200	$3{,}2\cdot10^{-6}$
Graphite foil[14]	15	30	$2{,}0\cdot10^{-6}$

Table 4.5.2: TIM types used for the tests and their properties

Grease 1	Grease 2	Grease 3	Grease 4	Pad	Graphene
1,7	1,3	0,9	0,7	5,8	13,1

Table 4.5.3: Results of TIM optimization. ΔT between FEB box and heat exchanger plate for different TIM types is shown. Temperature of the coolant is 5°C. Room temperature and humidity were maintained at the same level during measurements.

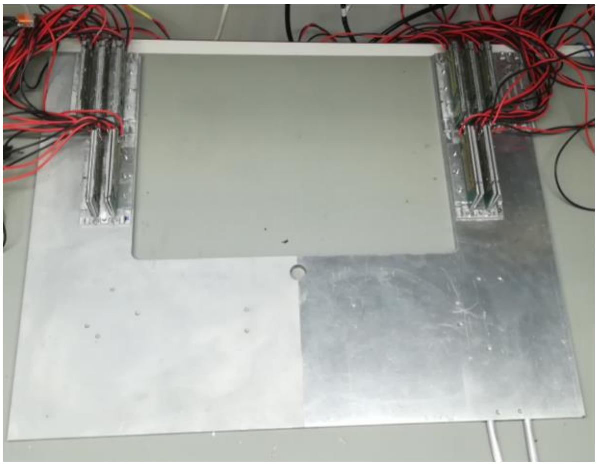

Fig. 4.5.6: Photograph of the test bench for the TIMs. One half of the heat exchanger (left) was machined by a waterjet, while the right part was polished. Thermal contacts of both parts were compared.

For the Interface-2 there is an additional requirement on the dielectric properties i.e. it should withstand up to 500 V DC. We have tested two options: a thermal conductive tape and epoxy film glues. We have finally chosen for our application a custom-developed film glue filled with diamond powder. Thickness of the glue film is 200 μm with measured thermal conductivity value of a sample ~ 3 W/m·K.

---

[9] GD900

[10] Polimetech PK-2

[11] Thermalright TF8

[12] Termal lright TF

[13] Termal grizzly Carbonaut

[14] FGS003 Amec Thermasol

4.5.4 Gas cooling

The innermost sensors, i.e., those with the highest radiation load, will eventually produce up to 6 mW/cm^2 at the end of their lifetime. To avoid premature thermal runaway this power load has to be neutralized. As we have to avoid additional material in the acceptance region, cooling via a stream of cold gas is the obvious choice. Natural convection as a cooling mechanism is excluded due to the tight assembly. Moreover, the sensors are surrounded by the FEB-boxes, which might release some residual heat into the sensor region. Those calculations were done for the CBM STS [1]. Back-of-the envelope calculations show that a flow of cold gas (v = 0.3 m/s) would cool the sensor sufficiently. The gas nozzles are located outside of the detector acceptance.

The results of the realistic cold gas flow simulations done in SolidWorks for CBM STS [1] are shown at Fig. 4.5.7. Simulations were performed with the aim to show whether the blowing air could cool the sensors around the beam pipe (~50 cm in CBM case). Results of the simulations have shown that the sensors around the beam pipe are subjected to sufficient gas flow. To minimize temperature gradient inside STS box the cooling gas has ambient temperature (20 °C).

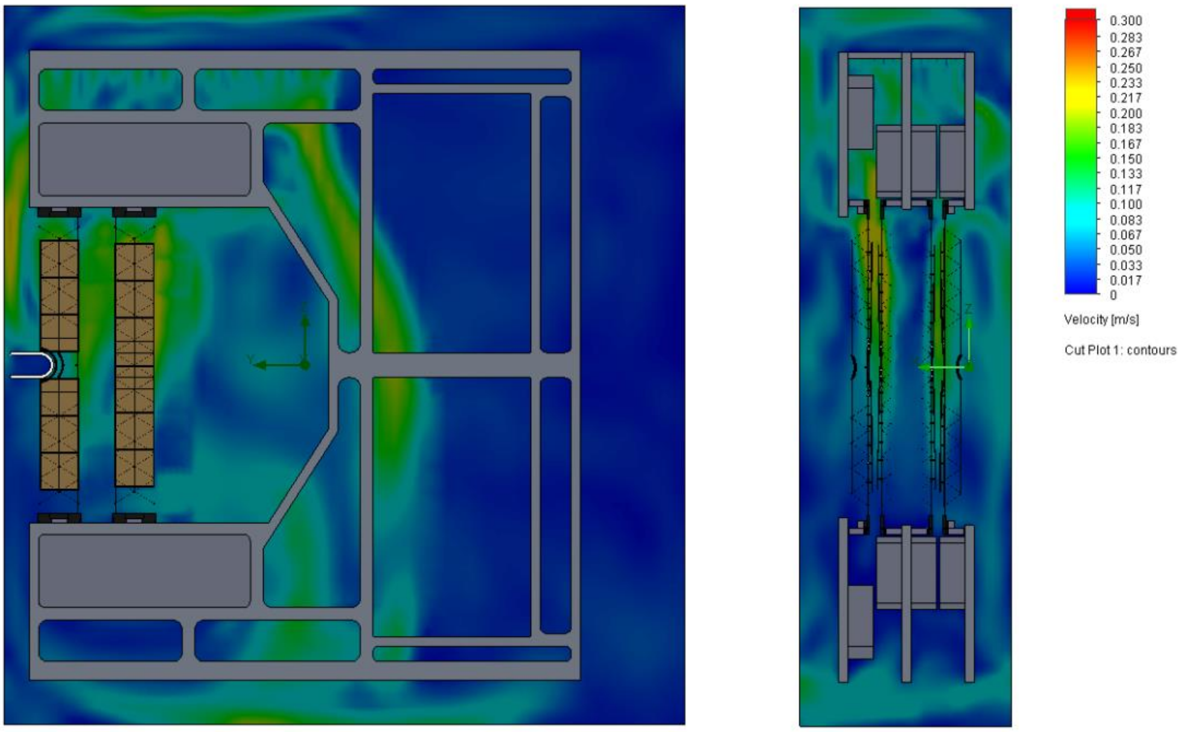

Fig. 4.5.7: Front view (left plot) and Left-Side view (right plot) representing cut plot contours of the gas flow in terms of velocity for the CBM-type STS station. It can be observed that flow successfully reaches the sensors.
(Source: CBM Technical Note 18004)

References

[1] Conceptual Design Report of the STS Cooling System , K. Agarwal , M. Kis , P. Kuhl , H. R. Schmidt , O. Vasylyev, CBM Technical Note 18004, November 24, 2018

4.6 STS Module Assembly

The basic component of the STS system is a module. Each module consists of specially developed components: double-sided micro-strip silicon sensor with 1024 strips per each side (described in Sect. 4.2), two front-end boards with readout electronics (described in Sect. 4.4) and a set of low-mass aluminum micro-cables (described in Sect. 4.3). The highly granular detector system requires a high density of electrical connections with low cross-talk. Therefore, we have opted for a Tab-bonding technology to connect the aluminum micro-cables to a sensor and to the front-end ASICs. The module assembly requires a special equipment, a clean assembly site and trained staff. Moreover, the module assembly turns out to be the most time-consuming procedure of the STS production. A procedure including a set of special jigs was developed and tested on mockups and module prototypes. The module assembly technology is described below.

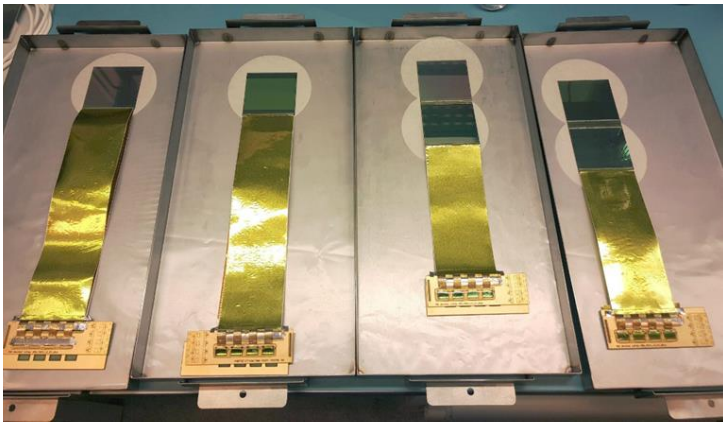

Fig. 4.6.1: Photograph of the module mockups of different size assembled at JINR

4.6.1 Components of the module

The size of the sensor and the length of the micro-cables depend on the location of the module. According to the layout of the STS as described in Sect. 4.1, 10 different types of modules have to be assembled. The full list of the components is described below.

Fig. 4.6.2: Set of the components for the module assembly: 32 micro-cables with shielding layers, two FEBs with 16 STS-XYTER ASICs, and 8 LDOs.

Sensors of three different sizes are used to assemble STS modules: 42×62 and 62×62 mm^2 sensors are used to assemble regular modules, and 42×62 mm^2 sensors with a round cut are used to assemble 16 central sensors, which are located near the beam pipe. The sensors were produced by two vendors, i.e. CIS Forschungsinstitut für Mikrosensorik GmbH in Germany, and Hamamatsu Photonics in Japan. All sensors have been tested by the vendors. However, a dedicated probe machine was developed and produced according to our specifications in order to perform on-site electrical quality assurance (QA) tests of the sensors. A photograph of this probe machine is shown in the figures 4.6.3a and 4.6.3b. Electrical QA tests include common IV and CV measurements, and strip-by-strip capacitor leakage current measurements at 10 V and 20 V followed by strip current measurements at 130 V and 150 V. Typical results of measurements are shown in the figures 4.6.4a and 4.6.4b. These measurements allow to detect shorts, broken AC capacitors, and other defects. The sensors are stored in a dry storage in a special package at the assembly site. Before assembling, a visual inspection of the sensor is performed to avoid scratches and dust particles in the bonding area. Photographs of the bonding area are stored in the production DB.

Fig. 4.6.3a: Photograph of the sensor probe machine used for the electrical QA tests of the sensors.

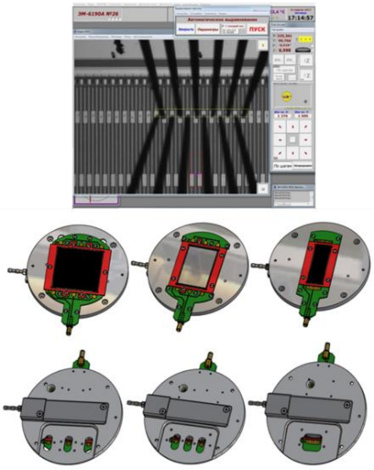

Fig. 4.6.3b: Photograph of the probe needles touching the pads on the sensor (top). Different vacuum tables for the fixation of different sensor types on the probe machine (bottom)

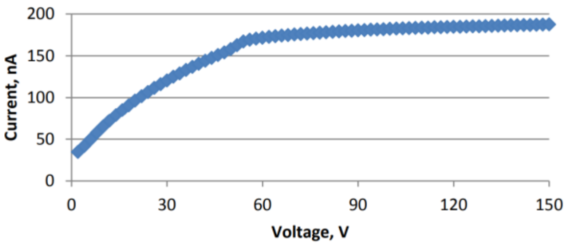

Fig. 4.6.4a: Typical common IV measurements for the sensor

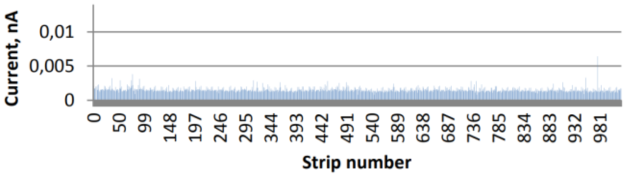

Fig. 4.6.4b: Typical capacitor leakage current measurements at 20 V bias voltage

Each double-sided silicon sensor has 1024 strips on each side with a pitch of 58 µm. The bonding pads are arranged in two staggered rows at the edges of the sensor with a pitch of 116 µm, a third and a fourth bonding row are placed behind the first two rows as an alternative for bonding and testing with a help of the probe machine. The N-side-strips are parallel to the side edges of the sensor, the P-side-strips are inclined at 7.5° with respect to the N-side-strips. Short strips in the corners are connected via the second metallization layer (see figure 4.6.5).

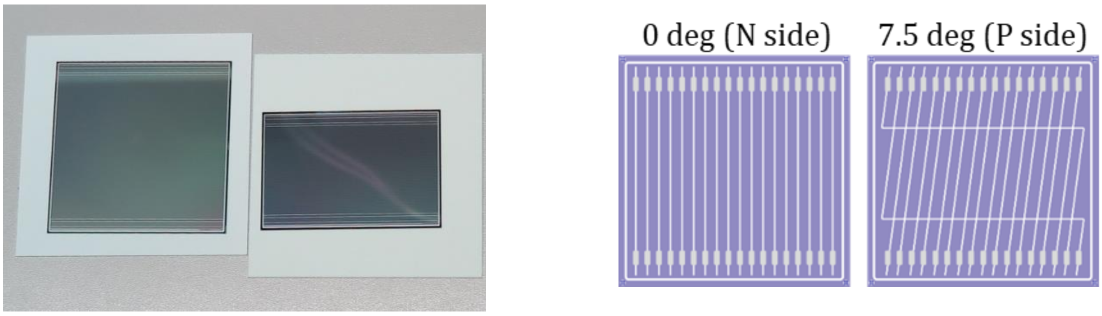

Figure 4.6.5 Photograph of the sensors (left) and the strip topology for the P- and N- sides of the sensor (right.)

Because of the small pitch, the low material budget and the electrical properties, the realization of the signal transmission via analog micro-cables is a big challenge. For the module assembly, Al-micro-cables produced by LTU ldt (Kharkiv, Ukraine: http://ltu.ua) are used. The cables consist of a 14 µm thick aluminum film covered with a 10 µm thick insulating polyimide layer. A photograph of the micro-cable is shown in figure 4.6.6.

Each micro-cable comprizes 64 aluminum traces with a width of 30 µm and a pitch of 112 µm, produced by a photolithography process and wet etching. In the TAB-bonding area, the width is 45 µm and the pitch is 116 µm. For a complete module, eight different cable types are necessary (four of each type), in total 32 micro-cables.

The sensor as well as the ASIC have two staggered bonding rows, and, therefore, a bottom and a top layer are necessary. On the FEB the ASICs are also arranged in two rows, this means two cable lengths and two cables types are necessary for P- and N-side, since the micro-cables of the N-side are bonded in the two back rows. In addition, on each side micro-cables with a Bias-line are needed.

All cables have their unique number, which is applied on the packaging and in the test zone of the cable. Since the micro-cables are very sensitive to the environment humidity level due to the polyamide layer, all cables are stored in the dry storage in the packages.

Before the assembling, micro-cables are unpackaged and kept under an antistatic fan to relieve static charge that can accumulate in a polyamide. All cables pass optical and electrical tests in LTU. However, each micro-cable is visually inspected before the assembly, i.e. the traces width uniformity and the cleanliness of the bonding area are carefully checked. Photographs of the bonding areas are stored into production DB.

Fig. 4.6.6: Al micro-cables with step test zones in the transport package

The front-end electronics of the STS is based on the STS-XYTER ASIC. Each chip has 128 channels. The inputs of the channels are arranged in two staggered bonding rows. A photograph of the ASIC is shown in figure 4.6.7. One side of the sensor is read out by 8 chips, i.e. 16 ASICs are needed for the assembly of one module. For the tests of the ASICs a pogo pin test circuit was developed. A special routine for the tests of the analog and digital parts of the ASIC, and for the calibration of the ADC and the fast discriminator is used for the chip QA certification. The final report is stored in the production DB.

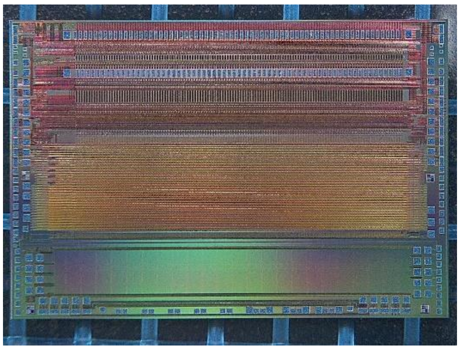

Fig. 4.6.7: Photograph of the STS-XYTER ASIC v.2.1

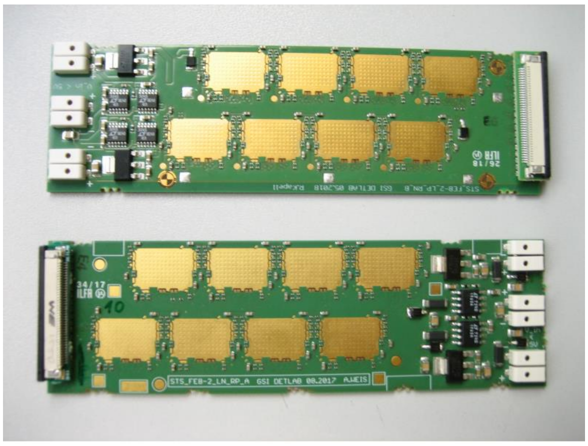

Fig. 4.6.8: Photograph of the two FEB boards for the P and N sides of the sensor

The 16 ASICs are mounted on two Front End Boards. Each FEB is used to readout one side of the sensor. A photograph of the FEBs of two different symmetries is shown in figure 4.6.8. For the AC coupling of the differential links HV capacitors are used. Due to a very limited space on the PCB those capacitors are 3d mounted under the mezzanine board with an FPC connector. Before the assembling, the bonding quality of each differential link is checked as well as the resulting value of the AC coupling capacitance. A pogo-pin test circuit for the quality assurance of the FEBs is now under design at GSI.

4.6.2 Assembly procedure

The assembly of the STS module includes several steps comprising the assembly workflow. The four main steps of the assembly are sketched in figure 4.6.9, and are described below.

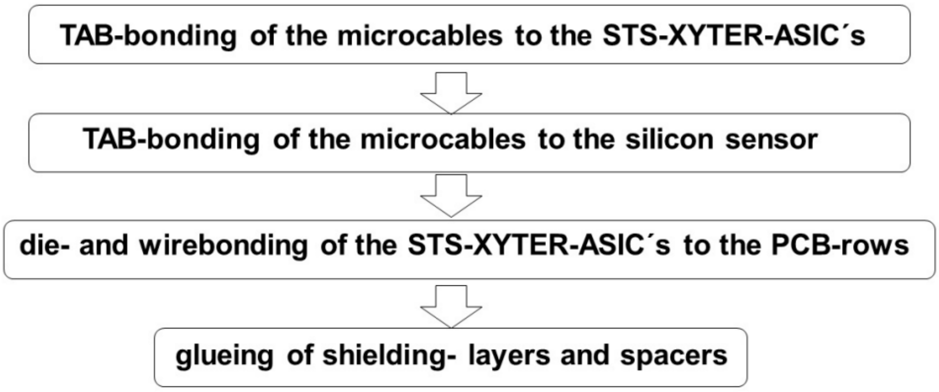

Fig. 4.6.9: Four main steps of the module assembly workflow. Those steps are performed separately for the P and N sides of the sensor.

4.6.2.1 Tab-bonding of the micro-cables to the STS-XYTER ASICs

TAB-bonding is a solid phase metal welding process using ultrasonic power and force to bond the aluminum traces to the aluminum pads of the ASIC or sensor. The tip of the TAB-bond tool is a cross groove. Figure 4.6.10 shows a row of TAB-bonded micro-cable traces.

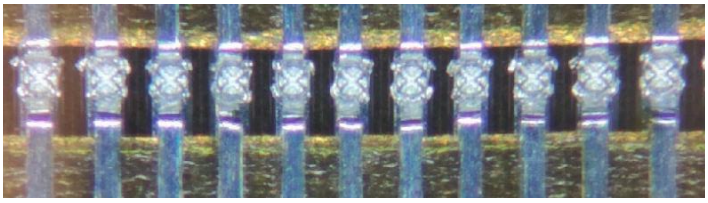

Fig. 4.6.10: Photograph of the tab-bonded row of microcable.

Before the bonding, an ultrasonic cleansing of the ASICs is performed in IPA, and then in deionized water. The photograph of the cleansing process is shown in figure 4.6.11.

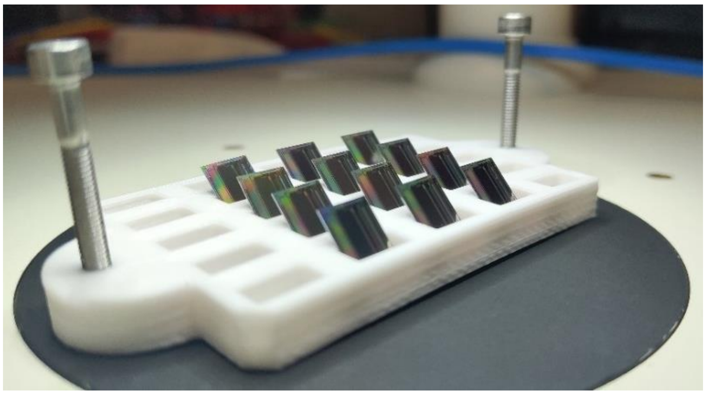

Fig. 4.6.11: STS-XYTER ASICs in a special box prepared for the US cleansing

Before the Tab-bonding of the micro-cables, the parameters of the bonding machine are selected for each set of the micro-cables. Test bonds are performed on the test zones of the micro-cable. The bonding quality is tested with a pull test machine (DOGE 4000).

After cleansing of the ASICs, the micro-cables are TAB-bonded to the 16 STS-XYTER-ASICs with a Tab bonding machine (F&K Delvotec G5 Wedge Bonder). The inputs of the even channels of the ASIC are arranged in the first pads row, while the odd channels pads are arranged in the second row. Two 64-channel signal cables are bonded to one ASIC in two layers. ASIC and micro-cables are fixed with vacuum on a special jig. The bonding row of micro-cables is aligned above the pad row on the ASIC with a help of µm-screws. The 64 traces are Tab-bonded to the ASIC. After that, the cable is fixed with a glue. The procedure is repeated for the second layer of the signal cable. A photograph of the Tab-bonding process is depicted in figure 4.6.12. A photograph of the ASICs bonded to the cables is shown in figures 4.6.13a and 4.6.13b.

After this step, the test zones of the cables are cut with a scalpel. We found, that during this procedure there is a risk of damage of the analog channels of the ASIC due to the ESD. That is why cutting is performed under an ESD fan on a conductive substrate. Compliance with these conditions allowed us to achieve zero number of dead channels after the assembly of the module.

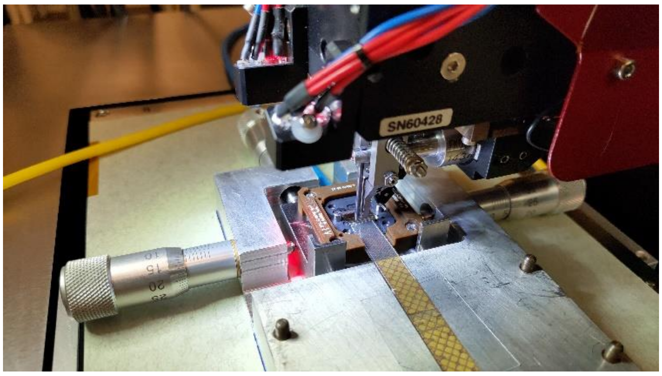

Fig. 4.6.12: Tab bonding of the micro-cables to the ASICs

Fig.4.6.13a: ASICs with top and bottom layer micro-cables

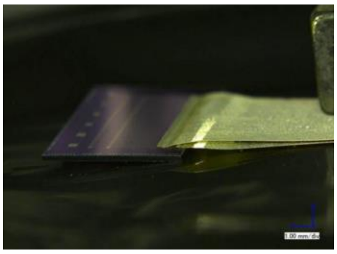

Fig. 4.6.13b: ASICs with two bonded cables. Source: CBM-TN [1]

4.6.2.2 Tab-bonding of the micro-cables to the sensor

The other side of the micro-cables is Tab-bonded to the sensor. The bottom layer cable is bonded to the even strips of the sensor, while the top layer is bonded to the odd strips. The sensor and the bottom layer of the micro-cables are fixed with vacuum on the sensor-fixture. The cable bonding row is aligned above the first pad row on the sensor and then Tab-bonded. At this stage, the bonding quality is checked with a Pogo-pin test circuit. If non-bonded traces are detected, they are repaired. Then the bonded row is protected with a glue line. The same procedure is repeated for the top layer cable. A photograph of the sensor Tab-bonding procedure is shown in figure 4.6.14.

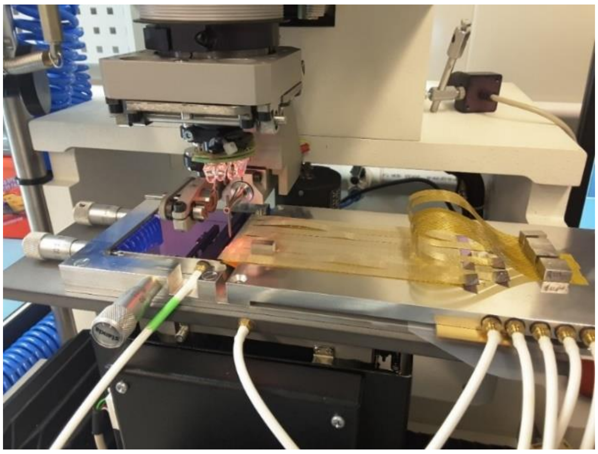

Fig. 4.6.14: Tab-bonding of the micro-cable to the sensor

4.6.2.3 Wire-bonding of the STS-XYTER ASIC to the FEB

Eight STS-XYTER ASICs are staggered onto the FEB PCB. In the third step, four ASICs with the shorter cables are glued with a thermally and electrically conductive glue and then wire-bonded to the contact pads of the FEB. The FEBs are tested beforehand and cleansed in ultrasonic bath to remove impurities. The assembled and tested ASICs are covered with a glob top. In addition, a thick aluminum shielding layer is fixed above the digital signal area of the ASIC to protect the top micro-cables from signal pick-up. Shielding is soldered to the corresponding pads on the PCB. Then the second row of ASICs with longer cables is assembled.

After the tests of the half module, the module is turned to the N-side, and the second and third assembly steps are repeated. Photographs of the wire-bonding procedure and a wire-bonded STSXYTER ASIC are shown in figures 4.6.15a and 4.6.15b.

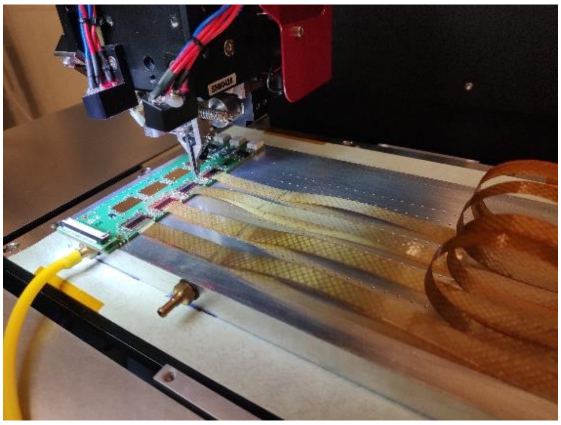

Fig. 4.6.15a: The wire-bonding of the STS-XYTER on the FEB

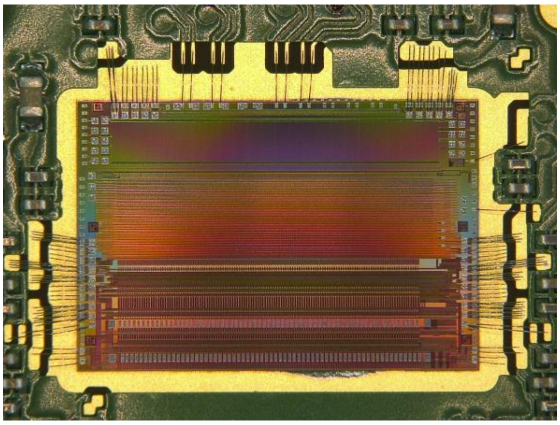

Fig. 4.6.15b: A wire-bonded STS-XYTER

4.6.2.4 Fixation of the shielding layer

Finally, the thin aluminum shielding is fixed with a glue on top and bottom of the module (on the P- and N-sides). The shield is not laminated to the micro-cables to allow clearance. The electrical contact is done by soldering the cables on special pads on the FEBs. A photograph of the assembled module with a shielding layer is shown in figure 4.6.16.

Fig. 4.2.16: Assembled STS module with shielding

4.6.3 Assembly fixtures

Before TAB-bonding, the substrates have to be fixated, and the traces of the micro-cables have to be aligned precisely above the bonding pads of the ASICs and of the sensors. Dedicated fixtures have been designed for these purposes, and several versions of such tools have been tested.

4.6.3.1 Fixture for the Tab-bonding of the micro-cables to ASICs

The fixture for the Tab-bonding of the micro-cables to ASICs consists of the mother base plate that allows positioning and fixation of the ASIC and the cable. To minimize the number of operations with ASICs, it has been decided to assemble the chip with the micro-cable directly on the Pogo-pin base plate. This base plate is mounted on the positioning block, which is installed into the mother base plate pocket and can be positioned with the µm screws. It allows a precise relative alignment of the bonded parts in X- and Y- direction. The ASIC is fixed on the Pogo-pin base plate with mechanical stoppers and vacuum. The bonding tests are performed with a Pogo-pin test circuit directly on the bonding fixture. The photograph of the fixture is shown in figure 4.6.17.

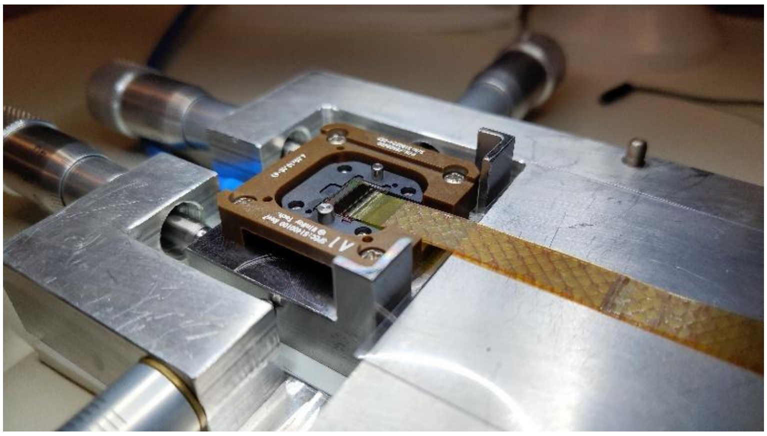

Fig. 4.6.17: Fixture for the Tab-bonding of the micro-cables to ASICs

4.6.3.2 Fixture for the Tab-bonding of the micro-cables to the sensor

The fixture for the Tab-bonding of the micro-cables to the sensor consists of the base plate with a vacuum fixation of the micro-cables and a vacuum positioning table for the sensor. After the sensor is fixed on the table with vacuum, it can be aligned in X and Y direction relative to the pads of the cables. For the assembly of the N-side, the fixture comprises a top part, which is used for the P-side cables and FEB. The photograph of the fixture is shown in figure 4.6.18.

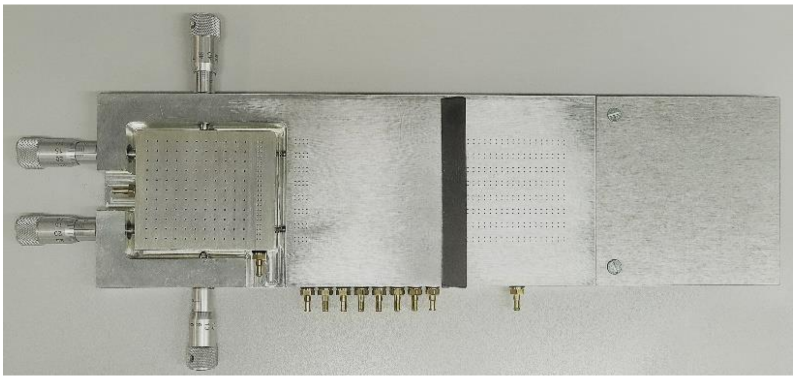

Fig. 4.6.18: Fixture for the Tab-bonding of the micro-cables to sensor

4.6.4 The QA measurements

For the quality assurance tests of the ASICs, a special Pogo-pin test circuit was developed and produced. It has 63 pins that contact dedicated pads on the ASIC (see figure 4.6.19). A test circuit is used for the certification of the ASICs before assembling. The following procedures are performed:

- Tests of the analog part: r/w the registers, tests with the internal analog calibration circuit;
- Tests of the digital part: r/w the registers, tests of the e-links functionality, tests with the test-pulse generator;
- Calibration of the ADCs;
- Calibration of the fast discriminator;
- Estimation of noise of each channel.

All results are stored in the production DB. The same test circuit is also used for the bonding test during the assembly. This procedure is described in more detail in Section 4.9. It is based on the noise measurements after each tab-bonding procedure. In case of a good connection, the noise level in the channel should increase due to the increased input capacitance. If the noise after the tab-bonding stays on the same level as it was before, the connection is bad and the bonding should be repaired. To minimize the pick-up, a test circuit is placed inside the shielding box (see figure 4.6.20).

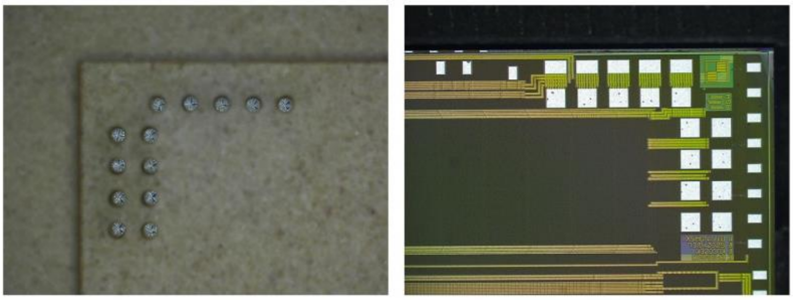

Fig. 4.6.19: Pogo-pins (left) and dedicated pads on the ASIC (right)

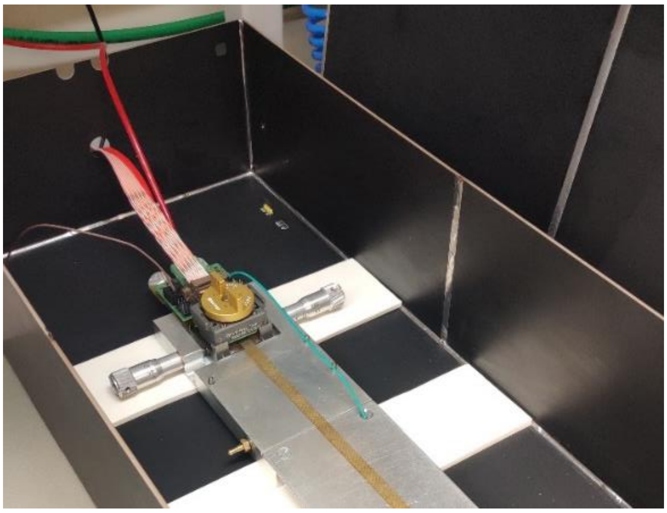

Fig. 4.6.20: Pogo-pin test circuit with STS-XYTER ASIC and micro-cable inside test box

For the optimization of the bonding parameters on the bonding machine, a dedicated test equipment is used. It is based on the pull test machine (DOGE 4000) with a special fixture (see figure 4.6.21). It allows us to perform pull tests of the wire- and tab-bonds to find optimum parameters for reliable US bonding.

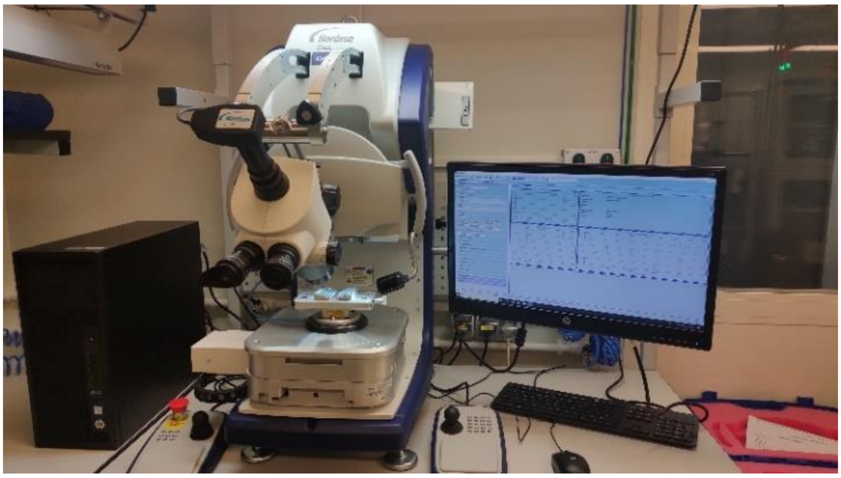

Fig. 4.6.21: Pull test machine

Before encapsulation of the contacts, a shortcut test is performed with an IR camera after the wire bonding of the ASICs on the PCB. This allows to identify shortcuts that may occur during the wire bonding due to high density of the bonding pads. A typical IR photograph of the STS-XYTER ASIC after wire-bonding is shown in figure 4.6.22.

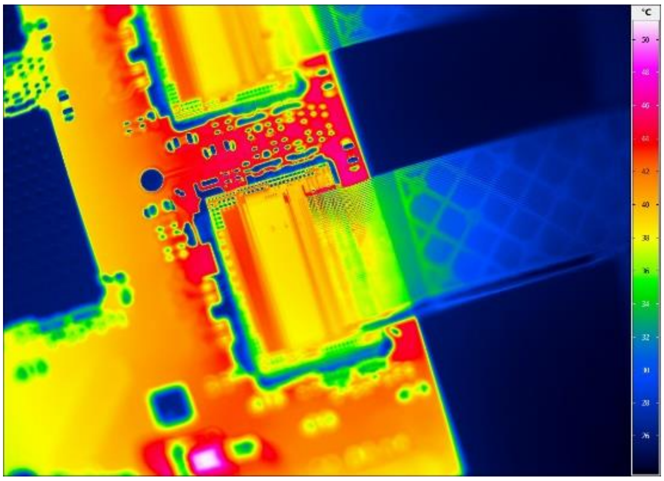

Fig. 4.6.22: IR photo of the wire-bonded ASIC on the PCB

4.6.5 Adhesives

Adhesives play an important role for the STS module assembly for

- Fixing of microcables on the sensor and ASIC;
- Protecting of the Tab-bonds on the STSXYTER ASIC and the sensor;
- Protecting of the wire-bonds on the ASIC: with Glob top dam & fill;
- Die-bonding of the ASICs to PCB.

Although only small amounts of glues are needed, they have to be chosen carefully with regard to their properties like viscosity, flow characteristics, curing, pot life and radiation hardness. The influence of the glues on the electrical properties of the sensor also should be taken into account, likewise the thermal and electrically conductivity where it is needed. The investigation of available glues was conducted by our colleagues from the GSI detector laboratory. The conclusions of this study [1] are summarized below.

Micro-cables have to be fixed at the edge of the ASIC and the sensor for ease of alignment as well as for strain relief. For this purpose a glue with a low viscosity and ion contamination, electronic grade, is needed. CERN recommended Epolite FH5313, which was tested, and the results were found satisfying.

For the protection of the TAB-bond rows on the ASICs and sensors a glue with low viscosity is needed, that spreads well over and between the bonds, but stops at the edges of the micro-cable. Since it is applied on the silicon sensors, it should have a low ion contamination. Epolite FH 5313 is also used for this purpose.

The wire-bonds that connect the ASICs to the FEB8 have to be protected with Glob-top Dam and Fill to avoid mechanical damage and environmental influences. The Dam-material should have a higher viscosity and form a perfect shape for the micro-cables of the second ASIC-row that lie on top of the first row Glob-top. The Fill-material should have low viscosity to be able to spread through the wire-bonds easily.

Polytec UV 2249 and UV 2257 have been chosen. The UV-curing of a few minutes allows to proceed quickly with the module-assembly. Since both glues are transparent, the bonds can also be seen after application and curing.

For the die-bonding of the ASICs to the FEB8, a conductive glue is needed to realize the ground connection of the chip, and good thermal coupling to dissipate the heat, that emerges from chip operation.

EpoTek E4110 has already been used for similar projects, and has the advantage of curing also at room temperature. To accelerate curing, but to avoid putting the whole module into the oven for curing, only the FEB-side is placed on a heating mat for two hours at 65 degrees.

The irradiation of Polymers like glues can cause a change of their properties. For example, the consistency, colors or mechanical properties can change. Since every glue contains ions, the leakage current of the sensors is also affected after application of the glue. To test the radiation tolerance of the glues, several micro-strip sensors of 1.5 x 1.5 cm^2 size have been prepared for irradiation tests at the TRIGA reactor of the Institute for Nuclear Chemistry in Mainz (see figure 4.6.23). Several glues were applied on typical areas for module- and ladder assembly: on the TAB-bonding-rows, on the sensor edge, and on the four points were the L-legs will be placed for the ladder-assembly.

Fig. 4.6.23: prepared small sensors for irradiation test.

The over-all leakage currents were measured before and after application of glue and after irradiation (see figure 4.6.24). Before the application of glue, the baby sensors show their typical behavior of the IV curves. After application of the glue, the shape of the IV-curves changes, but the saturated current values are similar to that before treatment. After irradiation, the current increases by two orders of magnitude as expected. It seems, that the chosen glues do not cause excessive leakage current in the sensor beyond the leakage expected for an unglued sensor. The lowest current was measured for Epolite FH 5313. More detailed tests will follow. [2]

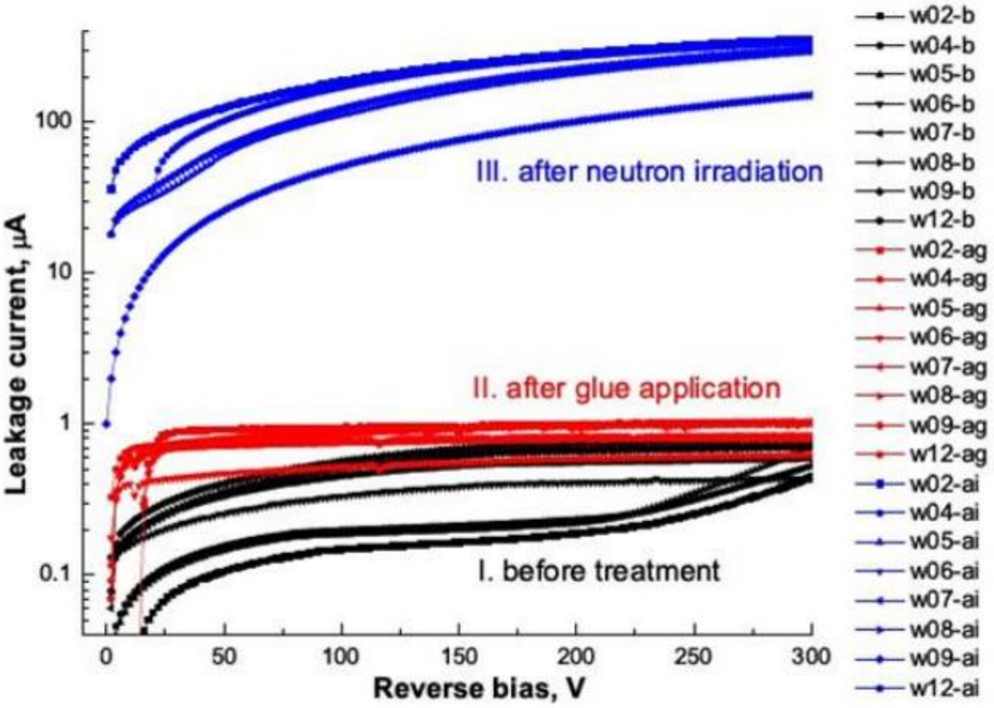

Fig. 4.6.24: I-V curves of the baby-sensors before and after glue application, and after irradiation. Source: CBM Progress report 2017 [2].

References

[1] The assembly of the STS-sensor-modules at GSI, Carmen Simons and Robert Visinka, CBM-TN-18005, November 22, 2018

[2] A. Lymanets et al, Radiation hardness of adhesives in the STS-module, CBM Progress report 2017

4.7 Ladder assembly

STS modules are in groups installed on the trusses made of high modulus carbon fiber. To have a 2.5 mm overlap between sensors in the direction of the truss, sensors will be glued to the frame with L-legs of different length. L-legs are made of fiberglass and thus sensors are electrically decoupled from the frame. Ladders consists of different sets of the modules depending on their position. BM@N STS will comprise 44 ladders of 6 types.

CF trusses are produced based on the technology developed by ALICE ITS group. For the grounding of CF trusses thick nickel foil is glued inside carbon fiber prepreg at the edge of the truss during production. For the positioning of the ladder on C-frame CF truss is glued on both sides to the grooves in the mounting blocks made of durastone. Mounting blocks are positioned on the C-frame with the help of two high-precision 4 mm ruby balls. For the bottom side of the truss V-type mounting block is used (Figure 4.8.1), SQ-type of the block is used for the positioning of the top side. Accuracy of the ladder positioning in X direction is less than 20 µm on 538 mm base (maximum pin-to-pin length of the ladder in BM@N STS).

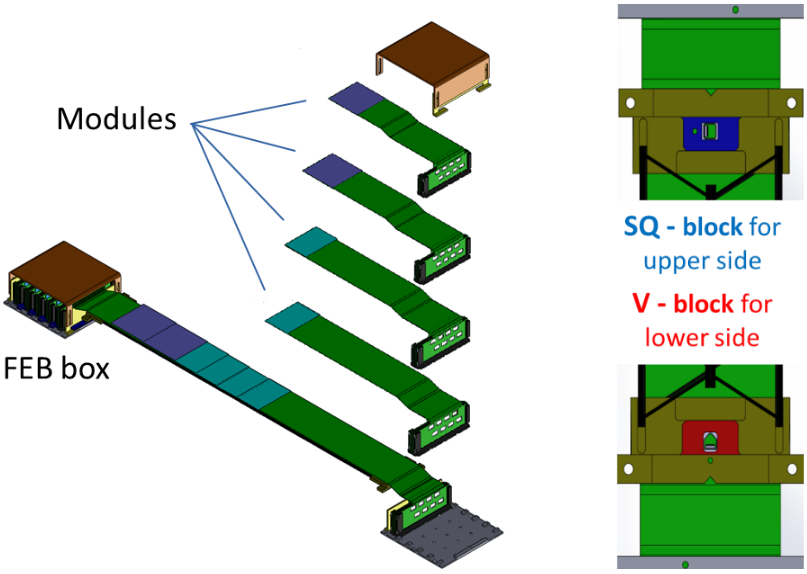

Fig. 4.7.1: Left figure is an exploded view of one ladder. Right figure shows two different types of mounting blocks on the both sides of the ladder: SQ block (top) is installed on the top edge of the truss, V block (bottom) is installed on the bottom side

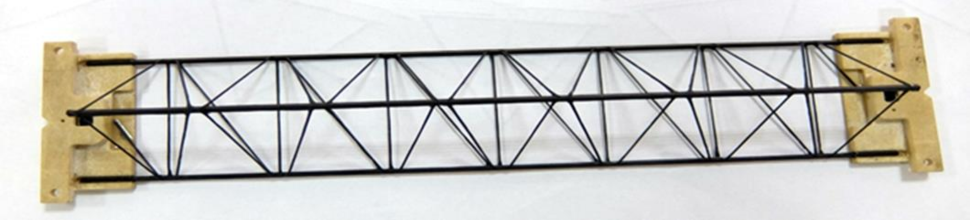

Fig. 4.7.2: CF truss with mounting blocks on both sides. Center holes in the blocks are used for the positioning of the ladder with ruby balls. There are also additional holes on the mounting blocks, which are used for the transporting of the ladder.

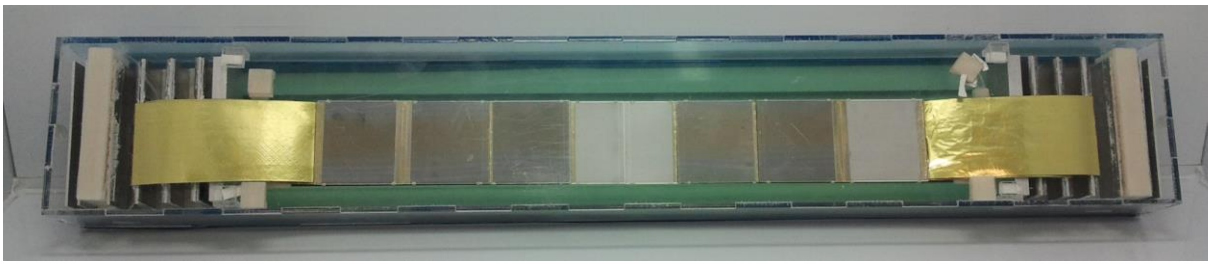

Fig. 4.7.3: Mockup of the ladder assembled of the dummy modules

4.7.1 Ladder assembly procedure

Ladder assembly procedure requires high precision of the positioning of the sensors on the base of the ladder length. Thus, a dedicated Ladder Assembly Device (LAD) with a set of jigs for the transporting and alignment of the components was developed and produced at Planar facility (Minsk) [1]. LAD should provide the following accuracy of the sensor positioning:

X coordinate	±15 µm on a 1200 mm base
	±12 µm on 180 mm base
Y coordinate	±50 µm
Z coordinate	±50 µm

LAD will also be used for the assembly of the ladders for CBM STS that is why the maximum base was specified to 1200 mm. LAD is equipped with an optical system, which is used for the monitoring of the sensor positions in a horizontal plane and has an accuracy of 2 µm. For the alignment of the sensors it comprises different sets of coordinate units with micro-screws for the adjustment of the position of the sensors and a lift unit for the positioning of the CF truss. Device is installed on the diabase table.

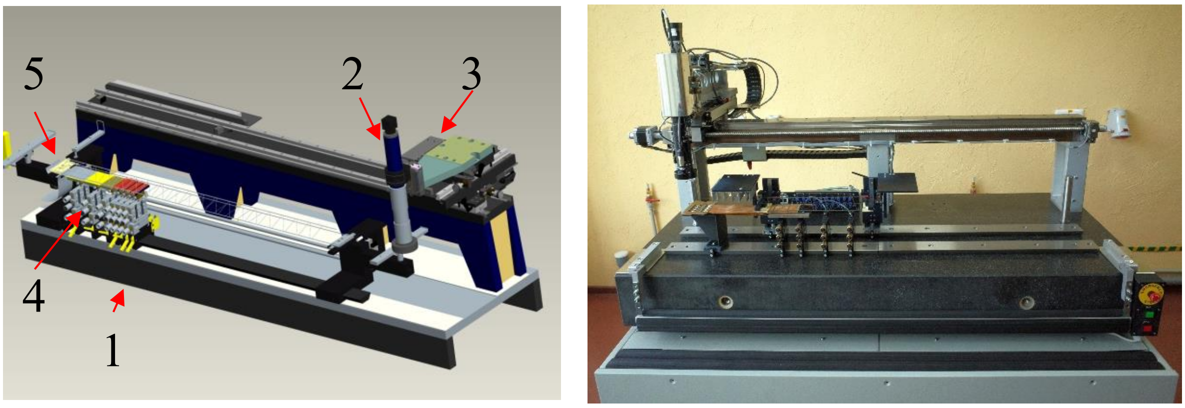

Fig. 4.7.4: Ladder assembly device consists of the following parts: Base table (1), Optical system (2), XYZ coordinate system for optics (3), XYϕ coordinate units for modules (4), CF-frame lift unit (5). Schematically view is shown at the left figure. On the right side the photo of the LAD from Planar facility is shown as of October 2019. SAT will be at November 2019.

Ladder assembly device was not yet delivered to the assembly site, SAT will be in November 2019. Thus, the described procedure is not yet finalized and will be tested on mockups first. Assembling procedure consists of the following steps:

1. Gluing of the L-legs to the sensors
2. Carrying of the module with transportation tool to the ladder assembly device.
3. Alignment of the module
4. Steps 2-3 are performed for all modules of the ladder
5. Positioning of the CF truss
6. Gluing of all L-legs to CF truss
7. Fixation of micro-cables stack to the truss
8. Assembling of the Feb-boxes on the both sides of the Ladder
9. Metrology of the ladder

4.7.2 Gluing the L-legs to the sensors

The sensors are mounted to the CF trusses with L-legs. The L-legs provide space between sensor and CF truss for the micro-cables from the modules in the center part of the ladder, electrically decouple sensors from the frame, and compensate any mechanical stress due to the thermal expansion. The L-legs are made of fiberglass with epoxy resin in a specially designed matrix. The shorter arm of the L-leg is glued to the position on the sensor, which was specified accordingly to the layout of the sensor. As an alternative, SLA 3D printing technology for the production of the L-legs also could be used.

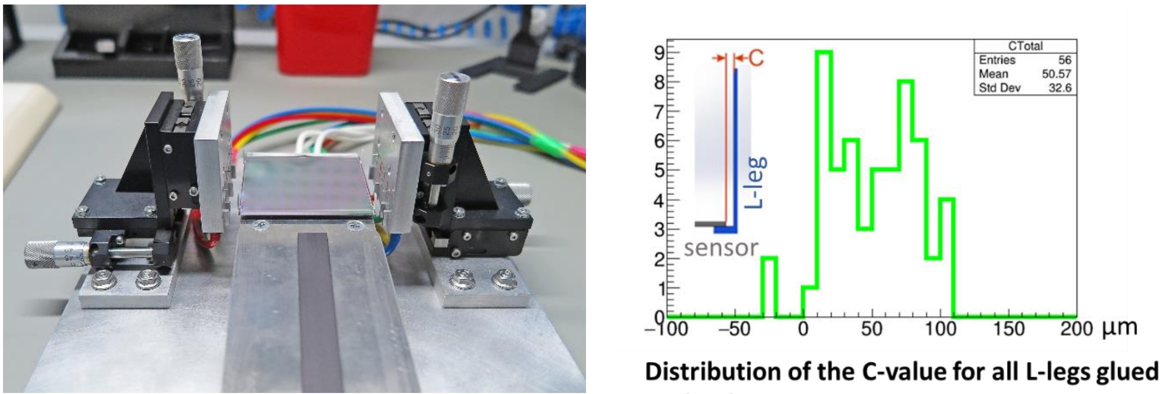

Distribution of the C-value for all L-legs glued to the dummy sensors

Fig. 4.7.5: Jig for the gluing of the L-legs to the sensors (left). The jig was tested on mockups, the distributions of the measured distances between the edge of the sensor and L-leg after gluing are shown in the right picture.

The jig for the gluing of L-legs to the sensors was developed and tested on mockups. The L-legs are glued to the sensor with CAF4 glue. The measured differences between the distance from the edge of the sensor to the end of the L-leg in the Y direction is less than 110 µm for all assembled dummies (Figure 4.8.5). This difference can be compensated with glue during the gluing of the L-legs to the truss.

4.7.3 Carrying the module with the transportation tool to the LAD

1. Before assembling of the ladder, the modules with glued L-legs are installed on the base plate, which has a dedicated corner backstops for the pre-alignment of the sensors and vacuum fixation (Figure 4.7.6).
2. The module transporting tool is positioned with help of dedicated pins on the base plate, and then put on the top of the module. The vacuum fixation is switched from the base plate to the transporting tool. The module is fixed to the transporting tool in the area of micro-cables near the sensor, the FEBs are mechanically fixed on the tool (Figure 4.7.6).
3. The module is located on the corresponding coordinate unit on the ladder assembly device with help of dedicated pins. After vacuum fixation is switched to the unit, the transportation tool is removed. The sensor is already pre-aligned on the coordinate unit.

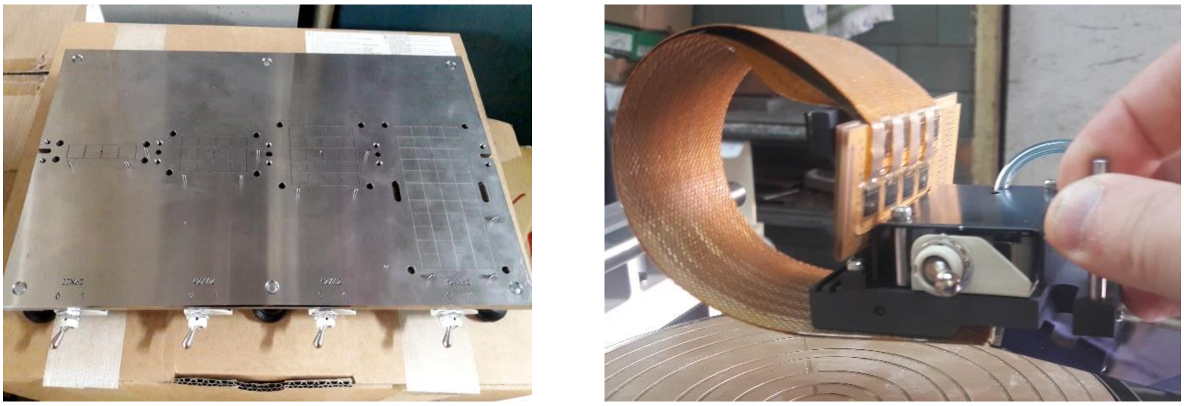

Fig. 4.7.6: Base plate for pre-alignment of the modules (left); Mockup of the module transporting tool (right)

4.7.4 Alignment of the modules

For each type of the ladder there is a corresponding set of coordinate units for the positioning of the modules. Each unit has micro-screws for the alignment of the sensor in X, Y and ϕ coordinates. For the monitoring of the sensor position, an optical control system of the ladder assembly device is used. Before the start of ladder assembly, a set of coordinate tables is installed on the LAD and aligned with an optical system. The origin point for the positioning of all elements is a high-precision ruby ball for the positioning of a V-type mounting block of CF truss. The alignment of the sensors is carried out based on the cross-marks on the surface of the sensors (Figure 4.8.7).

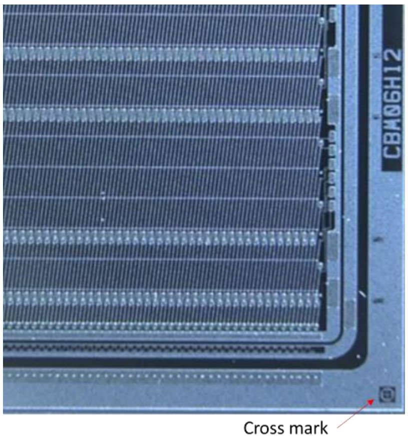

*Fig. 4.7.7***:** *Cross mark on the surface of the sensor produced by Hamamatsu. There are 6 cross marks on the surface sensor, which are used for the alignment of the sensors*

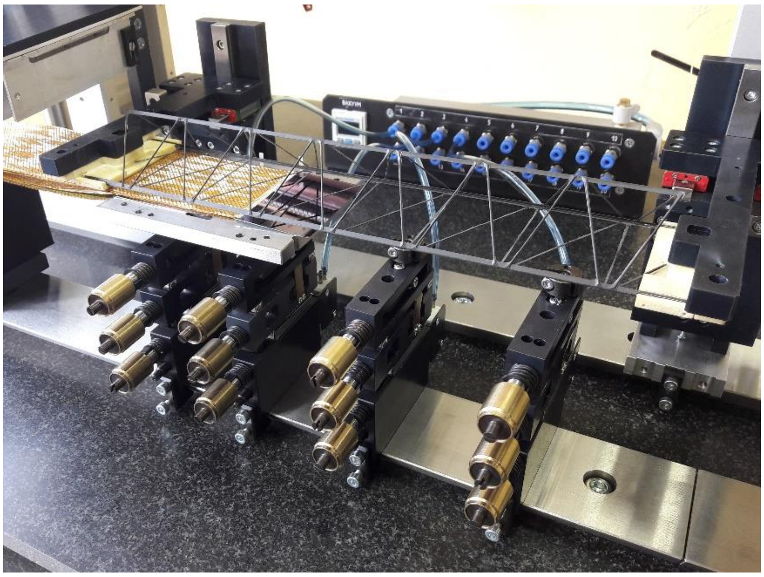

Fig. 4.7.8: Coordinate unit for one STS module on the LAD. The photo was made at the Planar facility during tests of the device with dummy components

4.7.5 Positioning of the CF Truss and gluing of the L-legs

1. The CF truss is installed in the start position on the lift unit. The mounting blocks are positioned with ruby balls on the lift.
2. The lift unit with the CF truss is lowered manually by guide rails to the mounting position
3. The alignment of the sensors and the CF-truss in vertical direction is inspected
4. Gluing of L-legs to CF truss with epoxy adhesive Araldite 2011

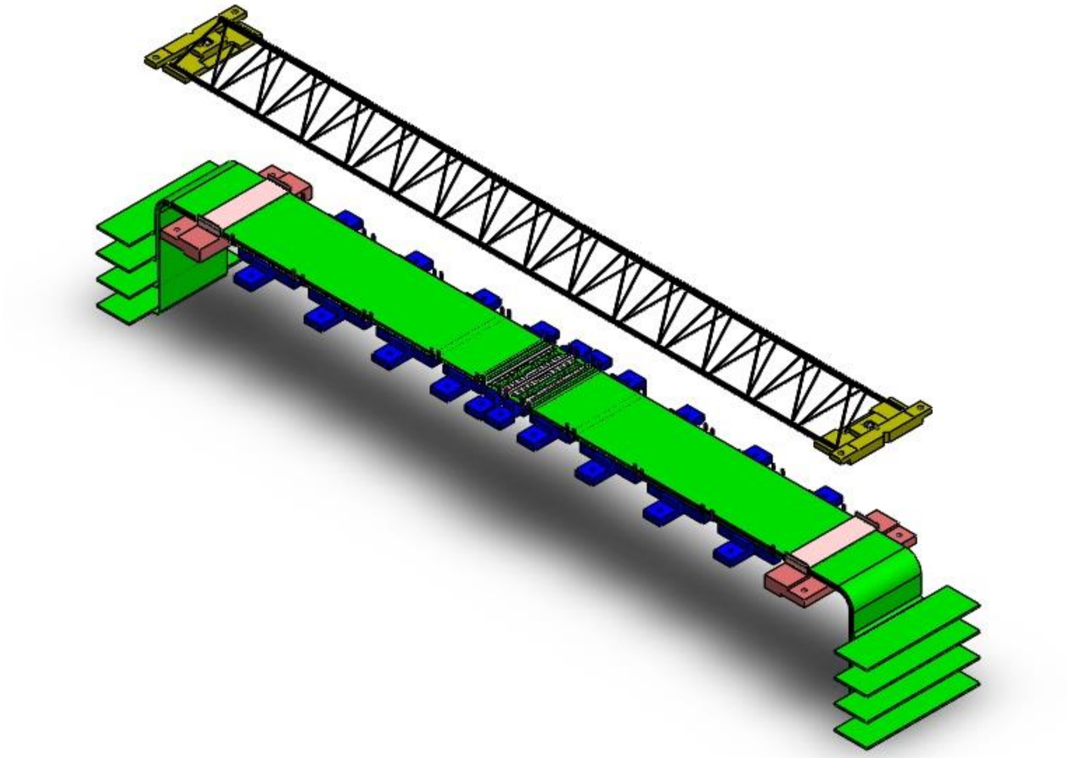

Fig. 4.7.9: CF truss is lowered down to the gluing position on the lift unit. The LAD is not shown

4.7.6 Assembling of the FEB-boxes on the both sides of the Ladder

Conceptually each ladder consists of two parts: an ultralight-weight central part with precisely positioned sensors, and a “heavy” part with readout electronics, which needs cooling. After assembly of the central part of the ladder top and bottom, the stacks of micro-cables should be fixed with a clamp to the truss on the edges to protect the sensors from any mechanical stress on the other side of the module. The FEBs are glued on thermal fins for the heat transfer from readout electronics. Those fins should be mounted to the base plate of the FEB box through a thermal grease. The fins are fixed in their position with screws. After the full ladder is assembled, it is transported with a ladder transporting tool to the metrology instrument.

4.7.7 Metrology of the ladders

The three-axis measurement of the ladder will be performed after assembly. The measured data will be stored into production data base. The three-axis measuring instrument has been re-commissioned at GSI for the metrology of the sensors and ladders for the CBM STS [2]. To perform the metrology for BM@N STS ladders, a CNC coordinate measuring machine Crysta-Apex S9206 with sets of instruments was ordered from Mitutoyo[15]. For the measuring of the positions in the XY plane, the pattern recognition algorithm is used [3], the sensor position is measured by finding the cross marks on the surfaces of the sensors. The origin point is assigned to the ruby ball position in the V-form mounting block of the ladder. The XYZ profile of the first

---

[15] https://www.mitutoyo.com/wp-content/uploads/2013/01/2097_CRYSTA_ApexS.pdf

assembled at GSI ladder was measured at GSI with a custom-built metrology instrument [4]. An example of the profile is shown in figure 4.7.10.

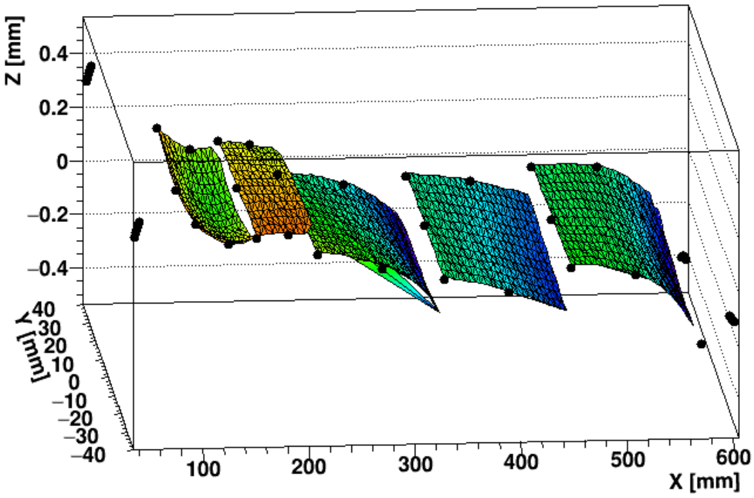

Fig. 4.7.10: Metrology of the CBM ladder performed at GSI. Nominal Z positions of the sensors are shifted to zero

4.7.8 Tests of the glues

During the assembly of the STS ladders, several kinds of glues are used. Depending on their properties, different adhesives vary in their consistence from liquid to viscous, curing method and mechanical strength. Their use in a radiation hard environment imposes additional requirements on the radiation hardness and long-term stability. The following glues were tested: Epotek T7110, Araldite 2011, Epotek 301-2, Epolite FH 5313, Epotek302-3M and silicone glue CAF4.

The adhesives were applied on the surface of the 1.5x1.5 cm^2 "baby" sensor produced on the same technology as real STS sensors. The influence of the glues on the electrical properties of sensors was tested by measuring the leakage current before treatment, after glue application, and after irradiation in a controlled environment. The results are shown at figure 4.7.11. After application of the glue, the characteristic IV curves vanish: all curves reach saturation before 30 V. The saturated current of the sensors is compared to the one before treatment. The highest current is drawn by the sensors w02 and w04, that have been both treated with Epotek 7110 glue in different sensor areas. The lowest current corresponds to the sensor w09 where Epolite FH 5313 adhesive has been applied.

After irradiation, the current increases by two orders of magnitude as expected [5]. According to [6], all tested glues can withstand a radiation dose up to 1 MGy. The mechanical properties of the glues were tested with a pull test. A set of 28 L-legs was glued to the sensors with different types of glues. A 1 mm hole was drilled in the longer arm of the L-legs before gluing to perform the pull tests. The plot (figure 4.7.12) shows the pull-off forces for different adhesives.

For the gluing of the L-legs to the sensors, the glue CAF4 was chosen. It has a minimal pull-off force of about 3.5-7 N, and is elastic enough to compensate mechanical stress caused by different CTE for silicon and carbon fiber materials. It's influence on the electrical properties of the sensor turns out to be negligible.

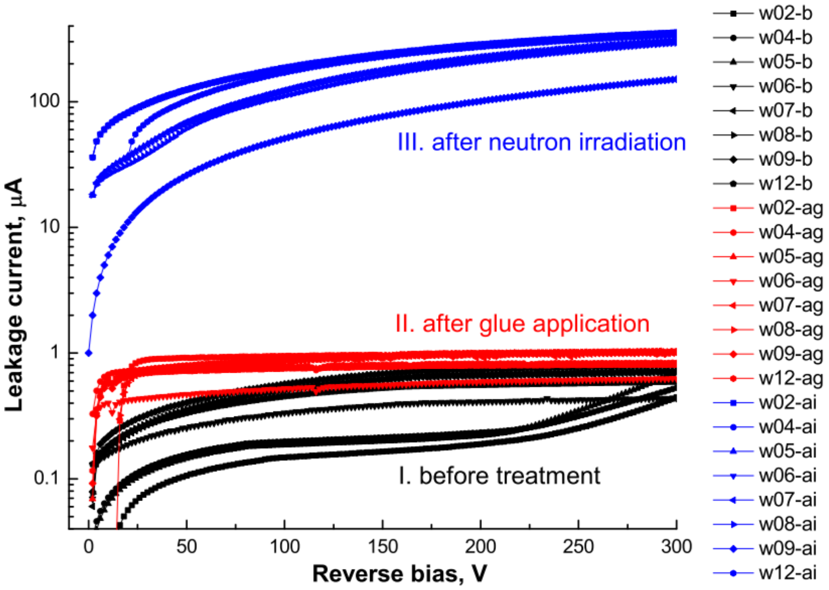

Fig. 4.7.11: Current-voltage curves measured before treatment, after glue application and after irradiation for different kinds of glue.

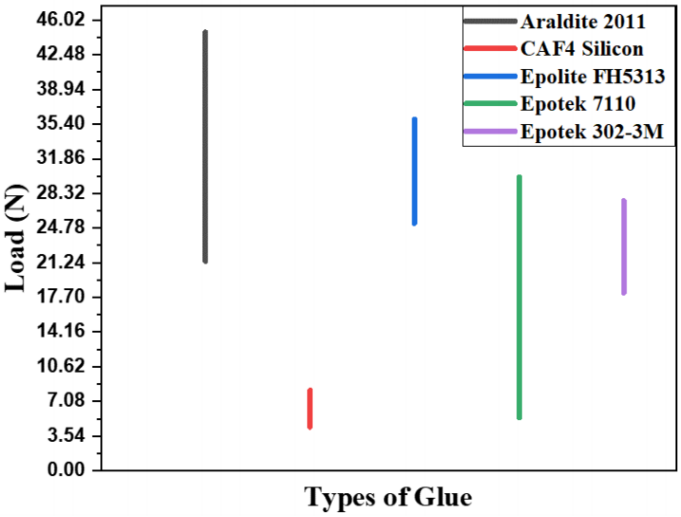

Fig. 4.7.12: Pull-off forces measured for different kinds of adhesives.

References

1. V. Elsha et al., Design of an STS ladder assembly device, CBM Progress Report 2017, p.40
2. U. Frankenfeld, S. Mehta, O. Vasylyev, STS Ladder Assembly, CBM Technical Note 18011
3. E. Lavrik, I. Panasenko, H. R. Schmidt, Advanced Methods for the Optical 255 Quality Assurance of Silicon Sensors, accepted for publication in Nucl. Inst. Meth. A, arXiv:1807.00211
4. E. Lavrik et al., NIM A935 (2019) 117
5. A. Lymanets et al., Radiation hardness of adhesives in the STS module, CBM Progress Report 2017, p. 39
6. F. Guuarino, C. Hauviller and M.Tavlet, Compilation of radiation damage test data Part IV: Adhesives, ISBN 92-9083-189-8

4.8 Support frames and system integration

The STS stations are assembled by installing the ladders onto support frames. In order to provide an overlap of the sensors in Y direction. i.e. between neighboring ladders, the ladders of one station are divided in two groups. The ladders from the first group are oriented upstream the beam, while the ladders of the second group are oriented downstream. The orientation of the ladders is shown in figure 4.8.1. Both groups are installed on the corresponding support frames in a such way that the sensors form a continuous coordinate plane without dead zones. The absence of dead zones is determined by overlap of the ladders, and of the sensors on the ladders. Those halves of one station are called units. The units consist of two quarter-stations located on the right and left sides from the beam. Each quarter is installed on the rails made of aluminum alloy. The rails are used for the installation of a quarter station into the mainframe support. Also, they provide the opportunity to pull the quarter stations away from the beam pipe during the beam tuning. The system should provide the repeatability of the positioning of each frame with a high precision in a plane perpendicular to the beam pipe.

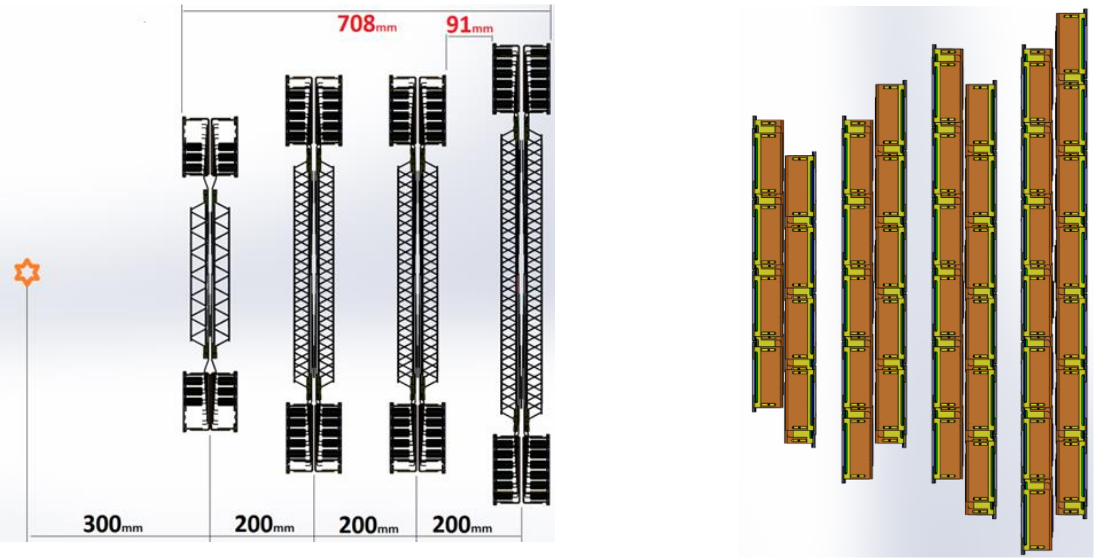

Fig.4.8.1 Ladders of the STS stations. Left: Side view. Right: Top view

4.8.1 C-frame

The support frame of one quarter station is called C-frame. A schematic view of the quarter station is shown in figure 4.8.2. One station comprises four C-frames of two different symmetries – right (R) and left (L). The C-frame consists of two parts: a light C-frame made of carbon fiber panel, and a heavy part made of aluminum with integrated heat-exchanger for the cooling of readout electronics.

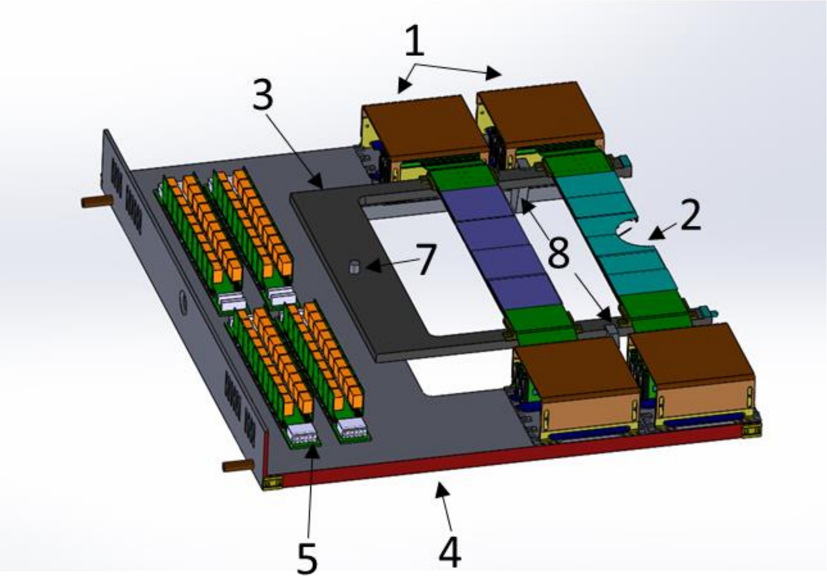

Fig. 4.8.2: Schematic view of the quarter of the 1st Station. The following components are shown with arrows: 1 – FEB boxes; 2 – sensors; 3 – light C-frame; 4 – heavy C-frame; 5 – power boards; 7 – aluminum sleeve; 8 – aluminum supports.

The light part of C-frame serves for the mounting of the ultralight part of the ladder, i.e. the CF truss with sensors, and provides a high accuracy of ladder positioning. It is made of a carbon fiber sandwich panel with a glued small aluminum base plate with ruby-ball pins for the positioning of the ladders. The CF material has the following benefits:

- low CTE and thus high thermal stability of the system is achieved;
- The ladder trusses are also made of CF and therefore no mechanical stress between C-frame and ladder occurs due to thermal expansion;
- The CF sandwich panel is very light and rigid which is needed for the precise positioning.

However, it also has disadvantages due to the complexity of the machining. That is why aluminum base plates will be glued to the surface of light part of C-frame.

The sandwich panel for the C-frame production was not yet chosen. However, the technology of the manufacturing of the light part of C-frame was approved on the mockups. This technology consists of the following steps:

- The C-frame is cut from the CFRP sandwich panel with water-jet cutter
- The aluminum embedded parts are glued to the CFRP surface of C-frame in places for precise holes
- The surface lapping of the embedded parts is made to achieve the flatness of less than 20 μm
- Precision drilling of holes for the pins with ruby ball

The mockup of the light C-Frame produced for the test setup at mCBM is shown in figure 4.8.3.

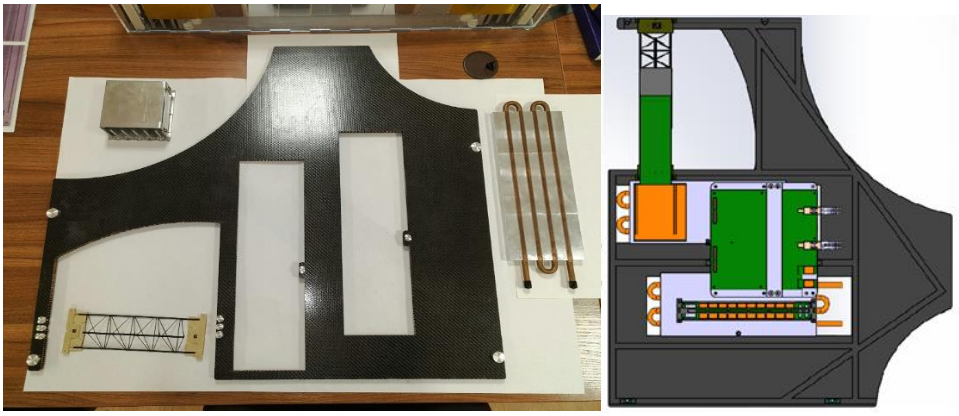

Fig. 4.8.3: CF sandwich panel C-frame for one ladder assembled for the mCBM experiment.

The heavy part of C-frame carries the boxes with front-end electronics, which does not require precise positioning but needs extensive cooling. It is made of an aluminum plate with an aluminum pipe glued inside for the cooling liquid.

The two parts of one C-frame are connected together via an aluminum sleeve, which is glued to the light part and provides freedom of relative movement of both planes within 1 mm in XY plane. A precise sleeve is used for the positioning of the C-frame with a calibrated pin during the assembly of the station. To provide the required flatness of the light C-frame, two supports are installed on the shorter arms of the heavy C-frame. Such a connection provides a good relative flatness of both planes, and a relative freedom in the XY plane. This is needed to compensate different thermal expansion of both parts. The positioning of the light part is performed during the assembly of the station.

4.8.2 STS unit

Two C-frames of “R” and “L” geometry as shown in figure 4.8.4 are assembled into one unit. The C-frames are installed on the rails at both sides of the mainframe, and then are pushed to the beam pipe. The light C-frames have dedicated locks on the connecting sides. The locks fix the light C-frames of one unit and form one plane. The heavy parts of the C-frames are not connected together to provide a thermal gap.

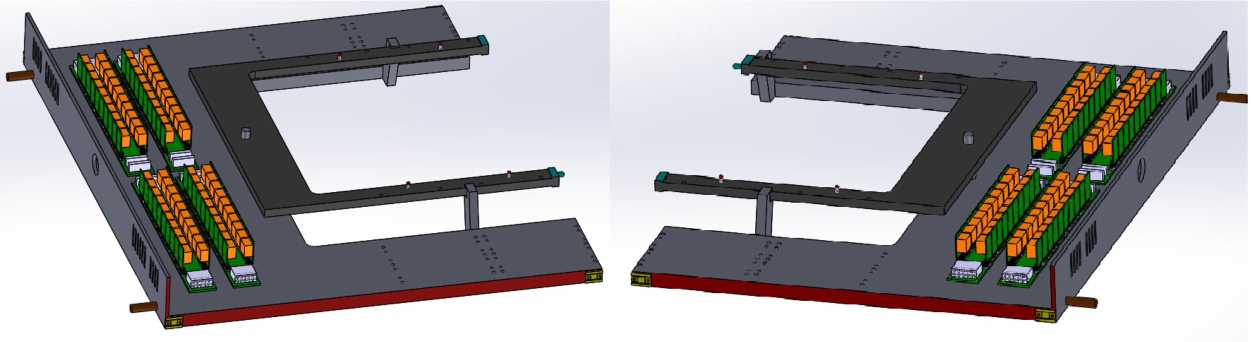

Fig. 4.8.4: Two quarters of the 1st station are assembled into one unit

4.8.3 STS Station

One station consists of two units. While the first unit is oriented downstream the beam, the second unit is oriented upstream the beam. Thus, the R-type C frame of the 1st unit and the L-type C-frame of the 2nd unit are located on the same side from the beam pipe and vice versa. The "R" and "L" C-frames of two different units are joined together with a calibrated pin, which is firmly installed into the sleeves in the light frames. Two C-frames are pushed together to a final position, both ends of the pin are fixed in a positioning block on the mainframe (see figure 4.8.5). Two C-frames of each unit are fixed together with a dedicated lock. Thus, the coordinate plane formed by four C-frames is positioned relative to the calibrated points on the mainframe.

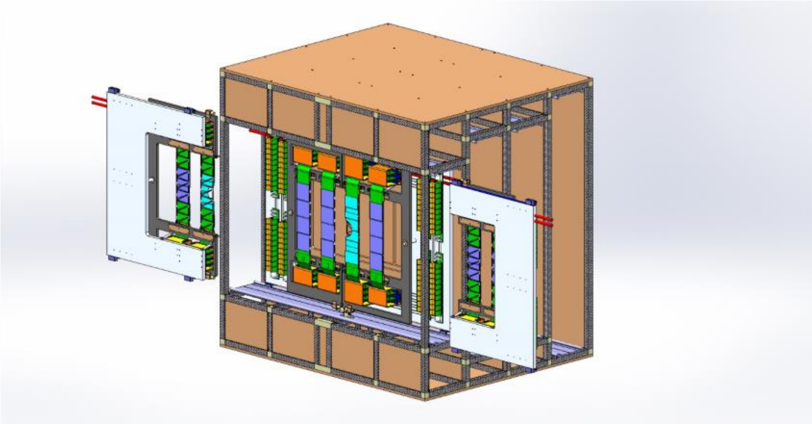

Fig. 4.8.5: STS Mainframe with the 1st Station installed.

4.8.4 STS Mainframe

The mainframe of the BM@N STS will be installed inside the BM@N dipole magnet between the target and the first GEM plane. The mainframe is made of CF profiles with a cross section 20×20 mm^2. The mainframe should carry four stations, and provide accurate and repeatable positioning of the light C-frames with a precision of less than 0.5 mm perpendicular to the beam direction. It should also carry a piece of the BM@N STS beam pipe, and provide thermal and electromagnetic shielding. The walls of the CF sandwich panels with the foam insulation will be mounted to the mainframe. The preliminary design of the mainframe is shown in figure 4.8.6

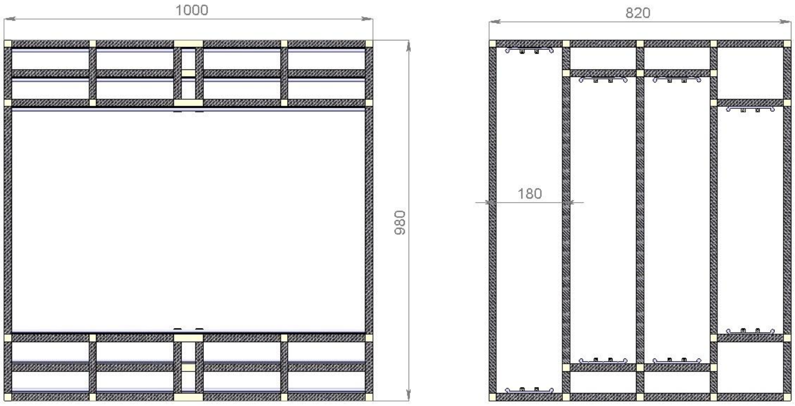

Fig. 4.8.6: Schematic view of the mainframe made of CF profiles

4.9 Quality Assurance of Module Assembly

The quality assurance (QA) procedures follow the technological operations of the assembly process. The initial components of the modules, such as sensors, micro-cables, ASICs, the front-end PCBs, etc. will be tested by the producers, and the results will be recorded in the detector construction data base.

The following QA actions will be performed at the module assembly site:

1. The reference measurement of the magnitude of noise in the inputs of the ASICs before bonding, using the pogo-pin device.
2. Tests of bondings between the micro-cable and the ASIC after bonding of each of two micro-cables to the ASIC, by measuring noise with the pogo-pin device.
3. Tests of bondings between the micro-cable and the sensor after bonding of each of two micro-cables to the sensor; performed by measuring noise in the ASIC channels with the pogo-pin device.
4. Measurements of front-end board (FEB) electrical parameters for quality checks of the assembly operations.
5. ASIC functionality tests - when the chips connected to the sensor are being bonded to the FEB.
6. Data read-out tests of a completely assembled module with undepleted and depleted sensor.
7. General functionality test (under development) of the module with the biased sensor and data readout via FLIB to a full-featured DAQ system. LASER or a radioactive source will be used.
8. Endurance test (under development) of the module with multiple power cycles and power supply voltages changing within full range of the specification limits.
9. Long term stability test (under development) with the module fully powered for certain time period.
10. After the modules are assembled on a ladder, some of the tests above should be repeated for each of the modules.

4.9.1 QA tests of the micro-cable bondings

Tests of the micro-cable bondings may be performed after completion of every micro-cable bonding operation. They are based on measurements of magnitude of noise at the ASIC inputs. There is an increment in the noise amplitude when an additional capacitance is connected to the amplifier's input. If the expected increase is not observed - the connection, i.e. bonding, is absent. The magnitude of noise is obtained from measurement of the S-curve using the internal pulse generator of the ASIC. The scheme of the setup is depicted in figure 4.9.1. A chip with a bonded micro-cable (or without it, for reference measurement) is placed in the pogo-pin device, which provides connections to the readout electronics as shown in figure 4.9.2. After the measurement is completed, the chip may be easily extracted for further assembly operations.

Components of the sensor module together with the pogo-pin device are placed inside the shielding box during the measurement (see figure 4.9.3) to avoid the influence of electromagnetic interference. The code “BondingTest" was developed to perform these tests. It runs in Linux PC and communicates to the ASIC using IPbus protocol via the chain : copper ethernet, ethernet to SATA D-LINK adapter, SATA link, AFCK, gDDB FMC1 board, twisted pair links to the pogo pin. It is a standalone application written in C++ using the CERN Root toolkit [1] and CERN IPbus software suite [2]. The measurement takes a few minutes depending on the technological operation. States of each electronic channel of the ASIC are shown on the GUI in colors indicating good and bad bonding, noisy and dead channels (see figure 4.9.4). A histogram of measured noise versus the channel number is displayed together with similar histograms measured at the previous technological steps. The results of the measurements are stored in root-files and also can be recorded in the detector construction data base.

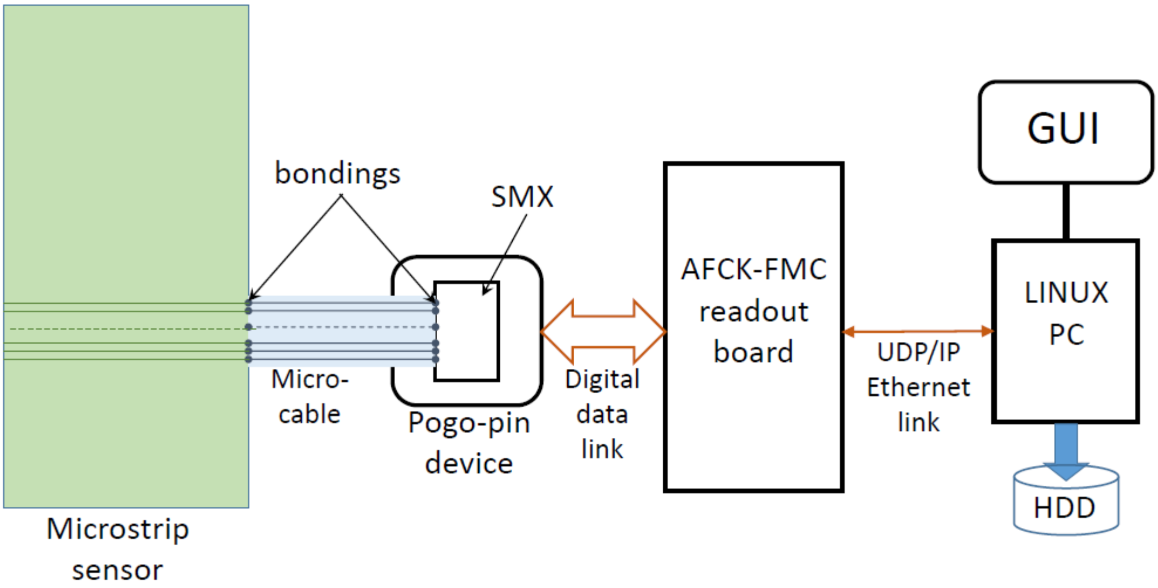

Fig. 4.9.1: Schema of the ASIC inputs noise measurement with the pogo-pin device. The magnitude of noise indicates the presence of a contact between the wire of the micro-cable and the ASIC input, and between the wire and the micro-strip of the sensor. The ASIC is connected to a sensor with two micro-cables, but only one of them is depicted here for illustration purposes.

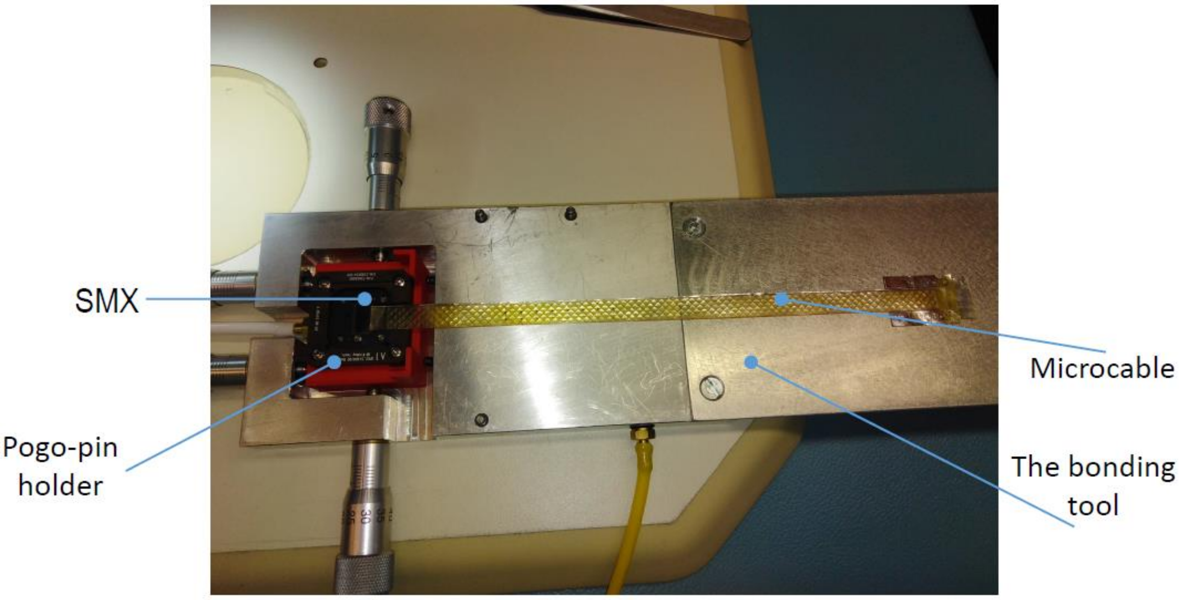

Fig. 4.9.2: ASIC ("SMX") bonded to a micro-cable installed in pogo-pin holder on the bonding tool.

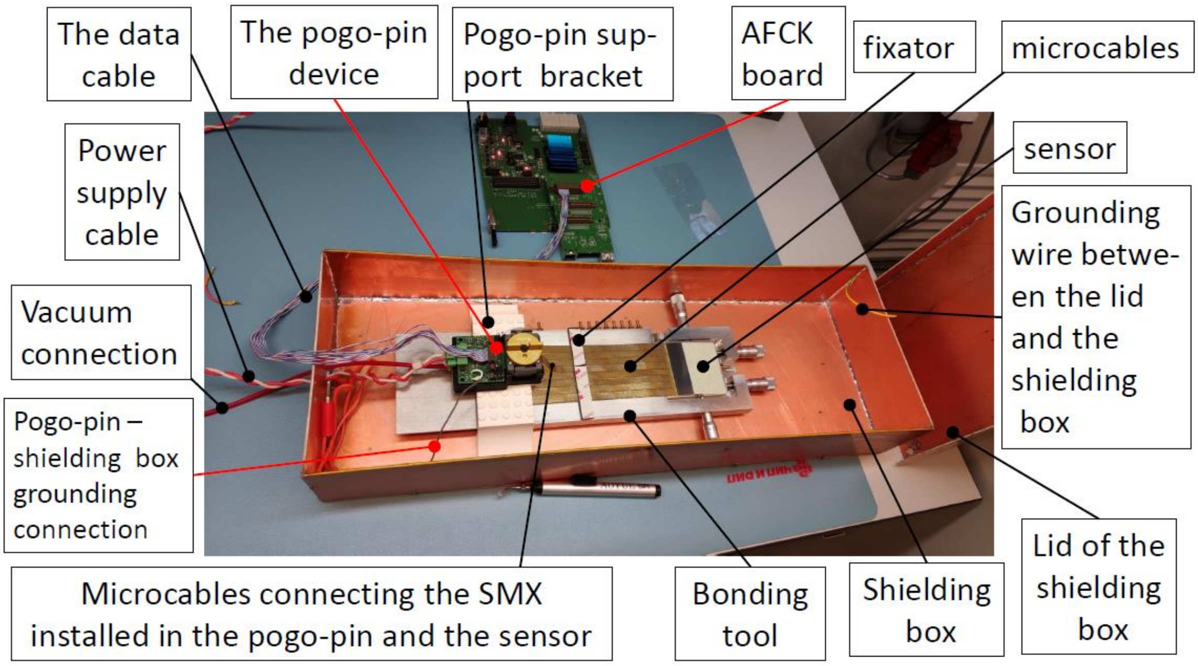

Fig. 4.9.3: Sensor with micro-cables bonded to ASICS (SMXs) on a bonding tool inside the shielding box, ready for bonding QA test. One of the bonded ASICSs is inside the pogo-pin device placed on a bracket above the tool. The data cable connects the pogo-pin with AFCK readout board.

chip code : DA2A542

operation : 2-nd(odd) cable-to-sensor

Total good channels : 122

Cable-1 good channels: 59

Cable-2 good channels: 63

Fig. 4.9.4: GUI of the Bonding test program. Test of bondings between the ASIC 2-nd micro-cable and the sensor. Histograms of the magnitude of noise versus the channel number are

displayed for each of the micro-cables. States of the electronic channels are indicated by rows of color labels below the histogram; the row corresponds to bonding operation.

4.9.2 QA tests during the FEB assembly

LDOs, and SMXs connected to a sensor, will be mounted and bonded on a FEB.
The following QA tests are foreseen:

1. Check of capacitance of the decoupling capacitors installed on the board.
2. Check of input and output resistance in the FEB power supply circuits after installation and bonding of the LDOs.
3. Check of resistance at the LDO output after ASIC is bonded to the FEB.
4. Components temperature check with the infrared camera after powering the FEB.
5. ASIC functionality tests will be performed after bonding a row of four ASICs to the FEB (2 rows per FEB). The FEB should be powered and connected to the AFCK board via a data cable. The python script running in a PC will perform the test using IPbus protocol.
6. Tests of the grounding connections of the module's shielding, FEBs, and radiators, after the module assembly is completed.

When possible, after an operation is completed, a photo should be taken. All the photos and results of the tests will be stored in the detector construction data base.

4.9.3 The data read-out tests of the assembled module

After a module is completely assembled with all cables and shieldings, and the FEBs are mounted on the radiators, the data read-out tests will be performed on a test stand as shown in figure 4.9.5. The scheme is depicted in figure 4.9.6.
The tests include:

- measurement of noise magnitude for each of 2048 channels of the unbiased sensor.
- biasing of the sensor and measurement of I-V curve.
- measurement of noise magnitude in channels of the depleted sensor.
- tuning of the FADCs and fast discriminators.
- test of the data read-out via FLIB.

The noise measurements and the tuning operations will be perfomed by codes running in the PC via IPbus protocol. The data read-out will be tested via the fiber optics link between AFCK board and FLIB unit (see figure 4.9.6). The results will be recorded in the detector construction data base. The example of noise measurement of the depleted sensor is depicted in figure 4.9.7. If the measured magnitude of the noise is within certain limits, the corresponding channel is considered as “good", otherwise it is “bad". In this way, the measurement gives QA information of the sensor, that may be combined with the QA data recorded at the microcables bonding operations. The combined data give an overview of “evolution" of electronic channels of the module during the assembly. It allows to determine at which operation a problem appears and to improve the assembly process.

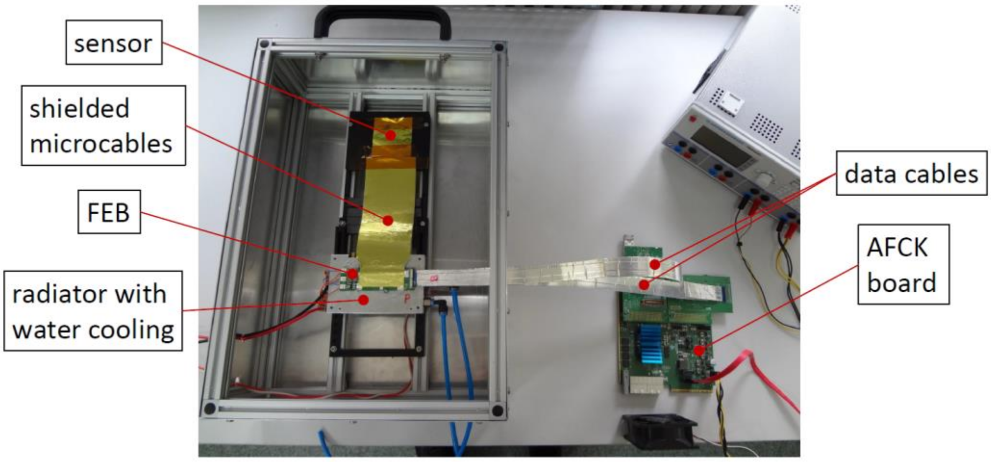

Fig. 4.9.5: Test stand for data read-out tests of the assembled module.

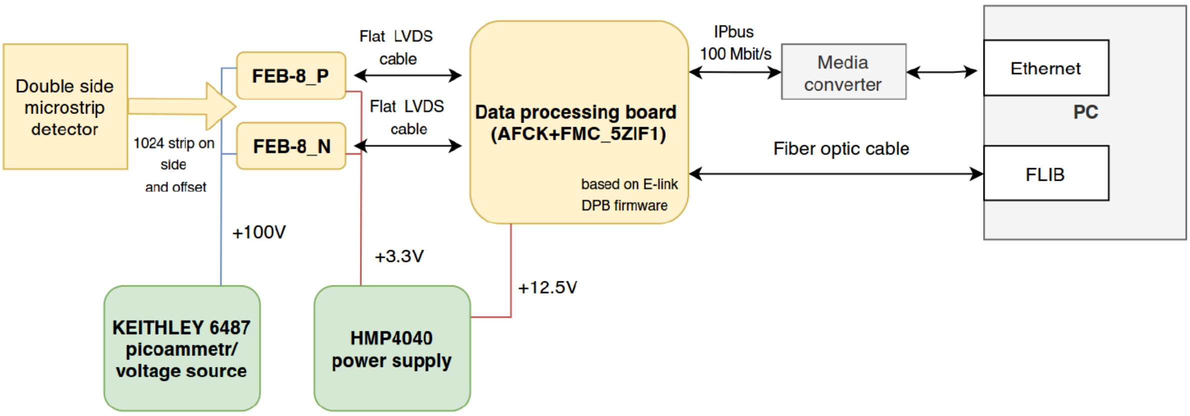

Fig. 4.9.6: Scheme of the module general functionality tests

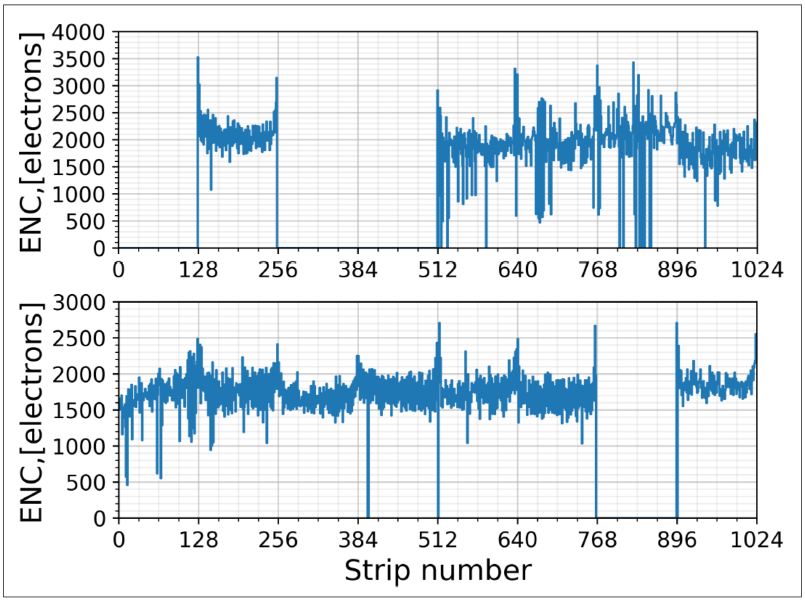

Fig. 4.9.7: Depleted sensor. Noise versus strip number. Top: N-side of the sensor - three ASICs do not work; bottom: P-side of the sensor - one ASIC doesn't work. There are also several separate „dead" channels.

4.9.4 Tests of the assembled modules

The assembled module should pass more tests before it is used for the ladder assembly. They are:

- The general functionality tests. The module is fully powered and irradiated using LASER or a radioactive source. The data are read-out via FLIB by DAQ system.
- The endurance test. The module should stand multiple power cycles and power supply voltages changing within the full range of specification limits.
- The stability test. The module should be powered and keep its operational parameters during certain period of time.
-

After the modules are assembled on a ladder, some of the tests above will be repeated separately for each module of the ladder.

References

[1] Rene Brun and Fons Rademakers, ROOT - An Object Oriented Data Analysis Framework, Proceedings AIHENP'96 Workshop, Lausanne, Sep. 1996, Nucl. Inst. & Meth. in Phys. Res. A 389 (1997) 81-86. See also ttp://root.cern.ch/

[2] C. Ghabrous Larrea, K. Harder, D. Newbold, D. Sankey, A. Rose, A. Thea and T. Williams, \IPbus: a exible Ethernet-based control system for xTCA hardware", JINST 10 (2015) no.02, C02019.

4.10 Low and High Voltage powering scheme for STS

Each STS-unit consists of two quarters (left and right) which are independently of each other supplied with LV, HV, data cables and cooling liquid for the cooling of the readout electronics. The structure of a quarter-station is described in details in Sect. 4.8. It consists of two supporting parts: light and heavy C-frames, which serves as a mechanical support for the ladders and readout electronics as well as a cooling interface. Each quarter station has its patch panel with all interface connections located on the outer side of the heavy C-frame. HV powering of the sensor as well as a readout of the signals are performed via a set of 32 micro-cables connected to the 16 ASICs installed on two FEBs. (The module construction is described in Sec. 4.6). Silicon sensors need to be biased in a floating manner with 0 V and –V applied to p- and n-sides. The value of the bias voltage for the non-irradiated sensors is expected to be in the range 80-150 V. However, for the end-of life of the sensors it could be increased up to 500 V. FEBs are readout via GBTxEMU boards over twinax data cables. To separate data acquisition electronics from the biasing potential on the front-end electronics a dedicated AC-coupling capacitor with a value of 3.3 nF are installed on the FEBs for each signal line.

The z-distance (along the beam axis) between two C-frames belonging to consecutive STS-units is equal to 200mm and each cooling plate has a thickness of 14 mm. The remaining 172 mm distance is shared by the FEB boxes (2 x 57 mm) and the stacks of-cables. The distance between the closest edges of FEB-boxes installed face-to-face amounts to 10 mm (see figure 4.10.1). This space will be used for the data cables (AWG 40 twinax). The LV and HV cables will be stacked on the back side of the heat-exchanger plate. The gap between neighbor FEB boxes installed onto one C-frame is 28 mm (see figure 4.10.2). This space will be used for the LV and HV cable connections.

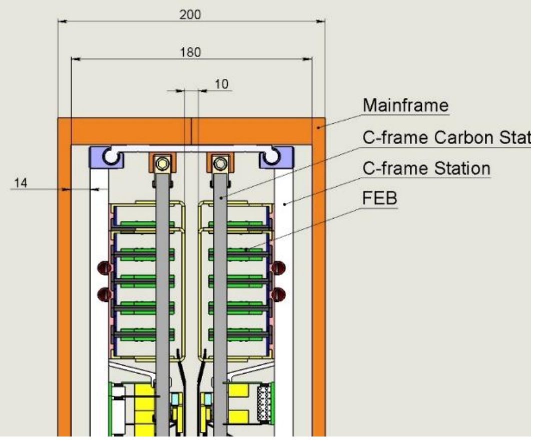

Fig. 4.10.1: View of two consecutive STS Units of one station (side view). The space between staggered FEB boxes available for cabling is 10 mm.

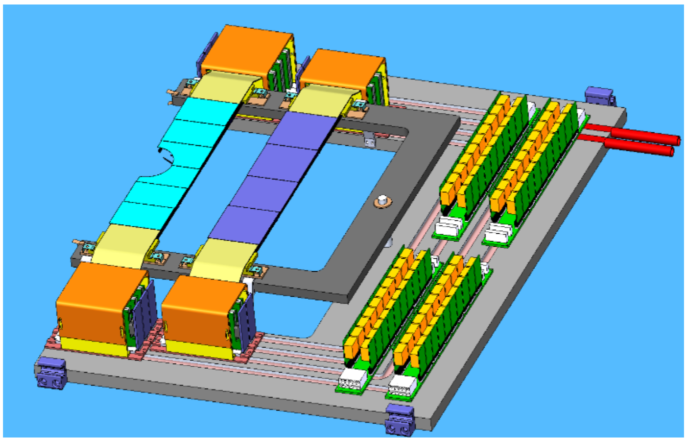

Fig. 4.10.2: View of a quarter of STS station. The space between neighboring FEB boxes available for cabling is 28 mm.

The photograph of the mockup shown in figure 4.10.3 illustrates the narrow gap between the FEB boxes available for cabling.

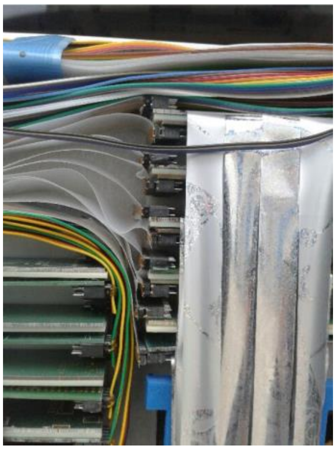

Fig. 4.10.3: Photograph of the mockup illustrating the narrow gap between the FEB boxes available for cabling.

4.10.1 LV and HV powering inside STS box

The sensors should be supplied with the depletion voltage in an asymmetrical manner (e.g. 0 and -150V). The overall maximum biasing voltage of 500V for irradiated sensors may be needed to achieve full sensor depletion and charge collection efficiency after reaching the expected radiation life-time doses. This leads to the requirement of sufficient high voltage insulation of the entire construction, hence up to 500V DC potential difference can occur in many places of the construction. The readout ASIC is powered with 1.2V and 1.8V for analog and 1.8V for the digital part. Both voltages are applied on top of the biasing potentials in a floating manner. The powering scheme is shown in figure 4.10.4. The technical requirements for the LV and HV for BM@N STS are in the most parts the same as for CBM STS, and are described in more detail in [1].

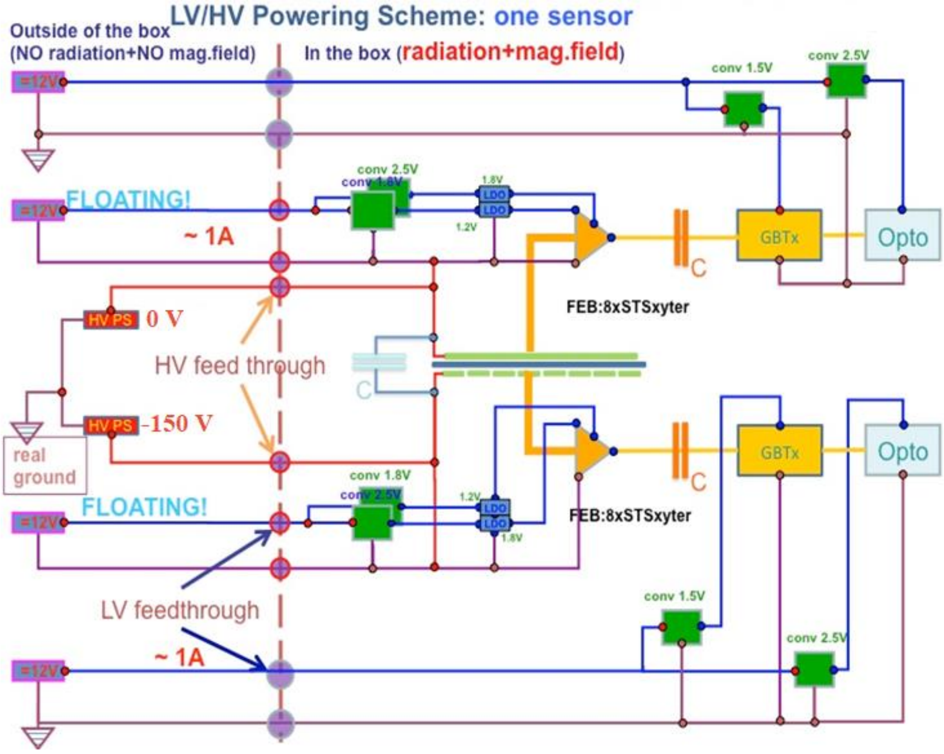

Fig. 4.10.4: Schematics of the low and high voltage supply for one double sided sensor. The broken vertical line illustrates the thermal enclosure, which marks at the same time the high ionizing dose region. Source: [1]

LV powering

The general concept for LV powering foresees to supply 12V @ 1A from outside of the STS and to convert it to needed voltages inside STS box. For this purpose a dedicated D-Sub connectors are used. Since the STS detector is placed in a strong magnetic field of up to 1T, any power converter employed has to use ferrite-less (in general: coreless) inductivities. In addition, all elements placed in the acceptance of the experiment will be strongly irradiated by the flux of the reaction products. To provide 1.8 V and 1.2 V power to each FEB, two dedicated buck converters FEAST MP[16] are used (see figure 4.10.6). DCDC converters are installed on a specially developed PCB – Power Board (PoB). Each PoB carries 20 converters for 10 FEBs (5 modules) i.e. one FEB box. Due to the very tight geometry, the size of the PoB is defined to be < 30 x 250 mm^2. Bulk converters operate at the maximum efficiency (see figure 4.10.6). However, 20% of the input power is dissipated at the PoB. Therefore, an effective cooling of bulk converters is needed. FEASTs are installed onto aluminum fins connected to the heat exchanger plate. The input side of the POB is fed with several 12V supplies floating at the various biasing potentials. It has a high voltage resilient multi-pin connector, which assures power transmission at ~1 A. At the output of the POB, similar connectors for powering lines (2.8V/2.3A and 2.1V/2.5A, power return lines) are used. The photograph of the PoB prototype is shown in figure 4.10.7. To minimize the voltage drop on the LV power lines due to the currents, special attention has to be paid to the PCB conductor cross section and to contact impedances of connectors on the PoB, the FEB as well as the conducting cables.

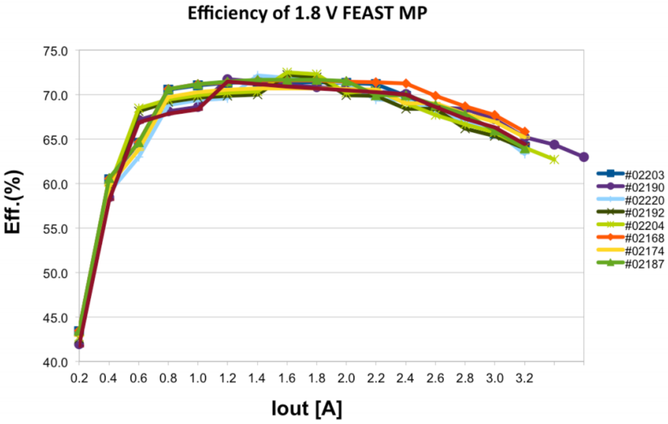

Fig. 4.10.5: Efficiency of 1.8 FEAST MP at 10°C. Vin=12V reaches maximum around Iout=2A.

Fig. 4.10.6: Photograph of the FEAST MP

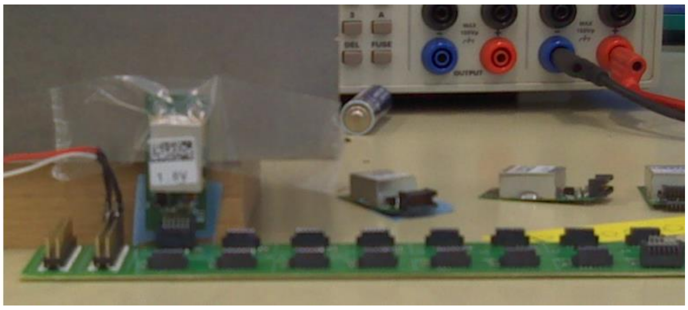

Fig 4.10.7: A prototype of the PoB

---

[16] web page of the DCDC converter project: http://project-dcdc.web.cern.ch

The low-voltage power requirements of the ASICs on the FEB are defined as follows:

- up to 2.5 A at 1.2 V for the analog part (low noise density level: 10^{-12} V^2/Hz in the range 1 - 5 MHz);
- up to 2.3 A at 1.8 V for the digital part.

To achieve a such a low noise density level, and to keep the supplied voltage on the constant level, dedicated LDOs are placed on the FEB near the STSXYTER ASICs. The measured noise spectrum for the 1.8 LDOs is shown in figure 4.10.8

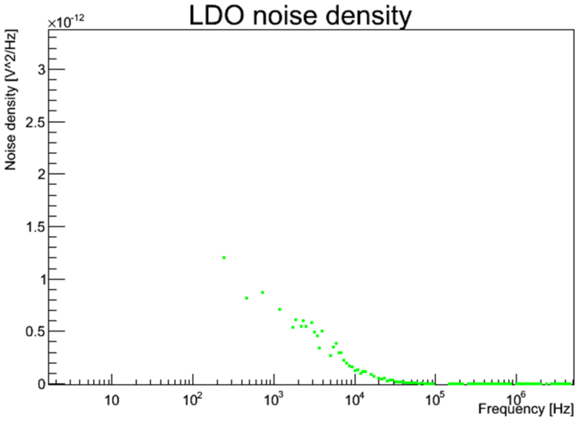

Fig 4.10.8: Noise density of the LDO used for the powering of ASICs

HV powering

The high voltage biasing of the silicon sensors is generated outside of the STS housing, lead into the box and distributed inside the box almost without any power loss because of negligibly low current (< 1mA). Dedicated REDEL connectors are placed on the patch panel on the C-frames. High voltage lines will be installed between the outside wall of the half-station directly to FEB/sensor omitting PoB. The sensor itself is biased with this voltage over the micro-cable (an extra HV trace). Up to 500 V of potential difference may occur in many locations of the PoB-PCB, between FEB-PCBs, between analogue micro-cables as well as between PCB and cooling interface, so precautions have to be taken to protect the system against discharges. For the filtering of the noise and pick-ups, a dedicated CR filter is placed near the FEB-box.

4.10.2 LV and HV powering outside STS box

Power boards will be fed with 12 V power from outside via Sub D37 connectors mounted in the patch panel of each quarter of the STS station, and via 20 m long SABIX cable[17] to WIENER MPOD power supply devices mounted in dedicated racks in the BM@N cave. Additional SENSE lines will be connected to the patch panel. Each 12 V cable for the FEAST has to be floating to allow connection to the sensor bias voltage. The HV will be supplied to the corresponding REDEL connectors on the patch panels via a specially produced by Wiener cables with a length of 20 m. HV WIENER MPOD power supplies will be installed in the same racks in BM@N cave

References:

[1] Low and high voltage powering for STS, P. Koczon, C.J. Schmidt, CBM-TN-18009, September 4, 2018

---

[17] SABIX D 315 FRNC multi-wire cable (0.34mm2 Cu)

4.11 Project organization and time lines

The project organization is sketched in the organigram below. The participation of GSI experts in the construction of the BM@N-STS is based on the legal validity of the Russian-German Roadmap, which still has to be signed by the Russian side. Likewise, the time line is valid under the condition, that the Roadmap will be signed in the first half of 2020, and the German effort is focused on the module assembly. If this is not the case, the duration of the project will increase by 12 months.

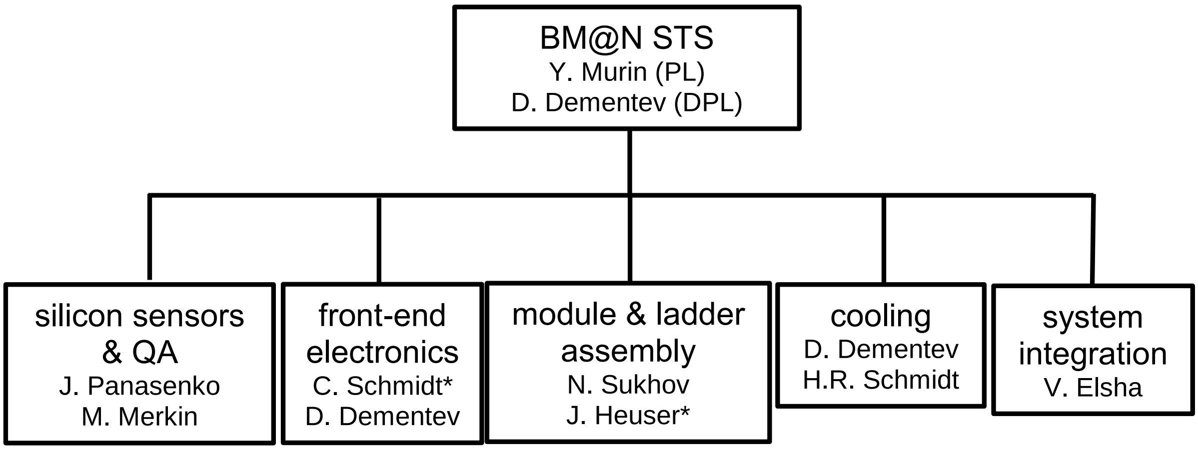

*to be confirmed by GSI

Project time line

Tasks	2020	2021	2022	2023	2024
Module assembly and QA	Tool development	Station 1+2	Station 3+4		
Ladder assembly	Tool development	Station 1+2	Station 3+4		
Micro cables	Production station 1+2	Production station 3+4			
ASICSs	Production	Production			
FEBs	Production	Production			
HV, LV	Development	Production	Production		
CF mainframe	Development	Production station 1+2	Production station 3+4		
Cables, fibres	Design	Production	Production		
Cooling	Design	Production	Production		
Read-out chain	Design	Production	Production		
System integration			Station 1+2	Station 3+4	
Commissioning				Station 1+2	Station 3+4
Data taking					Station 1+2 Station 3+4